

POLITECNICO DI TORINO

Corso di Laurea Magistrale in Ingegneria Aerospaziale

Tesi di Laurea Magistrale

AERODYNAMIC ANALYSIS OF A TRANSONIC BLENDED WING BODY CONCEPT



Relatori

Prof. Romeo Giulio
Prof. Simon Prince
Ing. Davide Di Pasquale

Candidato

Cristina Nuzzo

Anno accademico 2017-18

ABSTRACT

This project is focused on the study of a blended wing body, a concept which theoretically promises improved aerodynamic performance over existing designs. It is an unconventional configuration different from the commercial wing and tube design. The examined wing body is the BW11 Eagle Ray aircraft, designed by the 2011 Group Design Project of the Aerospace Vehicle Design MSc at Cranfield University. The baseline model was designed for subsonic cruise and is now studied in transonic field and its aerodynamic parameters such as lift and drag coefficients, lift-drag ratio and span wise pressure distribution are investigated using Computational Fluid Dynamics (CFD). The aim of the study is to analyse the aerodynamic performance of the BW11 concept at transonic cruise Mach number as a preliminary stage in its redesign for transonic flight. Evaluations of the results show that BW11 is reasonably good in the analysed transonic flight conditions, so some optimizations in its design could allow to reach better performances comparable with conventional tube-wing aircraft.

ACKNOWLEDGEMENTS

This thesis represents the conclusion of MSc studies in Aerospace Engineering with a lot of effort, which have allowed me to gain more confidence in myself.

First of all, the author would like to give her gratitude to supervisor Professor Simon Prince, who gave guidance and helped me in developing this project with enthusiasm and patience. The author wants to give regards to co-supervisor Dr Davide Di Pasquale, whom with I have shared the office for four months and who provided help with a lot of advice about the project. Special thanks to the supervisor Professor Giulio Rome for his availability and for giving me the opportunity to have a wonderful experience at Cranfield University.

Furthermore, the author wants to thank her friends, Savino and Raffaele for sharing a lot of time during exams preparation, Mina for listening to me despite being miles away, Fabiana for cultivating twenty years of friendship, Lucia for always being there also after periods of separation, Mariastefania for always encouraging me, Roberta for always accompanying me during hard times and for always spending time for me when I needed.

Thanks to all people I met in Cranfield with whom I have shared my experience, I hope to see them again. Thanks to Teo, who makes me believe beautiful things can happen also when you do not imagine.

Finally, thanks are also given to my grandparents with whom I grew up, my grandmother for the affection showed despite the separation and for hosting me during the latest and hardest years of studies, to my parents for permitting my studies and for always supporting me, no matter what happened. Thanks to my father who dedicated his entire life to his family doing a lot of sacrifice, and thanks to my mother for always believing in me, and thanks to my sister who is my example and Gianluca who is the most caring person I have ever met, and to my brother who is my pride.

INDEX

Abstract	II
Acknowledgements	III
List of figures	VI
List of tables	X
Nomenclature	XI
1 Introduction	XIII
2 BWB Configurations.....	1
2.1 A short background.....	1
2.1.1 Advantages of BWB.....	3
2.1.2 Disadvantages of BWB	5
2.2 Aerodynamic characteristics of transonic wing section	6
2.2.1 An overview of transonic aerodynamics	6
2.2.2 Supercritical Aerofoil	11
2.3 Aerodynamic of transonic swept wings of transonic wing.....	13
3 Computational Fluid Dynamics (CFD) Analysis.....	16
3.1 Mesh generation	17
3.1.1 Structured Mesh.....	17
3.1.2 Unstructured Mesh	18
3.1.3 Hybrid Mesh.....	19
3.2 Governing Equations.....	20

3.3 Turbulence	22
3.4 Boundary Layer.....	24
4 Results and Discussions	27
4.1 Aerodynamic characteristics of a transonic aerofoil section	27
4.1.1 Analysis with structured mesh over the airfoil RAE2822.....	28
4.1.1.1 Generation of Structured Mesh.....	28
4.1.1.2 Setup and post processing.....	30
4.1.2 Analysis with unstructured mesh over the aerofoil RAE2822	36
4.1.2.1 Generation of unstructured Mesh.....	37
4.1.2.2 Setup and post processing.....	38
4.2 BW11 CFD Analysis	40
4.2.1 Mesh generation	40
4.2.2 Setup.....	45
4.2.3 Aerodynamic characteristics	47
4.2.3.1 Pressure and Mach distribution	59
4.2.4 BW11 Aerodynamic Optimization on conceptual design.....	73
4.2.5 Critical comments about advantages and disadvantages mentioned.....	74
5 Conclusions	75
6 References	77

LIST OF FIGURES

Figure 2.1 AVRO Vulcan[2].....	1
Figure 2.2 Advantages of BWB Configuration [10]	4
Figure 2.3 Definition of transonic flow domain around a two-dimensional airfoil [12].....	7
Figure 2.4 The movement of shock wave with increasing Mach number [13].....	8
Figure 2.5 Drag behaviour and definition of the drag divergence Mach number [14].....	9
Figure 2.6 Buffet boundary at various Mach number and lift coefficient [12].....	10
Figure 2.7 Pressure distribution on a conventional (NACA 6-series) airfoil and a supercritical airfoil. (a) Supersonic domain over NACA 6- series airfoil. (b) Pressure distribution over NACA 6-series airfoil. (c) Supersonic domain over supercritical airfoil. (d) Pressure distribution over supercritical airfoil [12]	12
Figure 2.8 Typical geometry and characteristics of a supercritical airfoil [12].....	13
Figure 2.9 Swept back wing [15].....	18
Figure 3.1 Structured mesh around an airfoil [18].....	18
Figure 3.2 Unstructured mesh around an airfoil [18]	18
Figure 3.3 Subdivision of near Wall Region [18].....	25
Figure 4.1 RAE2822 airfoil.....	27
Figure 4.2 Domain divided into blocks	28
Figure 4.3 Mesh A	29
Figure 4.4 Mesh B.....	29
Figure 4.5 C_p distribution on the airfoil RAE2822	32

Figure 4.6 Mach number distribution computed with Spalart Allmaras model and for mesh B	33
Figure 4.7 y^+ profile on the curves calculated with Spalart Allmaras model and for mesh B	34
Figure 4.8 Residuals of iterations process of mesh B and turbulence model Spalart Allmaras.....	35
Figure 4.9 Lift coefficient convergence history	36
Figure 4.10 Drag coefficient convergence history	36
Figure 4.11 Far field surface cut	37
Figure 4.12 Unstructured mesh over the aerofoil RAE2822	38
Figure 4.13 Comparison of C_p distribution obtained by VGK, Structured Mesh and Unstructured mesh	39
Figure 4.14 Main views of the BW11 Eagle Ray baseline model used for aerodynamic analysis [20]	40
Figure 4.15 BW11 baseline model	41
Figure 4.16 Parts of geometry division in ICEM	41
Figure 4.17 Domain	42
Figure 4.18 Refinement of the mesh at the trailing edge.....	43
Figure 4.19 Unstructured Volumetric Mesh.....	43
Figure 4.20 Detail of unstructured volumetric mesh (side view).....	44
Figure 4.21 Detail of prism layer mesh	45
Figure 4.22 C_L versus α at different Mach numbers	50
Figure 4.23 C_D versus α at different Mach numbers	52
Figure 4.24 C_D versus M_∞ at $\alpha=2^\circ$	52
Figure 4.25 C_L versus C_D at $M_\infty=0.7$, fine mesh and $M_\infty=0.75$, fine mesh	53

Figure 4.26 C_L versus C_D at $M_\infty=0.75$, coarse mesh and $M_\infty=0.8$, fine mesh	54
Figure 4.27 C_L/C_D versus α for each Mach number and fine mesh.....	55
Figure 4.28 C_M versus α for each Mach number	58
Figure 4.29 Static margin versus Mach number.....	59
Figure 4.30 C_p distribution at $M_\infty=0.75$ and $\alpha=2^\circ$ on top and bottom surface of BW11	60
Figure 4.31 C_p distribution at $M_\infty=0.77$ and $\alpha=2^\circ$ on top and bottom surface of BW11	61
Figure 4.32 C_p distribution at $M_\infty=0.8$ and $\alpha=2^\circ$ on top and bottom surface of BW11	62
Figure 4.33 Section $\eta=0$, Mach and C_p distribution at $M_\infty=0.8$ and $\alpha=2^\circ$	63
Figure 4.34 Section $\eta=0.17$, Mach and C_p distribution at $M_\infty=0.8$ and $\alpha=2^\circ$	64
Figure 4.35 Section $\eta=0.34$, Mach and C_p distribution at $M_\infty=0.8$ and $\alpha=2^\circ$	65
Figure 4.36 Section $\eta=0.45$, Mach and C_p distribution at $M_\infty=0.8$ and $\alpha=2^\circ$	66
Figure 4.37 Section $\eta=0.80$, Mach and C_p distribution at $M_\infty=0.8$ and $\alpha=2^\circ$	67
Figure 4.38 Section $\eta=1$, Mach and C_p distribution at $M_\infty=0.8$ and $\alpha=2^\circ$	68
Figure 4.39 Section $\eta=0.80$, Mach and C_p distribution at $M_\infty=0.7$ and $\alpha=2^\circ$	69
Figure 4.40 Section $\eta=0.80$, Mach and C_p distribution at $M_\infty=0.75$ and $\alpha=2^\circ$	70

- Figure 4.41 Section $\eta=0.80$, Mach distribution at $M_\infty=0.8$ and $\alpha=3^\circ$.. 71
- Figure 4.42 Section $\eta=0.80$, bubble separation at $M_\infty=0.8$ and $\alpha=3^\circ$... 72
- Figure 4.43 Section $\eta=0.80$, C_p distribution at $M_\infty=0.8$ and $\alpha=3^\circ$ 72

LIST OF TABLES

Table 3.1 Comparison of Experimental and Computational simulation	16
Table 4.1 Aerodynamic Results for Mesh A	33
Table 4.2 Aerodynamic Results for Mesh B.....	34
Table 4.3 Comparison of results obtained by VGK, unstructured mesh and structured mesh	38
Table 4.4 Physical quantities corresponding at different Mach numbers...	47
Table 4.5 C_L, C_D, C_M and C_L/C_D corresponding at different angles of attack at $M_\infty=0.7$, fine mesh	48
Table 4.6 C_L, C_D, C_M and C_L/C_D corresponding at different angles of attack at $M_\infty = 0.75$, fine mesh	48
Table 4.7 C_L, C_D and C_L/C_D corresponding at different angles of attack at $M_\infty = 0.75$, coarse mesh	49
Table 4.8 C_L, C_D, C_M , and C_L/C_D corresponding at different angles of attack at $M_\infty = 0.8$, fine mesh.....	49
Table 4.9 Equations of linear part of lift curve corresponding at different Mach numbers	50
Table 4.10 $C_{L0}, C_{L\alpha}$ and α_{0lift} at different Mach numbers	51
Table 4.11 K_n and $C_{M\alpha}$ for each Mach number	57

NOMENCLATURE

C_p	Pressure Coefficient	
C	Chord	m
C_D	Drag coefficient	
C_L	Lift coefficient	
C_M	Pitching moment coefficient	
Re	Reynolds Number based on chord	
M	Mach Number	
M_{DD}	Drag Divergence Mach Number	
M_∞	Freestream Mach Number	
M_{crit}	Critical Mach Number	
α	Angle of attack	deg
ρ	Density	Kg/m^3
t	Time	s
\mathbf{u}	Velocity	m/s
a	Speed of sound	m/s
τ	Viscous stress tensor	Pa
e_0	Specific total energy	J/Kg
h_0	Specific Stagnation enthalpy	J/Kg
\mathbf{q}	Conduction heat flux vector	J
c_p	Specific heat capacity at constant pressure	J/kg

c_v	Specific heat capacity at constant volume	J/kg
μ	Dynamic Viscosity	Pa·s
ν	Kinematic Viscosity	m^2/s
y^+	Non-dimensional wall distance	
u_τ	Friction velocity	
τ_w	Shear stress of the wall	Pa
\otimes	Tensor product	
BWB	Blended Wing Body	
CFD	Computational Fluid Dynamic	
RAE	Royal Aircraft Establishment	
BLI	Boundary Layer Ingestion	
2D	2-Dimensional	
3D	3-Dimensional	

1 INTRODUCTION

In recent years a new concept of airplane design has started to be considered. The blended wing body configuration consists of a wing that blends smoothly into a wide flat, tailless fuselage. The body generates the most of the lift and some theories suggest that the entire aircraft produces less drag than a corresponding cylindrical fuselage/wing arrangement. The consequence is less fuel consumption and increase of autonomy. This project is focused on the analysis of the BW11 Eagle Ray aircraft, designed by the 2011 Group Design Project of the Aerospace Vehicle Design MSc at Cranfield University for subsonic cruise. The aircraft has been investigated in transonic field and the study is fundamentally from an aerodynamic point of view. This thesis is structured as follows. Chapter 2 gives a short overview of the motivations which has increased the interest in the study of the blended wing body concept, and some advantages and disadvantages of this configuration are mentioned. Moreover, some aspects of transonic aerodynamics of wing sections and supercritical aerofoils are shown because the analysis has been carried out in transonic field, and the BW11 uses this type of aerofoil. In addition, the aerodynamics of transonic swept wings is explained. The aerodynamic performance has been analysed through Computational Fluid Dynamics (CFD), where ANSYS Fluent software has been used throughout the project to solve for the fluid flow around the body. The governing equations including the turbulence equations for resolution of the turbulent boundary layer which Fluent has to solve are explained in chapter 3. Chapter 4 presents the CFD analysis of a supercritical aerofoil, which is the RAE2822, with both structured and unstructured meshes to provide a preliminary validation of the CFD method used. Different meshes have been studied and they are described. These have been used to simulate the fluid flow around the aerofoil using three different turbulence models, the aim was understanding which one is the better for blended wing body analysis and which type of mesh is best to give accurate results at reasonable computational time cost. The generation of the mesh over the blended wing body is described and results of the main aerodynamic characteristics obtained using CFD after the selection of an adequate turbulence model are introduced. Moreover, some proposals are given to optimize and to achieve aerodynamic improvements in the

design of the aircraft. Chapter 5 summarises the results of this work and presents the discussion of the BW11 aerodynamic performance at transonic speed.

.

2 BWB CONFIGURATIONS

A Blended Wing Body (BWB) configuration consists of blended wing and body of a conventional aircraft to generate a tail-less vehicle that includes a bulge in the centre to enhance volume for passengers and airframe systems. Motivations for the interest in this configuration type have been improvements in emissions in the atmosphere and fuel consumption.

2.1. A Short Background

The Boeing B-47 which had the typical characteristics of jet airliners that fly nowadays, took its first flight in 1947. Most commercial aircraft developed subsequently to improve performance had the same basic shape with swept tapered wings, rear empennage and engines hung on pylons under the wing. Kunawala [1] states that “Their changes can be considered more evolutionary than revolutionary”. The first studies of BWB configurations were by Alexander Lippisch in Germany in the 1930s. Perhaps the first successful blended wing body aeroplane was the AVRO Vulcan which was developed as a transonic cruise bomber in the early 1950s (figure 2.1).



Figure 2.1 AVRO Vulcan [2].

A more recent study of a Blended Body (BWB) configuration was conducted in 1988 by McDonnell Douglas because NASA was interested in long-range transport aircraft concept [3]. Comparison of this preliminary configuration concept with conventional aircraft pointed out that the blended configuration was remarkably lighter and has higher lift to drag ratio [4], [5]. Moreover, Liebeck [6] pointed out that a blended wing body was characterized by lower fuel burn. In his studies an 800-passenger BWB and a conventional configuration airplane were sized and compared for a 7000-n mile design range and the author concluded that a reduction of about 30% fuel burn per seat can be achieved with a BWB. According to Ikeda and Bil [7], from the conceptual point of view, the BWB design is more attractive than the conventional aircraft because the BWB concept aircraft offers the potential to become the standard commercial aircraft in the next generation, being more fuel effective and environmentally-friendly at the same time. They have shown the results of the comparison of the A380 and an optimised BWB design obtained with CFD to demonstrate that the BWB design has the potential to be more aerodynamically efficient, because the BWB configuration performs with less energy dissipation. In order to gain confidence of the state-of-the-art CFD simulations Dehpanah and Nejat [8] have studied an initial scaled blended-wing-body airframe using computational analyses in the early conceptual design stage and developed a modified airframe based on evaluation of the initial airframe with the aim of improving it in the early stage of the conceptual design. Key design parameters were identified using CFD, investigating the variation of lift, drag, and pitching moment coefficients, spanwise lift and cross-sectional area distribution have been studied for improving the performance of the airframe. At the end the revised airframe was proposed as a high-capacity long-range blended-wing-body commercial transport. Wind tunnel tests were also conducted on a 2% model of Boeing's BWB-450-1L configuration in the NASA Langley Research Center's National Transonic Facility and the Arnold Engineering Development Center's 16-Foot Transonic Tunnel [9]. Characteristics of the configuration and the effectiveness of the elevons, drag

rudders and winglet rudders were measured at various angles of attack, yaw angles, and Mach numbers at subsonic and transonic speeds. The data from these tests were used to develop a high-fidelity simulation model for flight dynamics analysis and also serve as a reference for CFD comparisons. Due to these potential benefits, despite some challenges identified in the design, the BWB is seen by some researchers as the future innovation for airliners.

2.1.1. Advantages of BWB

According to Kunawala [1], the BWB configuration presents some aerodynamic benefits which are very helpful to reduce fuel consumption that is one of the main parameters that influence the direct operating costs (DOC) of the aircraft. These aerodynamic advantages are stated to be:

- Lift is also generated by centre-body, so aerodynamic performance can be improved, and wing load is reduced.
- Wetted area is maybe reduced due to the small outer wing, and consequently the aerodynamic efficiency (L/D) increases, since friction drag is proportional to wetted area. The absence of the horizontal tail also reduces the friction drag.
- Reduction of interference drag due to less junctions between the wing and body.
- The BWB's cross-sectional area variation is similar to that of the Sears-Haack body, which is the body with the lowest theoretical wave drag due to volume, so BWB is characterized by a reduction of wave drag at transonic speed.
- The aft-location of engines balances the airframe and offsets the weight of the payload, furnishings and systems, and it also guarantees a better efficiency with Boundary Layer Ingestion (BLI), because the boundary layer is fully developed behind the

wing. The consequence of that is the decreasing of pressure drag, therefore the reduction in the required thrust and fuel burn.

- The reduction of bending moment, due to the fact that wing and body are joined together. This implies a better weight distribution along the span and consequently a lighter structure can withstand the weight.
- Noise reduction due to the absence of tail and of lifting surface. Moreover, exhaust noise is not reflected under wing surface due to their aft-location.
- Low manufacturing cost thanks the simplicity of BWB configuration.
- Reduction of boarding and de-boarding time and shorter take-off field length due to its short fuselage.

These concepts are summarised in the Figure 2.2:

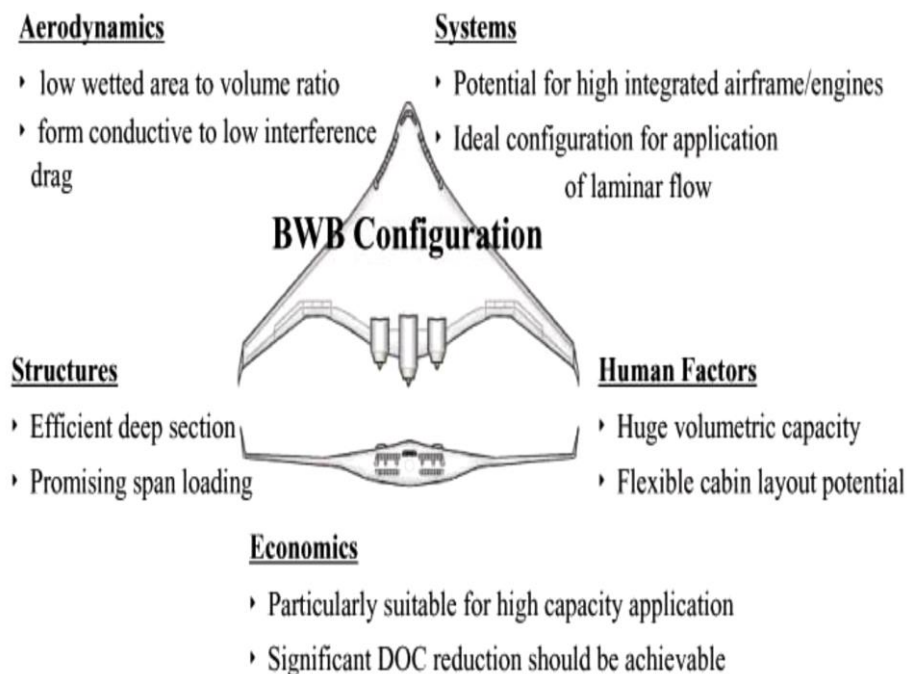


Figure 2.2 Advantages of BWB Configuration [10].

2.1.2. Disadvantages of BWB

Notwithstanding these benefits, there are some challenges in designing these types of configurations. Kunawala [1] and Liebeck [11] mention some of them:

- High thickness to chord ratio, that is necessary for accommodating of passengers and cargo, may be a problem to maintain low drag.
- Centre-body aerofoils must be designed to provide the necessary lift considering deck angle limitations.
- Supersonic flow that may occur on the lower surface is a challenge because it does not typically happen with a conventional configuration.
- Transition from the thicker centre-body aerofoil to thinner outer wing aerofoil could be abrupt.
- Embedded engines and BLI include some challenges because these technologies are not yet mature. For instance, the design of low-loss inlet ducts and the control of the inlet flow distortion are necessary.
- A BWB pressurized cabin will need to be non-cylindrical due to the flattened body, so it is more difficult to make the structure light and able to withstand bending loads and cabin pressure loads.
- Outer wing aerofoils should operate at high lift coefficients to maintain a reasonable span loading, due to their smaller chord than centre-body aerofoil, potentially causing catastrophic buffet (aerodynamic excitation), buffeting (aeroelastic response) and earlier stall characteristics.

2.2. Aerodynamic characteristics of transonic wing section

The starting point for aerodynamics analysis of an aircraft is studying the aerofoil that generates the pressure distribution on top and bottom surface of the wing to create the required lift. Given that the BW11 is analysed for transonic flight, which requires special aerofoil designs to suppress adverse effects or postpone them to higher Mach numbers, an overview of transonic aerodynamics and supercritical aerofoils is presented [12].

2.2.1. An overview of transonic aerodynamics

Flows close to the speed of sound makes the flow field transonic, where two distinct regions of flow exist at the same time: a subsonic domain and a supersonic domain. The sonic flow region is condensed in a line in two-dimensional case or in a surface in three-dimensional case, delineating the subsonic and the supersonic domains. The size and extent of these domains change with Mach number. Indeed, as the flow accelerates from low speed it is initially all subsonic, then when the free-stream Mach number reaches the Critical Mach number, a point of the flow over the body Mach reaches the sonic value, and at Mach numbers above this a supersonic domain forms. A normal shock wave appears because the flow has to decelerate back to the free-stream conditions. This shock moves downstream with increasing free stream Mach number extending the supersonic region further rearward. When the freestream Mach number exceeds sonic value, a detached bow shock wave forms in front of the body. Only the flow behind the normal part of the shock becomes subsonic, while the flow behind oblique branches will remain still supersonic. The more the freestream Mach Number increases, the smaller the subsonic domain becomes behind the shock. The flow is conventionally established to be supersonic when the value of Mach Number is greater than about 1.3.

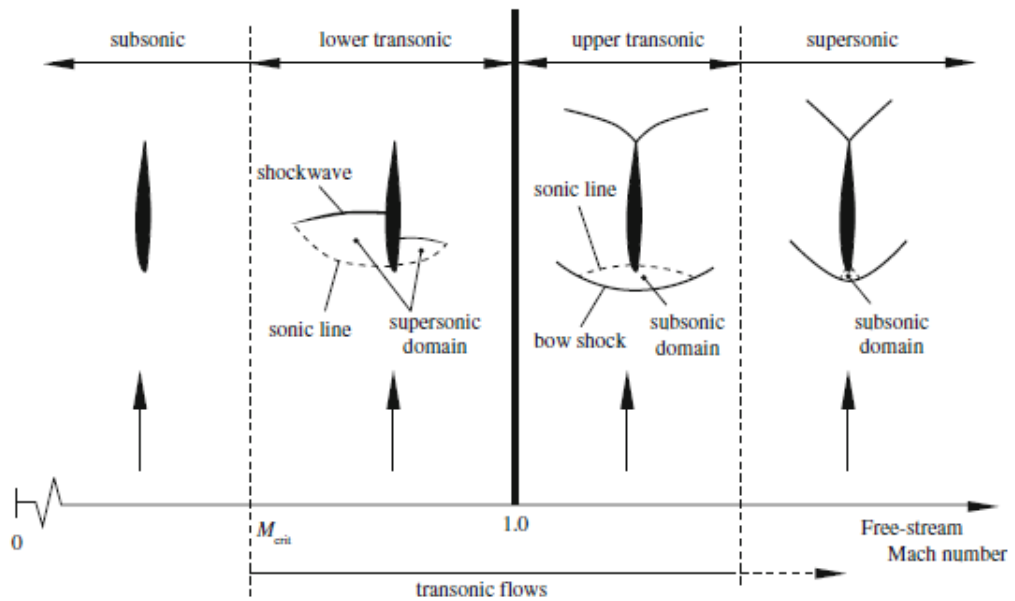


Figure 2.3 Definition of transonic flow domain around a two-dimensional aerofoil [12].

Figure 2.3 and Figure 2.4 show all three subdomains around a two-dimensional aerofoil and the movement of the transonic shock wave with increasing Mach number. One of the negative aerodynamic aspects of transonic flow is this shock wave that appears in flow field and becomes stronger when speed increases. Shock waves cause an increase of drag because they dissipate kinetic energy of the flow as thermal energy, preventing the full recovery of the pressure. Moreover, due to the sudden increase of pressure through the shock the local boundary layer becomes thicker causing viscous drag rise and may even separate.

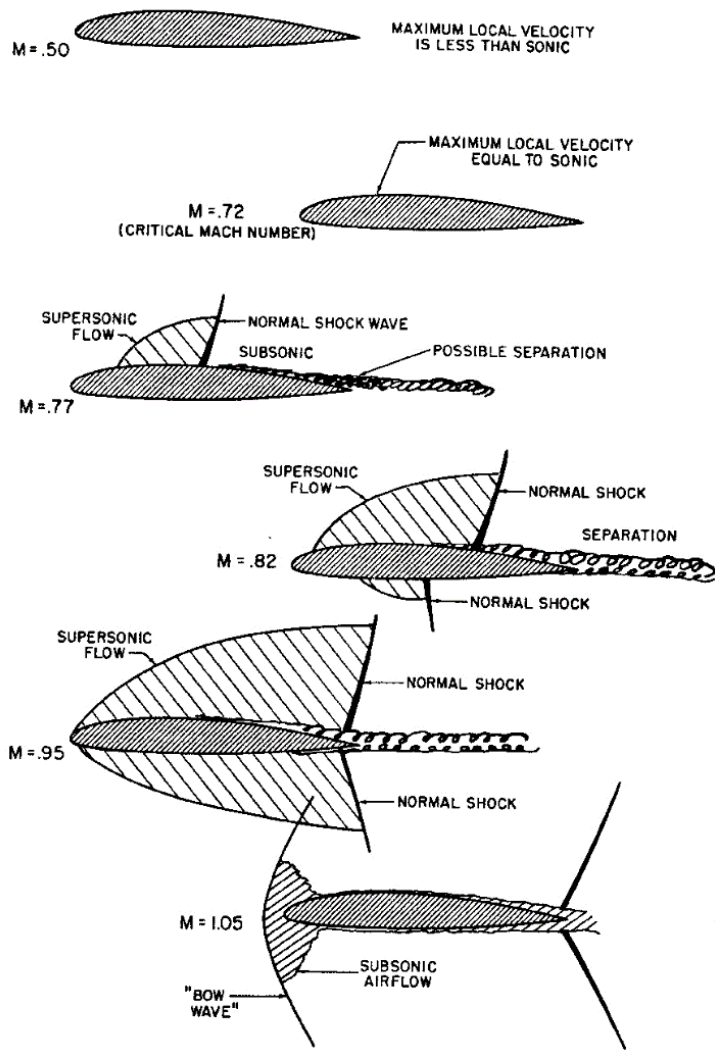


Figure 2.4 The movement of shock wave with increasing Mach number [13].

Another drawback of transonic flow is the drag divergence. First of all, the onset of wave drag, originated from the shock wave, causes a slow increase in drag (known as *drag creep*). Then the local shock on the top of the wing generates an adverse pressure gradient over the boundary layer and when the shock becomes very strong separation occurs and drag rises exponentially. Drag Divergence Mach Number (M_{DD}) is the Mach number at which this rapid increase of drag begins, as is shown in Figure 2.5, due to the formation of strong shock waves on the wing surface in combination with separation at

the shock foot. Several definitions are available to define it. Boeing asserts that Drag Divergence Mach Number is the Mach Number at which drag coefficient value is 20 times higher than the value in the mid-subsonic region, while Airbus and Douglas define it as the Mach number at which $dC_D/dM = 0.10$.

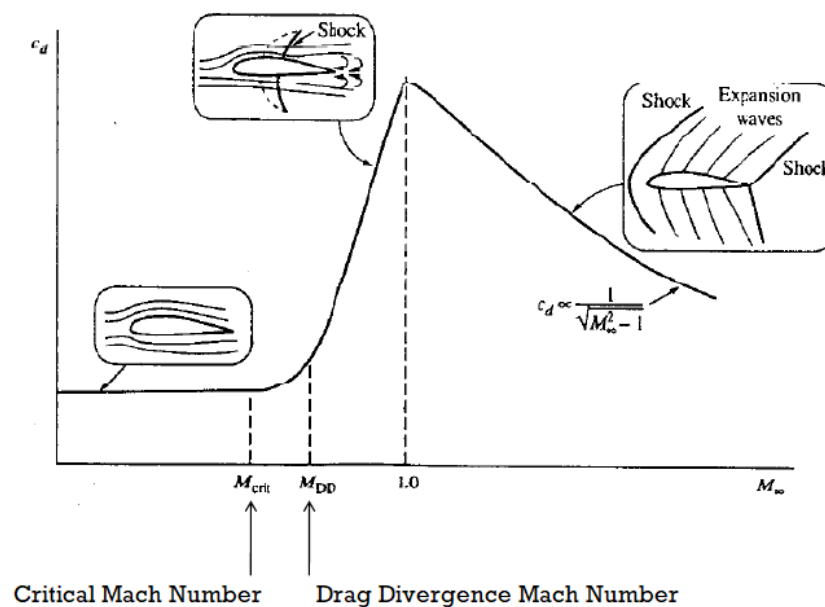


Figure 2.5 Drag behaviour and definition of the drag-divergence Mach number [14].

One of the worst enemies of aerodynamic efficiency is buffet. It is generated by the interaction between the unsteady shock oscillation and the resulting periodic separation at the shock foot. Indeed, separation and the associated wake cause pressure fluctuations that are transmitted to the aerofoil and they translate in structural vibrations, called buffeting. In transonic conditions separated boundary layers can also generate a periodic motion of the shock wave on the surface of the aerofoil, generating large pressure fluctuations. Typical shock-induced vibrations have a frequency that is several orders of

magnitude greater than the wing natural frequency, so these large fluctuations are felt by the structure. This phenomenon is known as transonic buffet. Therefore, buffet is firstly caused by separation of the boundary layer that occurs at foot of shock wave when the velocities become large and so shock wave that terminates the supersonic domain and increases in strength. Moreover, buffet limits lift capability of the wing, indeed according to aeronautical regulation it is necessary to have a margin of 30% between design-lift coefficient and lift coefficient at which buffet occurs. Figure 2.6 shows the buffet onset boundary, obtained by plotting buffet-onset lift coefficient and Mach number.

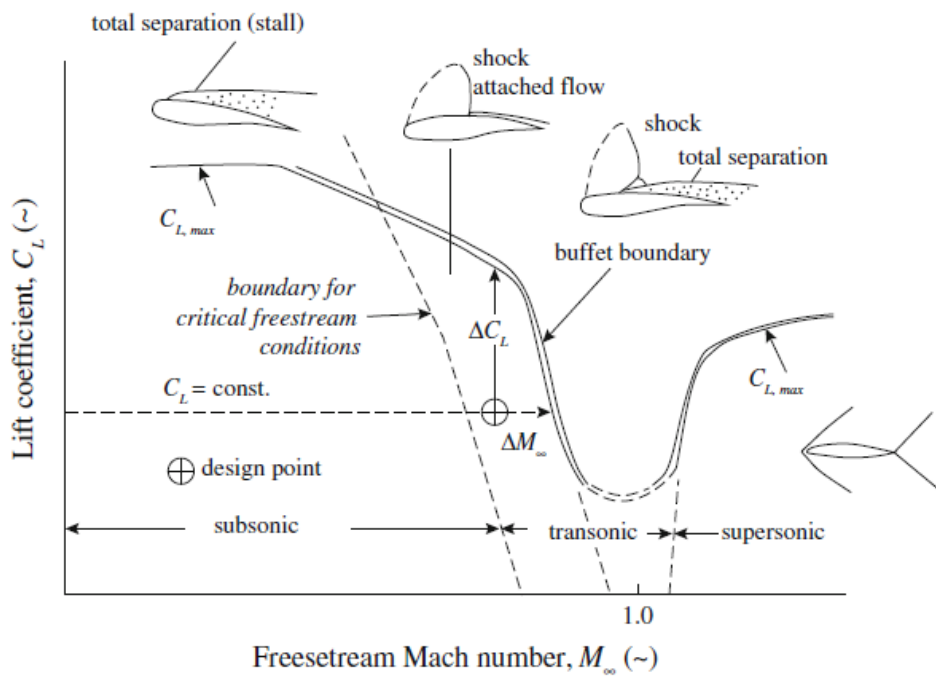


Figure 2.6 Buffet boundary at various Mach number and lift coefficient [12].

2.2.2. Supercritical Aerofoil

Conventional low speed aerofoils produce a large wake drag when free-stream Mach number is beyond the critical Mach number due to the formation of the transonic shock wave and strong separations at the shock foot. This limits the maximum Mach number. A supercritical aerofoil is designed to postpone the onset of shock waves and to produce low drag at high Mach number. A supercritical aerofoil has a flatter suction surface and a higher nose radius to reduce suction peak at the nose and to delay the stall, and to avoid excessive supersonic velocities, compared with a conventional aerofoil with the same thickness. Moreover, a supercritical aerofoil has a concave curvature near the trailing edge to give a larger contribution to lift, called aft loading, which causes an increase in pressure on the lower surface. This is a way to make super velocities unnecessary on the upper surface for a given lift coefficient. In addition, the abrupt transition through the strong shock wave of a conventional aerofoil is replaced by a weak shock wave that appears further aft on the aerofoil and its aim is to avoid shock induced separation; the result is to minimize wave drag increment. Essentially, the key to transonic aerofoil design is to control the expansion of the flow to supersonic speed and its subsequent recompression. These aspects are shown in Figure 2.7 that compares a conventional aerofoil and a supercritical aerofoil.

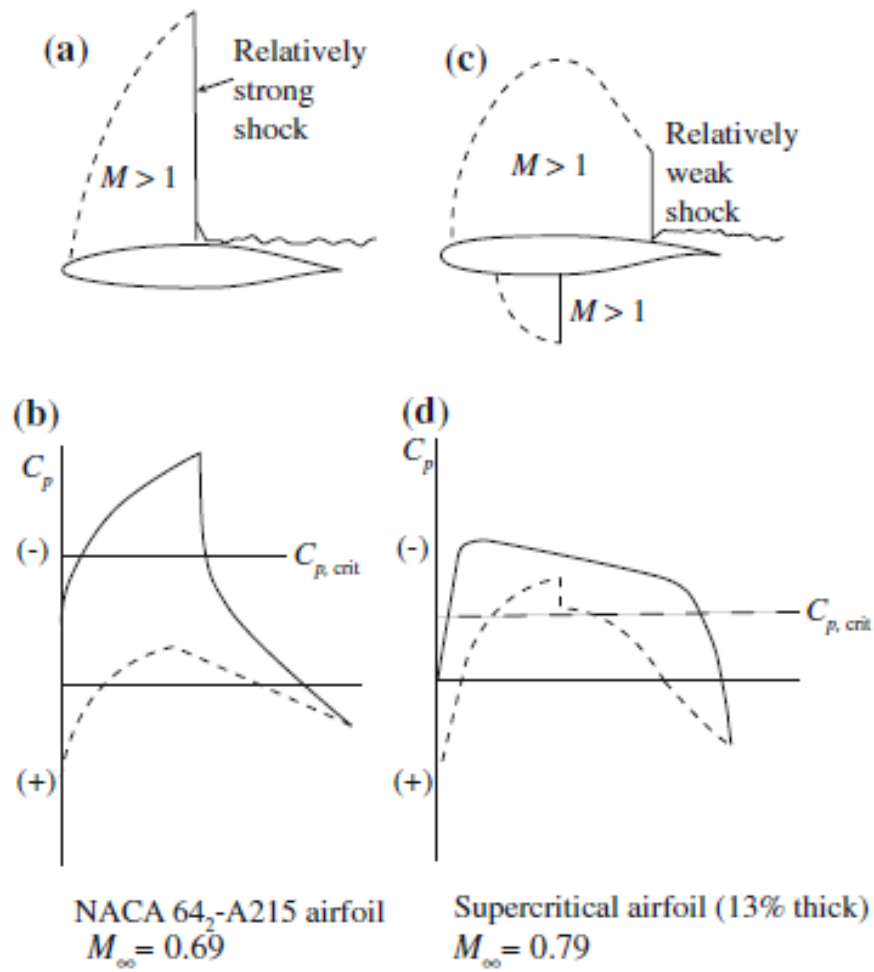


Figure 2.7 Pressure distribution on a conventional (NACA 6-series) airfoil and a supercritical aerofoil. (a) Supersonic domain over NACA 6-series airfoil. (b) Pressure distribution over NACA 6-series airfoil. (c) Supersonic domain over supercritical airfoil. (d) Pressure distribution over supercritical airfoil [12].

Figure 2.8 shows geometric characteristics of a supercritical aerofoil, and the flow development around it.

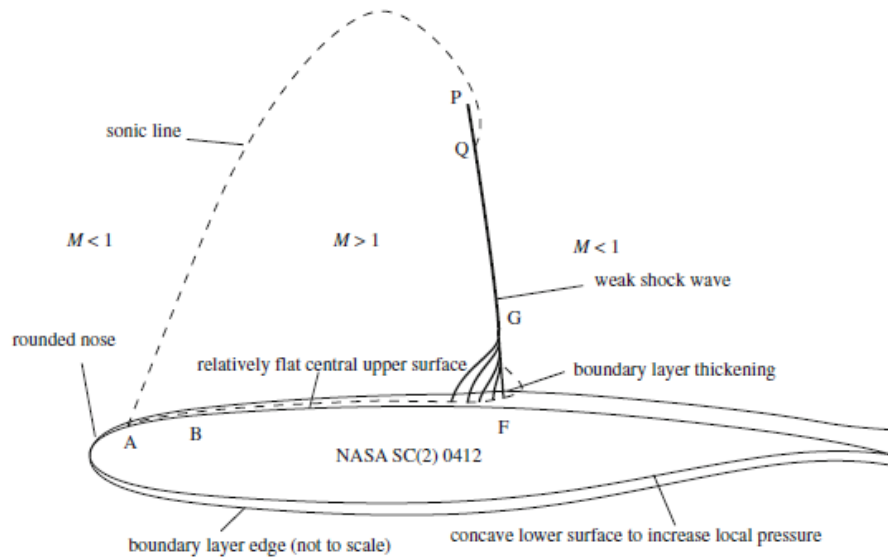


Figure 2.8 Typical geometry and characteristics of a supercritical airfoil [12].

A Sonic line, that separates the two flow domains – the purely supersonic and the purely subsonic merges into the shock wave at the point Q. The shock is slightly curved, and it is generated by the coalescence of compressive waves at its foot. Above the point Q the shock is oblique, therefore behind this part there is still a small supersonic region, while below the point Q the shock is normal, so the flow decelerates to subsonic conditions.

2.3 Aerodynamic of transonic swept wings of transonic wing

In the previous paragraph the transonic flowfield around a supercritical aerofoil is described, now another way of weakening transonic effects in terms of configuration aerodynamics is investigated. Today, transonic wings are usually swept back to delay the drag rise. The swept wing simply allows an aircraft to fly at higher Mach number without the exponential increase in

wave drag. The origin of the swept wing is the theory of the infinite shearing wing. By sweeping the leading edge of a wing with infinite span the free stream velocity vector is no longer perpendicular to the lifting surface. The pressure distribution will decrease with the cosine of the sweep angle Λ (figure 2.9). Hence the pressure and the lift coefficient and the complete lift of the wing decrease with the sweep angle. This is the cosine rule. The relationship between a swept wing and a straight wing section which is parallel to the free stream, is described by the following equation:

$$\frac{L_{swept}}{L} = \frac{C_{L,swept}}{C_L} = \frac{C_{p,swept}}{C_p} = \frac{\left(\frac{\partial C_l}{\partial \alpha}\right)_{swept}}{2\pi} = \cos \Lambda \quad (2.1)$$

Applying the cosine rule, the velocity vector can be decomposed into two components whereby one is perpendicular, and one is parallel to the leading edge as shown in figure 2.9. The magnitudes of the two components are given by the following relations:

$$v_N = v_\infty \cdot \cos \Lambda \quad (2.2)$$

$$v_T = v_\infty \cdot \sin \Lambda \quad (2.3)$$

The normal component is responsible for the aerodynamic characteristics; therefore, it is possible to write equation 2.4 and it is possible to extend it for the cases of the critical condition and drag divergence.

$$M_N = M_\infty \cdot \cos \Lambda \quad (2.4)$$

$$\frac{M_{cr,N}}{M_{cr,\infty}} = \frac{M_{DD,N}}{M_{DD,\infty}} = \cos \Lambda \quad (2.5)$$

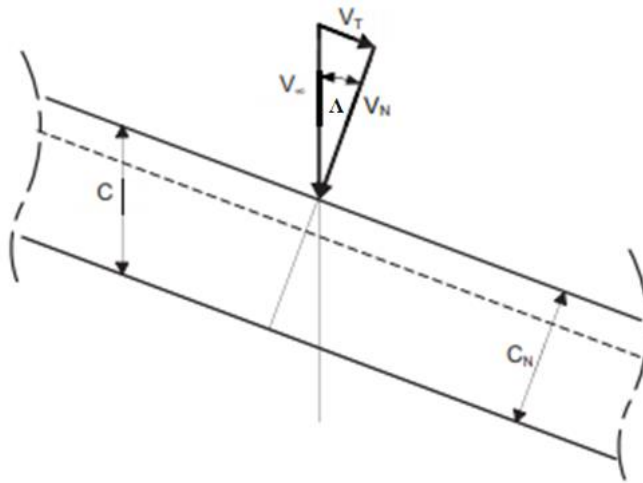


Figure 2.9 Swept back wing [15].

The effect of wing sweep is to reduce the effective Mach Number normal to leading edge. Although wing sweep gives the benefits of delaying the formation of shock waves and accompanying aerodynamic drag rise caused by fluid compressibility near the speed of sound thereby improving performance, wing sweep will tend to shift the load outboard, leading to high section C_L , and the possibility of outboard stall. The wing is twisted to unload the tip. The lift curve slope also decreases. Thus, the total system design must be considered when selecting the wing sweep [16].

3 COMPUTATIONAL FLUID DYNAMICS (CFD) ANALYSIS

The classical way to characterize the aerodynamic performance of a new aircraft concept is making use of wind-tunnel tests. Nowadays, extension of the flight envelope has reached flow regimes that are difficult to reproduce in ground test facilities. Moreover, thanks to the development of the technologies, CFD is a powerful numerical tool to support the aerodynamic analysis. CFD will not replace experimental tests, but it provides results in a complementary way to the wind tunnel test. Table 3.1 shows the comparison between experimental and numerical flow simulation [17].

Table 3.1 Comparison of Experimental and Computational simulation.

Computational fluid simulation	Experimental Fluid Simulation
real geometry	scaled geometry
no limits for variation of parameters	model flexibility limited
known boundary conditions	not always defined boundary conditions
real Reynolds number	Reynolds number may be too low
short response time	long response time
Low cost of first data point, but cost increasing with the data volume and time	High cost of first data point, but cost decreasing with the data volume and time
accuracy decided by mesh quality	accuracy decided by measuring technique
good reproducibility	questionable flexibility
flow representation by model approximation	real flow
computer speed and memory limited	Model manufacture and testing procedure limited

The software used to perform the calculation and to solve the flux is ANSYS Fluent, a commercial code used by industry and researchers. The aerofoil investigated in the 2D analysis is the supercritical aerofoil RAE2822, while the blended wing body analysed is the BW11 Eagle Ray aircraft, designed by

the 2011 Group Design Project of the Aerospace Vehicle Design MSc at Cranfield University. Moreover, aerodynamic characteristics of the aerofoil are compared with VGK results. VGK is a CFD method coded in FORTRAN for predicting the aerodynamic characteristics of a two-dimensional single-element aerofoil in a subsonic freestream, including the effects of viscosity (boundary layers and wake) and shock waves. This code is based on an iterative approach to solve the inviscid flow region (assumed to be 2D full-potential) with coupled finite-difference equations for the viscous flow region that is represented by the integral boundary layer equations. The code needs two input files, one that contains the coordinate of the profile and one that contains parameters to generate the computational grid and flow conditions. The principle advantages of the code are the low computational time; indeed, it takes only few seconds to obtain results, and the corresponding physical accuracy.

3.1. Mesh generation

Creating the mesh is the first step in the CFD process. The mesh is a set of cells (control volumes) of a calculation field in which a set of approximated conservation equations are solved. The grid strongly influences the results and its generation represents the task most demanding and time consuming. The geometry around which the mesh has to be generated is imported and boundaries of the domain are built. After that, nodes are distributed on the edges of the domain. Meshes can be classified as either structured or unstructured. The difference consists of the shape of the elements.

3.1.1. Structured Mesh

In structured meshes nodes are generated by the intersection of two families of lines that belong to systems of Cartesian or curvilinear coordinates, as shown in Figure 3.1. These lines define the interfaces of the cells.

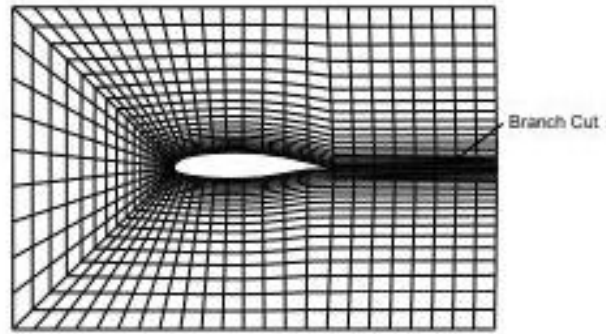


Figure 3.1 Structured mesh around an airfoil [18].

The advantages are:

- Simplicity and easy data access
- Less computer memory
- Better control over the size and shape of elements
- Elements that are generated can be better aligned with the flow, so the quality of mesh can be very high, and convergence thereby faster.

On the other hand, for a complex geometry a structured mesh is complicated and especially near a boundary surface it could give inaccurate results. This type of mesh has been used for the 2D case, so for meshing the aerofoil, which is a simpler geometry than the entire 3D BWB.

3.1.2. Unstructured Mesh

Unstructured meshes could be composed of triangular elements or quadrangular, in two-dimensional, while three-dimensional elements could be of tetrahedra or hexahedrons. An example of unstructured mesh is shown in Figure 3.2.

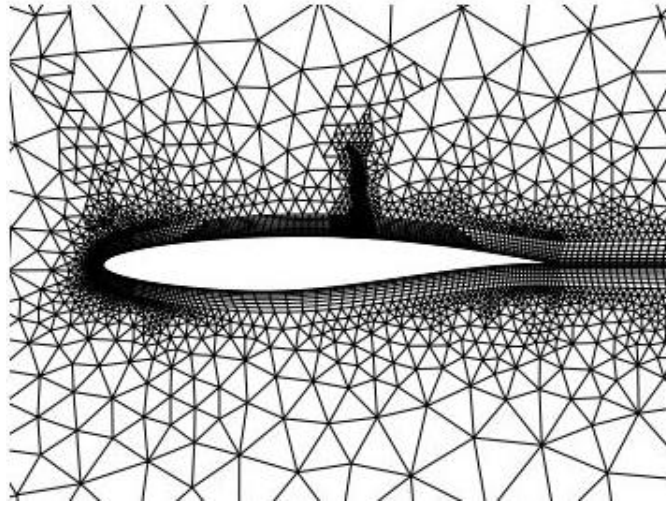


Figure 3.2 Unstructured mesh around an airfoil [18].

The advantage of an unstructured mesh is its high level of flexibility when it is built around a complex geometry. However, unstructured meshes require more memory to store information of explicit connectivity because neighbouring nodes in physical space are stored in non-neighbouring location in the memory. Moreover, elements are not aligned with the flow, so the solution could be less accurate than with a structured mesh.

3.1.3. Hybrid Mesh

It is possible to combine the two types of mesh obtaining hybrid mesh, using structured cells near wall regions to have an accurate solution there and unstructured cells in the rest of the domain. The advantage is to use structured mesh in the regions that need them and unstructured mesh where nothing relevant happens in the flow. The disadvantages are that this type of mesh requires user experience and it is less robust. A Hybrid mesh was used for the entire 3D BWB body mesh, which is a complex geometry.

3.2. Governing Equations

The governing equations of a continuous, viscous, compressible, Newtonian fluid flow are the Navier-Stokes equations. They are a set of partial differential equations that describe the relationship between the velocity, pressure, temperature and density of a moving fluid. They represent the conservation laws of physics, indeed they are derived by applying the mass conservation principle to obtain continuity equation (3.1), by applying Newton's second law to obtain conservation of momentum (3.2), by applying the first law of thermodynamics to obtain conservation of energy (3.3). These are the equations that Fluent solves to provide the numerical simulations [19].

$$\frac{\partial \rho}{\partial t} + \nabla \cdot (\rho \mathbf{u}) = 0 \quad (3.1)$$

$$\frac{\partial (\rho \mathbf{u})}{\partial t} + \nabla \cdot (\rho \mathbf{u} \otimes \mathbf{u} + p \mathbf{I} - \boldsymbol{\tau}) = 0 \quad (3.2)$$

$$\frac{\partial (\rho e_0)}{\partial t} + \nabla \cdot \rho \mathbf{u} h_0 = \nabla \cdot (-\mathbf{q} + \boldsymbol{\tau} \cdot \mathbf{u}) \quad (3.3)$$

These are the unsteady, three dimensional Navier-Stokes equations written in Cartesian tensor form and in conservation form. The variables $\boldsymbol{\tau}$, e_0 , h_0 and \mathbf{q} are respectively the viscous stress tensor, the specific total energy, the specific stagnation enthalpy, and the conduction heat flux vector.

$$e_0 = e + \frac{\mathbf{u} \cdot \mathbf{u}}{2} \quad (3.4)$$

$$h_0 = e_0 + \frac{P}{\rho} \quad (3.5)$$

$$\mathbf{q} = -k \nabla T \quad (3.6)$$

$$\boldsymbol{\tau} = \mu_l(\nabla\mathbf{u} + \mathbf{u}\nabla) + \lambda\nabla \cdot \mathbf{u} \quad (3.7)$$

Where c_p , c_v and k are respectively the gas constant pressure specific heat, the constant volume specific heat, and constant of thermal conductivity. Moreover, μ_l is molecular viscosity that could be estimated by Sutherland's law and λ is called the bulk viscosity.

In aerodynamic applications, the following relation holds:

$$\lambda = -\frac{2}{3}\mu_l \quad (3.8)$$

It is necessary to close the system of equations because there are five equations, and the unknowns that are present in the equations are seven: ρ , u , v , w , p , e , T . It is assumed that the gas behaves like a perfect gas, so that the sixth equation is the perfect gas law:

$$p = \rho RT \quad (3.9)$$

The seventh equation links the thermodynamics variables, for a perfect gas the specific heats are constant, so that the seventh equation is:

$$e = c_v T \quad (3.10)$$

These equations are non-linear, so no closed form solution exists. Computational Fluid Dynamics is the method to replace them with a system of approximate algebraic equations that are able to model the flow with complex physics and around complex geometries, predicting their development and evolution over time.

3.3. Turbulence

This phenomenon of turbulence arises at high Reynolds numbers. It is a random process, so it is very difficult to predict and it contains different scales. This phenomenon is characterized by a cascade process, in which small scale eddies are produced (via eddy stretching) from larger ones. Energy is extracted from the mean flow by the large-scale motions and is transmitted down through smaller and smaller scales until it is dissipated by viscous action at the smallest scales (Kolmogorov scale) into thermal energy. The size of the large scales is generally determined by the flow conditions and body characteristic length. The smallest dissipative scales become smaller at larger Reynolds numbers. It is necessary to capture all physical processes of turbulence to have better fidelity in numerical results. This means that computational domain should have dimensions larger than full scale length, which is a measure of the major eddy sizes in the flow and the grid cell should have the dimensions of Kolmogorov scale. The estimation of the relationship between length scale of the smallest eddies and full scale is $1/Re^{\frac{3}{4}}$. In addition, the time-step of the simulation should reproduce in an accurate way the dynamic behaviour of the minor scales and the relationship between Kolmogorov time scale and temporal full scale is $1/Re^{\frac{1}{2}}$. According to these considerations the computational cost is prohibitive. The difficulty to compute the instantaneous flowfield because of the limited memory of computers makes necessary the use of a statistical approach, so Reynolds-averaged Navier-Stokes (RANS) equations are considered in the solution. They are obtained applying Reynolds decomposition, in which the variables of the Navier-Stokes equations are divided into a time-averaged term and a fluctuating component in the following way:

$$\mathbf{u} = \bar{\mathbf{u}} + \mathbf{u}' \quad (3.11)$$

where mean value $\bar{\mathbf{u}}$ is the average of instantaneous quantities and fluctuating term \mathbf{u}' is the fluctuation from its respective average. These RANS equations are written in following way:

$$\frac{\partial \bar{\rho}}{\partial t} + \nabla \cdot (\bar{\rho} \bar{\mathbf{u}}) = 0 \quad (3.12)$$

$$\begin{aligned} \frac{\partial (\bar{\rho} \bar{\mathbf{u}})}{\partial t} + \nabla \cdot (\bar{\rho} \bar{\mathbf{u}} \otimes \bar{\mathbf{u}} + \bar{p} \mathbf{I} - \bar{\boldsymbol{\tau}} - \bar{\rho} \overline{\mathbf{u}' \otimes \mathbf{u}'}) \\ = 0 \end{aligned} \quad (3.13)$$

$$\begin{aligned} \frac{\partial \bar{\rho} (\bar{e}_0 + \bar{k})}{\partial t} + \nabla \cdot \bar{\rho} \mathbf{u} (\bar{h}_0 + \bar{k}) \\ = \nabla \cdot (-\bar{\mathbf{q}} + \bar{\boldsymbol{\tau}} \cdot \bar{\mathbf{u}} - \overline{\rho \mathbf{u}' h'}) - \bar{\rho} \overline{\mathbf{u}' \otimes \mathbf{u}' \cdot \bar{\mathbf{u}}} \end{aligned} \quad (3.14)$$

Where \bar{k} is averaged kinetic energy:

$$\bar{k} = \frac{1}{2} \bar{\mathbf{u}} \cdot \bar{\mathbf{u}} \quad (3.15)$$

The term $-\bar{\rho} \overline{\mathbf{u}' \otimes \mathbf{u}'}$ that appears is the Reynolds stress tensor $\bar{\boldsymbol{\tau}}_r$, that is the flux of momentum due to turbulent fluctuations. According to Boussinesq theory the Reynolds stress tensor is modelled by the following equations:

$$\bar{\boldsymbol{\tau}}_r = \mu_t \left(\nabla \bar{\mathbf{u}} + \bar{\mathbf{u}} \nabla - \frac{2}{3} \mathbf{I} \nabla \cdot \bar{\mathbf{u}} \right) - \frac{2}{3} \bar{\rho} \bar{k} \mathbf{I} \quad (3.16)$$

Where μ_t is eddy viscosity and so the total viscosity is:

$$\mu = \mu_t + \mu_l \quad (3.17)$$

Additional relations are needed due to new variables derived by the averaging, thereby further increasing computational cost, and some of these turbulence models to permit that system of equations to be closed include:

- The Spalart-Allmaras (S-A) is a one equation turbulence model and the equation is a transport equation for the kinematic eddy (turbulent) viscosity.
- The $k-\omega$ model is a two-equation turbulence model and these two equations are partial differential equations for the variables k , that is turbulence kinetic energy production and for ω which is the specific rate of dissipation of the turbulence kinetic energy into internal thermal energy.
- The $k-\varepsilon$ model is a two-equation turbulence model that describes turbulence with a relationship about k , which is the turbulence kinetic energy and about ε that is the rate of dissipation of turbulence energy. It is used to model the boundary layer far from the wall.
- The Shear stress transport (SST) formulation combines the best qualities of $k-\omega$ and $k-\varepsilon$. The $k-\varepsilon$ model is not able to capture the correct behaviour of turbulent boundary layers with adverse pressure gradients and so does not predict accurately the behaviour for separated flow, while $k-\omega$ is too affected by inlet turbulence and free-stream boundary conditions.

3.4. The Boundary Layer

The boundary layer of a turbulent flow is divided into three sublayers:

- The viscous sublayer that is the closest region near the wall and where friction viscous effect prevails
- The buffer layer where the influence of turbulence and viscosity is the same.

- The Log-law layer where the viscosity is neglected, and the flux is considered completely turbulent.

In these regions the variables are defined as non-dimensional velocity U/u_τ and non dimensional distance from the wall y^+ . Where:

$$u_\tau = \sqrt{\frac{\tau_\omega}{\rho}} \quad (3.18)$$

$$y^+ = \frac{y u_\tau}{\nu} \quad (3.19)$$

Here u_τ is friction velocity and τ_ω is shear stress of the wall. The distribution of these parameters in these regions and the trend of the non-dimensional velocity is represented in Figure 3.3.

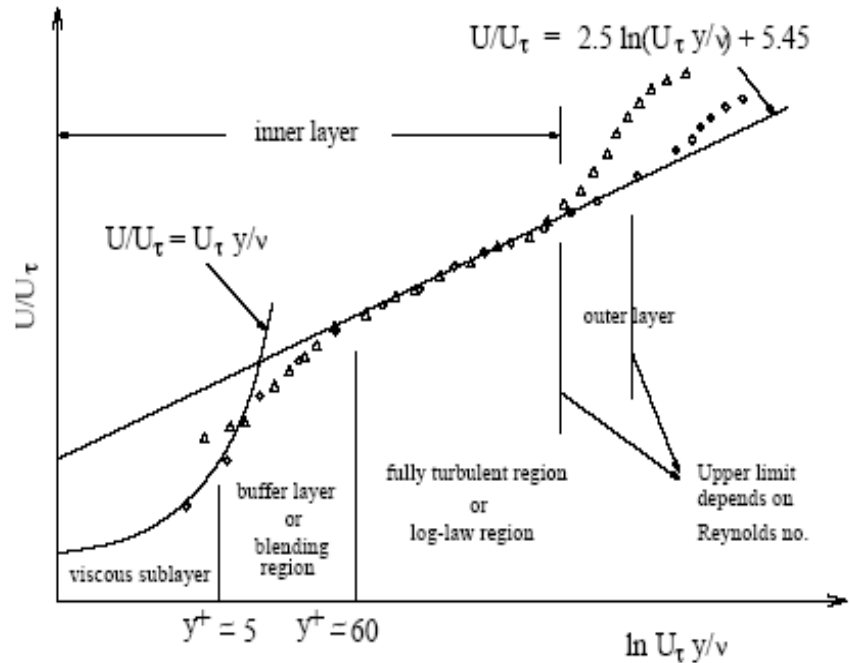


Figure 3.3 Subdivision of near Wall Region [18].

According to these definitions, there are two methods to model turbulence near the wall – the Near-Wall Model and the Wall Function Approach. In the first approach the sub-viscous layer is solved, so the length of first cell should be placed in the first sublayer, $y^+ < 5$. In the second method the viscous effect of the viscous sub-layer region is not solved to predict turbulent behaviour of the flux, but modelled. For this reason, the first cell should have a height greater than that of sub-viscous layer and buffer layer, $30 < y^+ < 200$. In this thesis the first method is employed to investigate the supercritical profile RAE2822 and the second method is used to analyse the full blended wing body configuration, due to the computational cost to reach $y^+ < 5$.

4 RESULTS AND DISCUSSIONS

In this sections results obtained for both the 2D case of a supercritical aerofoil and the 3D blended wing body case are presented.

4.1 Aerodynamic characteristics of a transonic aerofoil

The RAE (Royal Aircraft Establishment) 2822 is a supercritical aerofoil and its aim is to permit high speed flight with the same drag of a conventional aerofoil. The first step of aerodynamic analysis of the supercritical aerofoil, (which is represented in Figure 4.1) under the following condition of Mach number $M_\infty=0.729$, angle of attack $\alpha=2.31^\circ$, and $Re = 1.69 \cdot 10^7$, was the division of the domain in discrete control volumes (cells) by creating a computational grid.

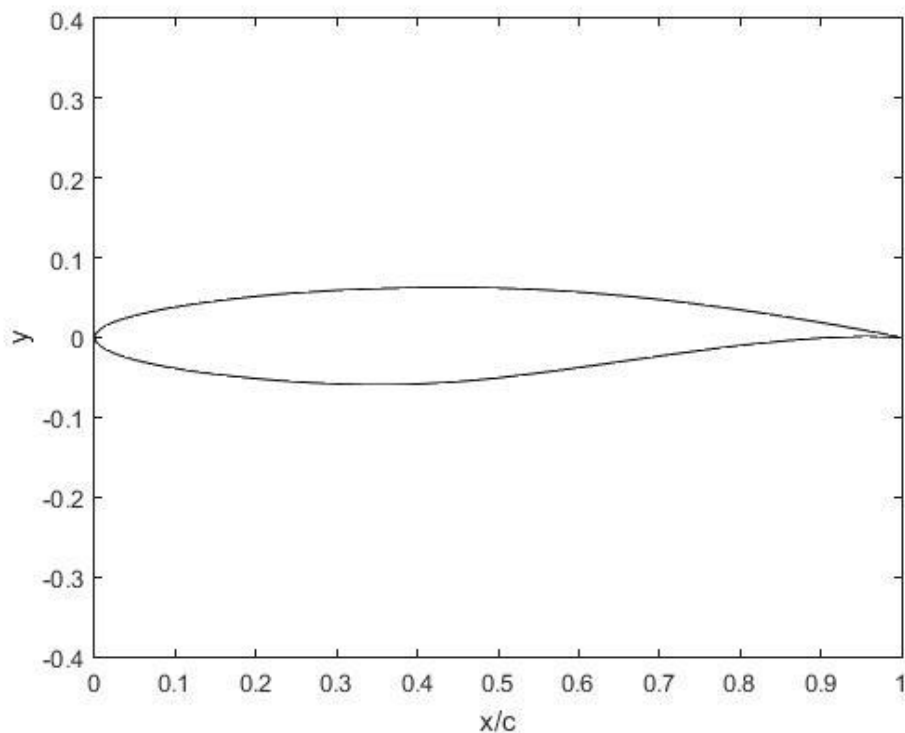


Figure 4.1 RAE2822 aerofoil.

4.1.1 Analysis with structured mesh over the aerofoil RAE2822

Firstly, before starting the mesh generation, a rough estimation of the height of the first cell y_p , to obtain $y^+ < 1$ over the curve of the aerofoil, was calculated at about $10^{-6}m$. For this reason, two different Meshes characterized by this value of y_p have been analysed with different turbulence models. Both meshes have been adapted in the position near the shock. The main difference between them was the number of cells. The two meshes tested were named Mesh A and Mesh B.

4.1.1.1. Generation of structured mesh

After the geometry of the aerofoil was imported in ICEM, fixing the origin of axes to the leading edge of the analysed aerofoil, the domain of the far-field was built. In both meshes its dimensions were from $15c$ to $20c$ along the x-axis and from $-15c$ to $15c$ along the y-axis, where c is the length of the aerofoil chord. The domain has been divided into blocks (Figure 4.2) and the mesh has been generated, selecting the number of nodes on all edges of the domain and over the curves of the aerofoil.

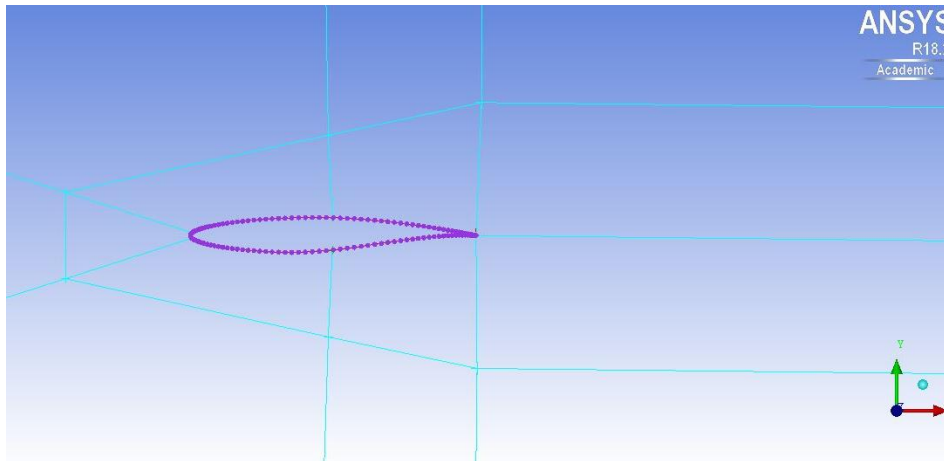


Figure 4.2 Domain divided into blocks.

The number of nodes has been chosen clustering the mesh on the curves of the aerofoil, near the leading edge and trailing edge and in the wake region to capture relevant physical phenomena of the flow. Therefore, cells dimensions grow along the radial direction with the ratio of 1.2. Mesh A, which is shown in Figure 4.3, has a maximum aspect ratio cell of $3.38 \cdot 10^4$, which is a measure of the stretching of a cell. This is a high value, because it is usual to have an aspect ratio up to around 100, but the mesh has been designed in this way to have a low y^+ over the curves of the profile.

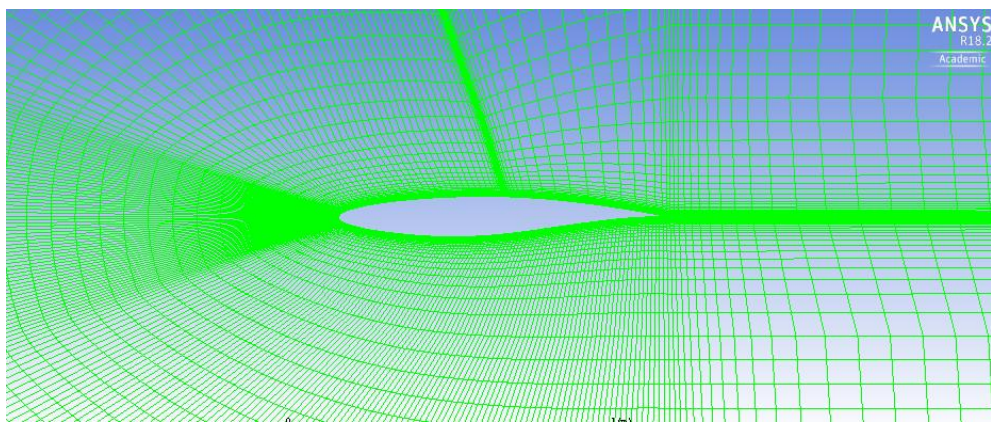


Figure 4.3 Mesh A.

The maximum aspect ratio of Mesh B is $6.59 \cdot 10^4$, which is higher than the value of Mesh A and this is the reason for why y^+ of Mesh B (shown in Figure 4.4) is lower.

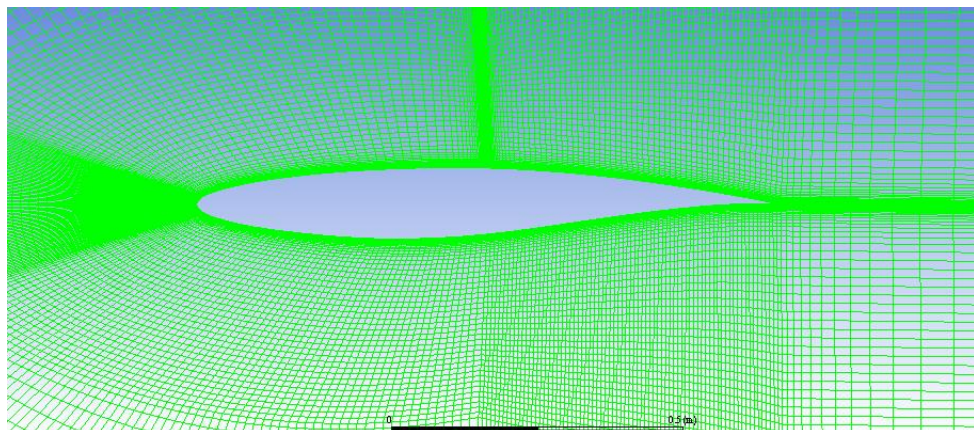


Figure 4.4 Mesh B.

4.1.2. Setup and post processing

Each cell represents a control volume where the numerical code Fluent has to solve the integrated governing equations with a discretisation process, using a finite-volume approach. The finite-volume approach discretisation process means integrating governing equations on each control volume and constructing an algebraic system of linearized equations to get unknown variables such as temperature, velocities, pressure and other conserved scalars. The discretisation process used here was density-based and the solver was a steady-state solver. Steady-state solvers assume that time marching proceeds until a steady-state solution is reached. Density-based methods are mainly used for high-speed compressible flow, while pressure-based is for low-speed incompressible flows. The velocity field is obtained from the momentum equations in both numerical methods, the density field is obtained from the continuity equations and the pressure field is determined from the equation of state in the first method, while in the second one the pressure field is obtained from a pressure correction equation which is the result of momentum and continuity equation manipulations. Due to the non-linearity of the resulting system of equations, many iterations are required to obtain convergence in results. Steps of each simulation are i) the initialization of the flow, ii) the solving simultaneously of the continuity momentum and energy equations and then iii) solving the equations for scalars. The iteration process continues until the absolute convergence criteria or the fixed number of iterations are reached. The manner in which the governing equations are linearized could be explicit or implicit. Explicit means the unknown variables are computed in each cell using only existing values of these variables from the neighbouring cells calculated at the previous step, so each unknown quantity appears in only one relation that could be solved alone in each cell, while implicit unknown variables in each cell are computed using both existing values calculated at previous steps and unknown values of these variables from the neighbouring cells, so equations must be solved

simultaneously. In the analysis of the RAE aerofoil an implicit method has been used due to its faster convergence in the solution and reasonable memory required. The spatial discretisation scheme was accurate to the second order so quantities at cell faces have been computed with a multidimensional linear reconstruction through Taylor series expansion and it has been accomplished with an upwind spatial scheme. The Courant number selected as solution control was 5. The ideal gas law together with a Sutherland viscosity law was used. Boundary conditions set were pressure-far field for the domain free-stream, this condition models a free-stream conditions at infinity (Mach number and static pressure conditions) and wall for the curves, which means a solid surface in the flow field where a viscous no-slip condition is enforced on the wall setting the velocity components to zero.

Plotting the distribution of pressure coefficient (figure 4.5) obtained at the end of the iteration process for both meshes analysed with different turbulence models, it is noticeable that the SA turbulence model gives a distribution of pressure closer to the experimental data and to VGK results. All the meshes can predict the interaction between shock wave and boundary-layer. In front of the shock the velocity is supersonic, descending into the boundary layer the velocity progressively decreases up the point where $u=a$ and $M=1$. Below the sonic line the information can travel upstream, consequently this interaction causes a pressure rise before the shock. Moreover, aft loading associated the aft chamber is correctly predicted.

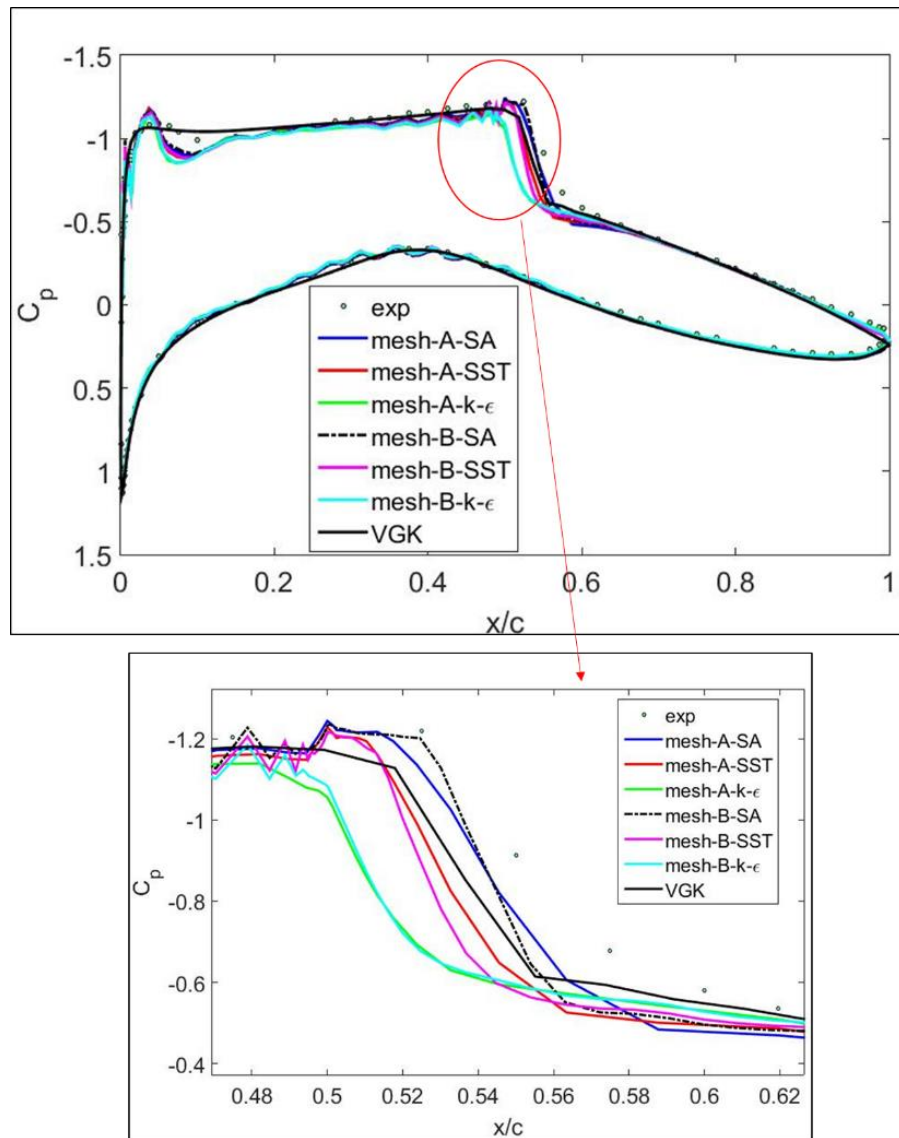


Figure 4.5 C_p distribution on the aerofoil RAE2822.

The shock, which is located in $x/c \approx 0.5$, is also visible in the Mach contour which clearly shows the supersonic flow becoming subsonic (figure 4.6).

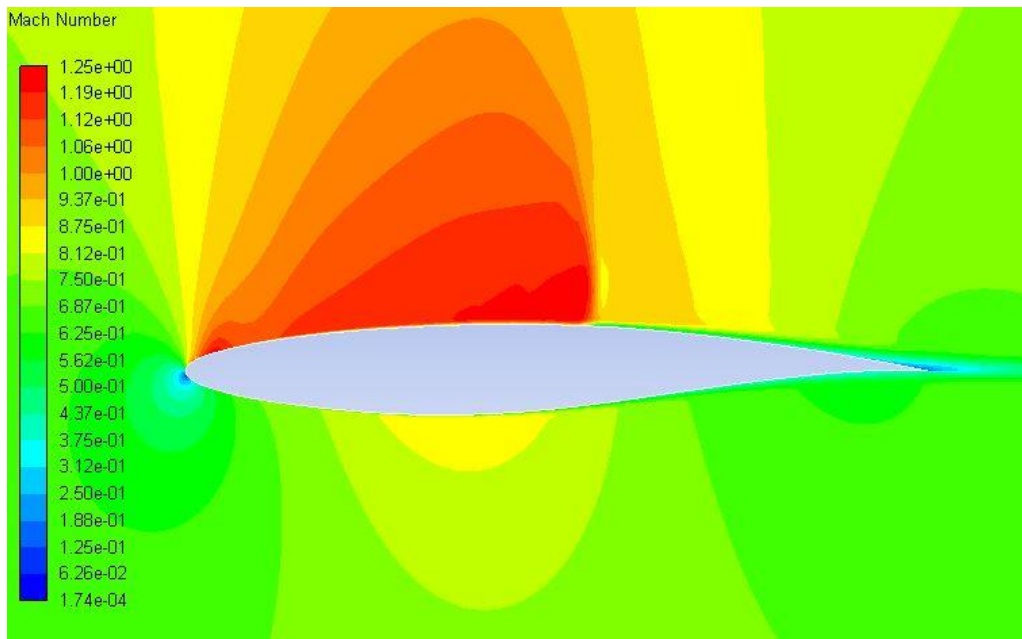


Figure 4.6 Mach number distribution computed with the Spalart Allmaras model and for mesh B.

Comparing all simulations, it is possible to conclude, from Figure 4.5, that the mesh B analysed with the Spalart-Allmaras turbulence model. represents the turbulent flux most accurately. Results of different simulations for Mesh A and for Mesh B are shown in table 4.1 and table 4.2.

Table 4.1 Aerodynamic Results for Mesh A.

		<i>Mesh A</i>			
<i>Cell Number</i> 173,892	Turbulence Model	y^+	C_l	C_d	
	SA	1.5	0.717	0.0138	
	SST	1.5	0.698	0.0128	
	k- ϵ	1.5	0.680	0.0158	
	Experiment	-	0.743	0.0127	

Table 4.2 Aerodynamic Results for Mesh B.

Mesh B				
Cell Number 350,084	Turbulence Model	y^+	C_l	C_d
	SA	0.25	0.718	0.0139
	SST	0.25	0.694	0.0128
	k- ϵ	0.30	0.681	0.0156
	Experiment	-	0.743	0.0127

The value of y^+ is an average value of the values over the entire aerofoil. The entire profile of y^+ over the curves is shown in figure 4.7.

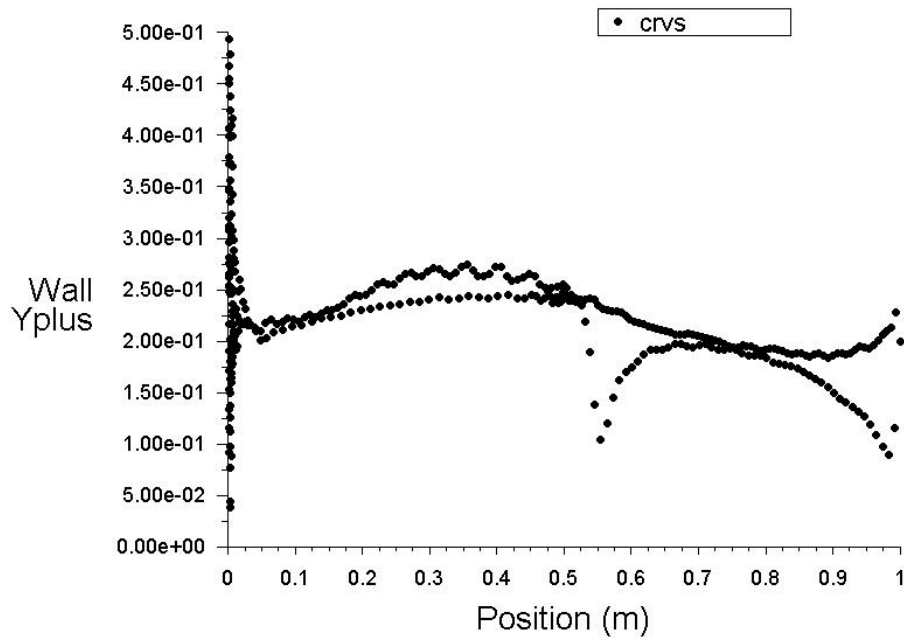


Figure 4.7 y^+ profile on the aerofoil surface calculated with the Spalart Allmaras model and for mesh B.

For both meshes, the results have been obtained fixing absolute convergence criteria of 10^{-6} for all the residuals (continuity equation, momentum equation, energy equation and of the additional equations that close the system). Furthermore, the value of maximum number of iterations was fixed at 1000, given that they were enough to reach a smooth convergence. All simulations stopped before reaching the absolute convergence criteria but reached an acceptable order of magnitude of $10^{-3}/10^{-4}$ (figure 4.8). In addition, convergence history of drag coefficient and lift coefficient are reported in figure 4.9 and figure 4.10.

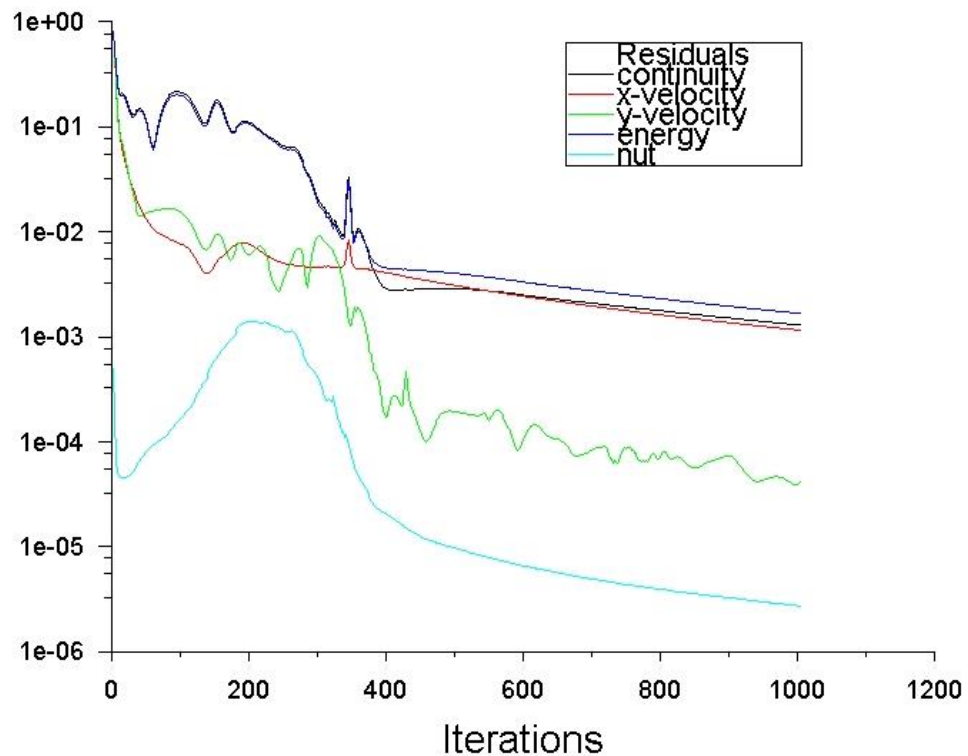


Figure 4.8 Residuals of the iteration process for mesh B and Spalart Allmaras turbulence model.

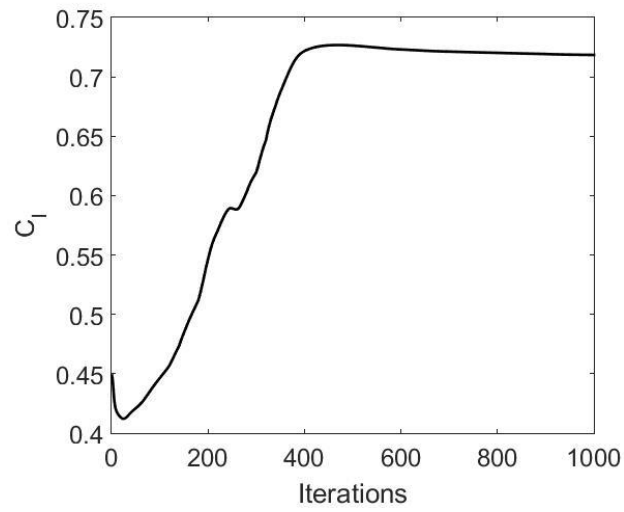


Figure 4.9 Lift coefficient convergence history.

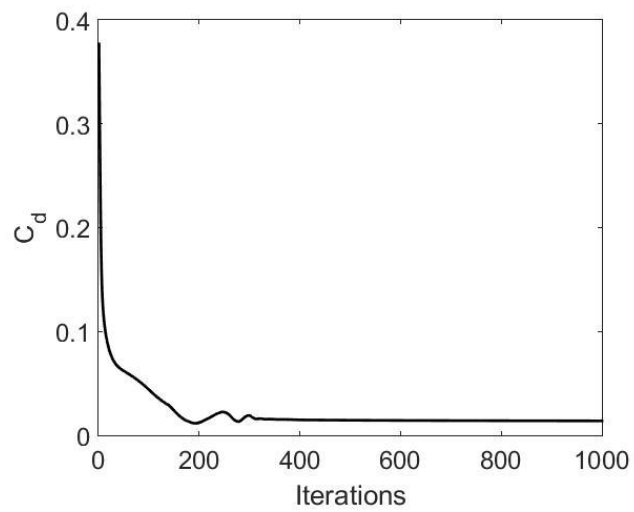


Figure 4.10 Drag coefficient convergence history.

4.2. Analysis with unstructured mesh over the aerofoil RAE2822

An unstructured mesh over the aerofoil RAE2822 was generated to compare results with the structured mesh in order to choose which approach was best used for the 3D blended wing body case.

4.2.1. Generation of unstructured mesh

After the geometry of the aerofoil was imported in ICEM, fixing the origin of axes to the leading edge of the analysed aerofoil, the same domain of the far-field described in the previous case was built. A surface over the far field curves was created and was cut to generate two different surfaces. The surface inside the aerofoil was deleted to avoid having cells inside, as shown in figure 4.11.

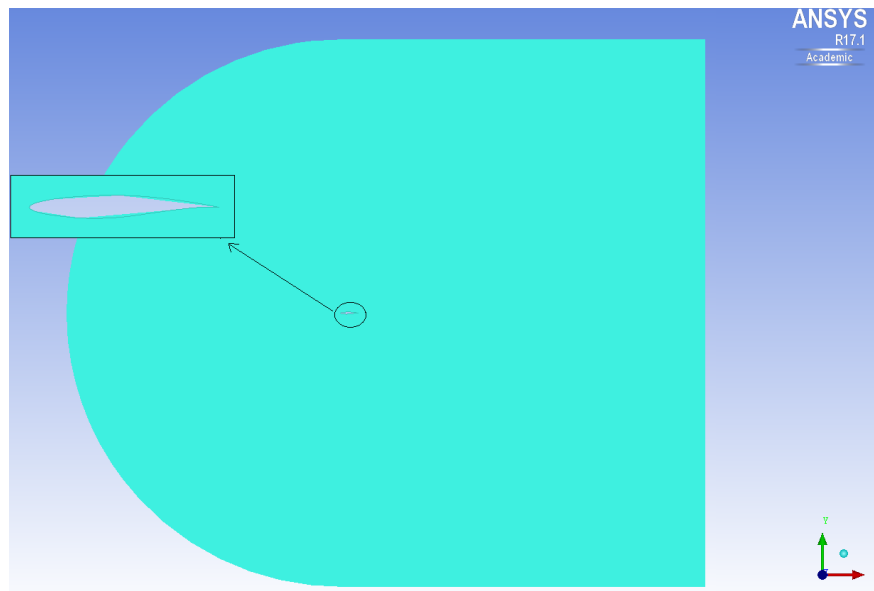


Figure 4.11 Far field surface cut.

The next step was setting the boundary conditions and maximum cell sizes for the far field curves and part fluid, which contained the surface. The maximum cell size on the domain edge was established as 0.08, while for the curves of the aerofoil the maximum cell size was set to 0.0068 and the number of nodes was 150 for each curve. Moreover, a BiGeometric clustering with ratio of 1.2 was used to provide more nodes at the trailing edge and leading edge because these have more pronounced curvatures. The internal

mesh was computed using All Tri as the mesh type, and it is illustrated in figure 4.12.

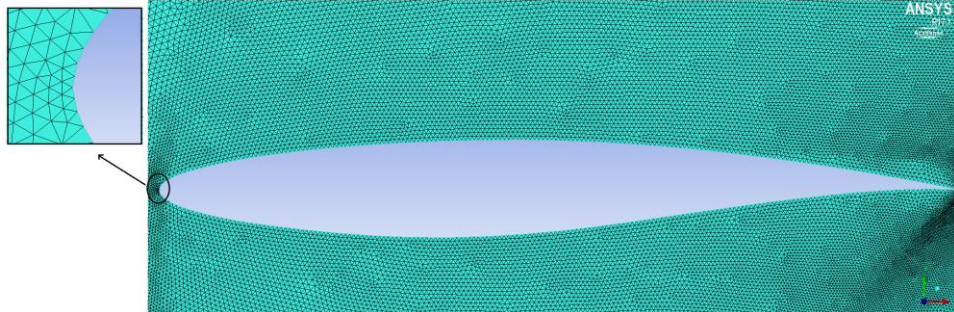


Figure 4.12 Unstructured mesh over the aerofoil RAE2822.

4.2.2. Setup and postprocessing

The behaviour of the flow has been simulated using the same setup of the structured mesh case using different turbulence models and the results have been compared. Looking at the results (figure 4.13 and table 4.3), it is possible to conclude that an unstructured mesh gives values close to values obtained with a structured mesh. The unstructured mesh presents oscillations because it is sensitive at the curvature, especially in supersonic flow where the information does not travel upstream.

Table 4.3 Comparison of results obtained by VGK, unstructured mesh and structured mesh.

	Turbulence model	C_l	C_d
Experiment	-	0.743	0.0127
Mesh B	SA	0.718	0.0139
Unstructured Mesh	SST	0.756	0.0135
Unstructured Mesh	k- ϵ	0.744	0.0144
Unstructured Mesh	SA	0.660	0.0123
VGK	Integral BL Eqns.	0.702	0.0123

The analysis of different flow conditions requires a lot of computing time, despite the use of 16 processors of a High Performance Computing (HPC) cluster, which aggregates computing power in a way that delivers much higher performance, so an unstructured / hybrid mesh was chosen for the 3D analysis of the blended wing body for its simplicity and to avoid spending too much time in generating the mesh. Obviously, the accuracy is lower with an unstructured mesh approach, but it represents the right compromise between getting physical fidelity in the results and the computational time cost. Therefore, an unstructured mesh gives less accuracy, but is easier to be built and it makes simulations faster. Nevertheless, using an unstructured mesh strategy makes it more difficult to reach low values of y^+ . Indeed, in the unstructured mesh generated around the RAE2822 aerofoil, the aspect ratio is 5.14 and so this is why a hybrid mesh, which consists of prism layers around the body and unstructured mesh far from the body, has been used for the 3D analysis.

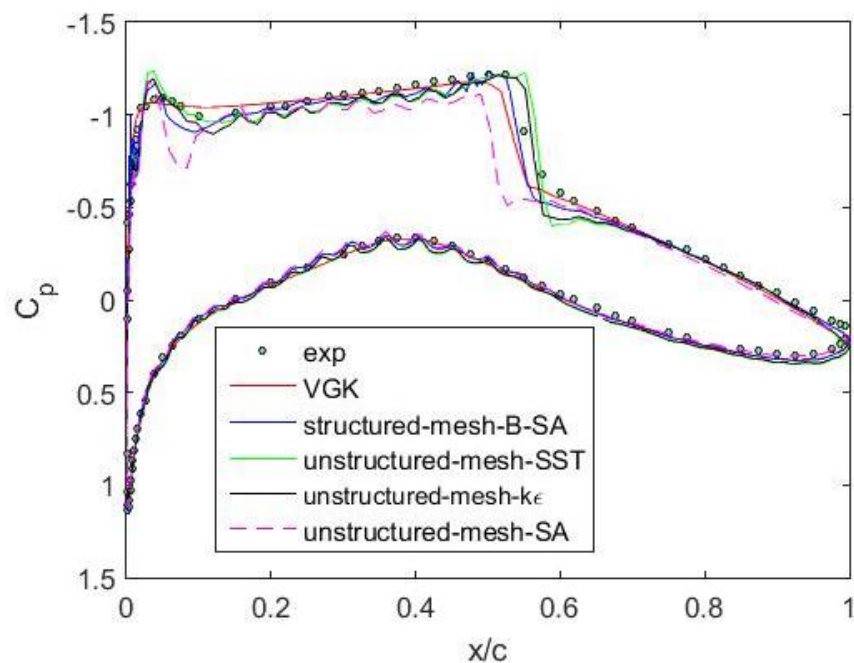


Figure 4.13 Comparison of C_p distribution obtained by VGK, Structured Mesh and Unstructured mesh.

4.2 BW11 CFD analysis

The analysed Blended Wing Body is represented in figure 4.14. In this section the transonic aerodynamic performance of the baseline model are predicted, and it has been analysed for different Mach numbers and angles of attack, maintaining fixed Reynold number.

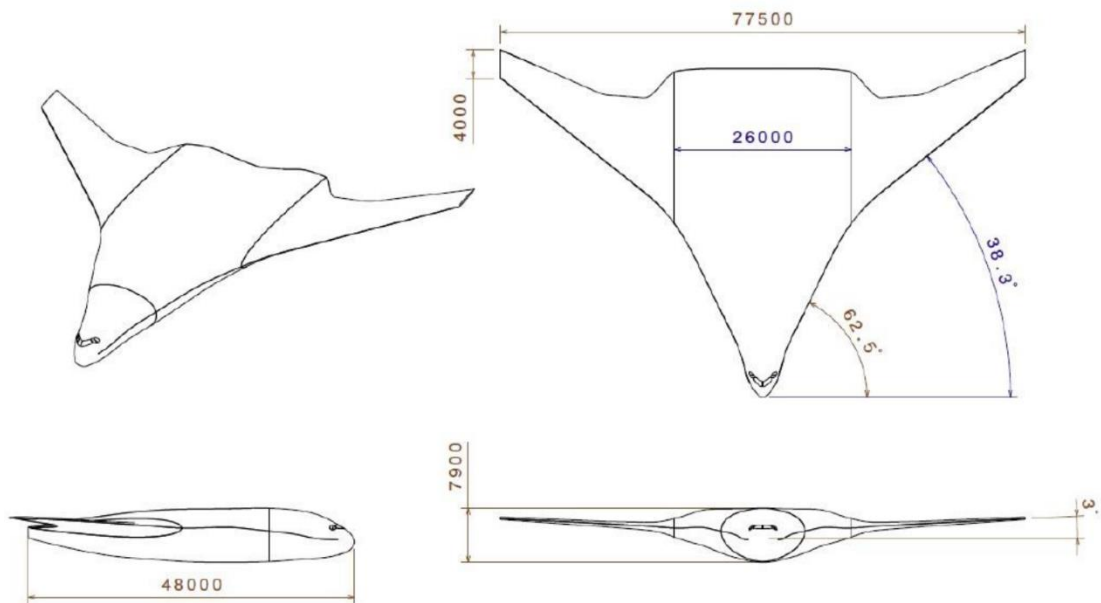


Figure 4.14 Main views of the BW11 Eagle Ray baseline model used for the aerodynamic analysis [20].

4.2.1 Mesh generation

To get started, the CAD model was imported in ICEM (figure 4.15) to allow generation of the mesh. The aircraft model was cut according to the symmetry of the plane, and a symmetry boundary condition to reduce the computational cost, as only the longitudinal aerodynamic characteristics were of interest in this study.

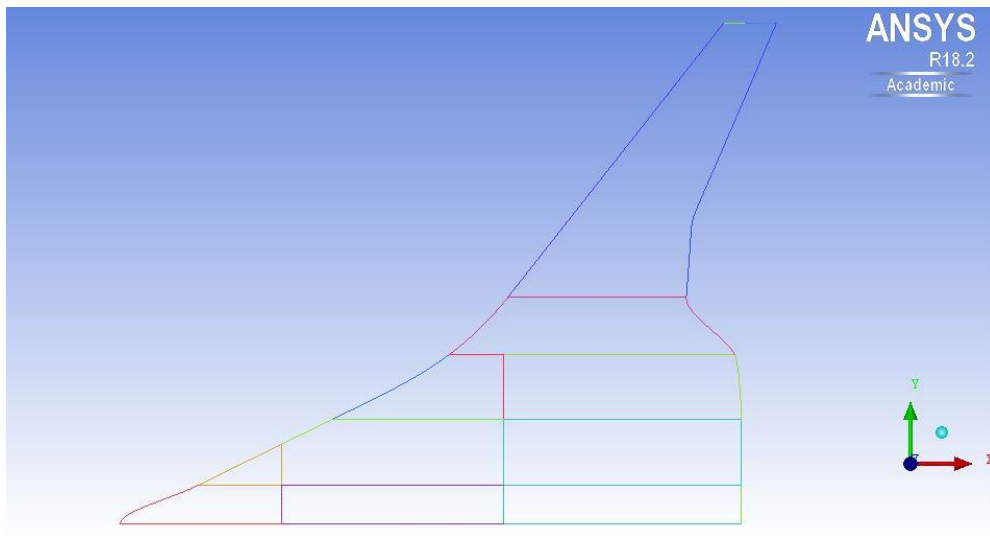


Figure 4.15 BW11 baseline model.

The engines and winglets have not been included to simplify the geometry and to reach a better mesh quality. The model has been cleaned of double curves to avoid problems in mesh generation. Surfaces were assembled in different parts as shown in figure 4.16. This division allowed different mesh sizes in each part and so the grid in the trailing edge was finer. This approach reduced the computational cost.

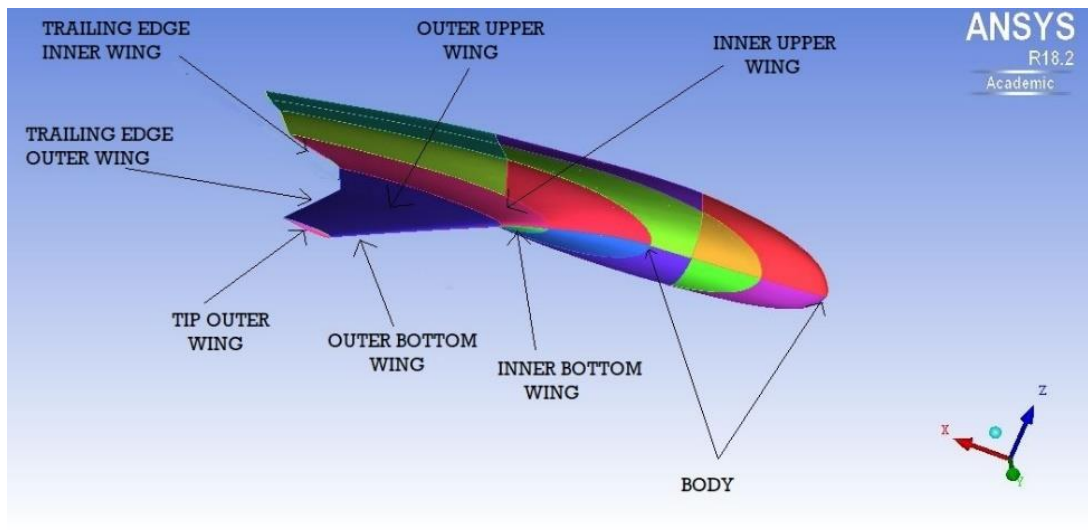


Figure 4.16 Parts of geometry division in ICEM.

After that, the domain, the virtual space which represented the environment around the aircraft, was built. The origin of the axis system was set at the nose of the aircraft, with x-axis along the body, y-axis along the span of the model and z-axis being vertically upwards as shown in figure 4.17.

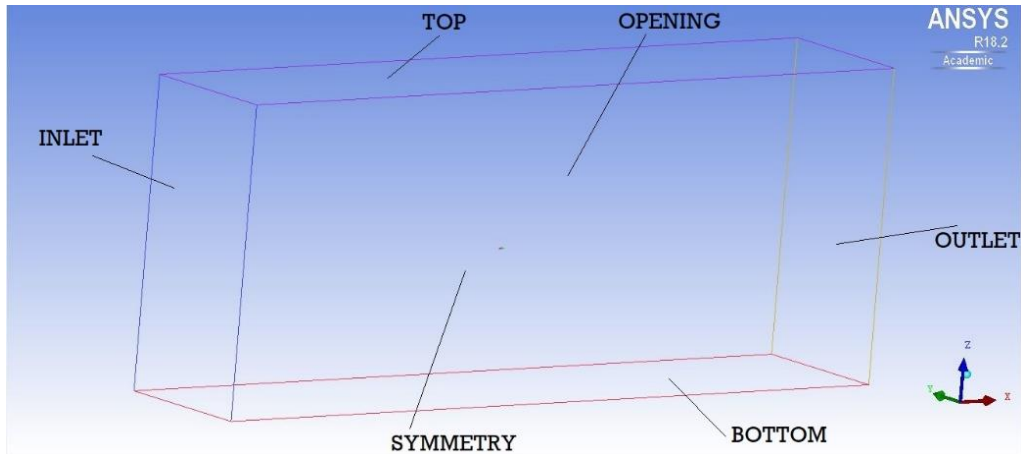


Figure 4.17 Domain.

The domain had the following dimensions related to the half span length of the aircraft:

- X direction: the edge was 150 times the half span length, 60 times the half span length far from the INLET and 90 times the half span length far from the OUTLET
- Y direction: the edge was 30 times the half span length with the SYMMETRY face in $y=0$
- Z direction: the edge was 60 times the half span length, and the nose of the aircraft was placed at 30 times the half span length.

The next step was defining the global parameters of the mesh to limit the size of elements and deciding the type of mesh. The maximum element size was chosen as 100. The mesh type used was Tetra/Mixed unstructured mesh, it was generated using the Robust Octree method [21]. At the beginning the mesh sizes was 0.5m for all the parts of the aircraft and 100

m for all the parts of the domain, but then in some parts of the blended wing body, especially on the tip of the outer wing and the trailing edge, the size has been decreased to cover correctly all the model with small enough cells to resolve the flow features, as shown in figure 4.18.

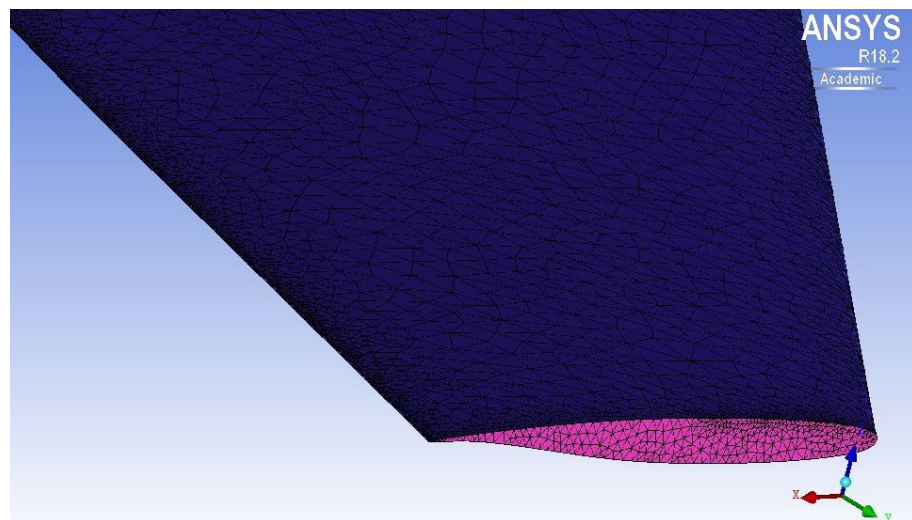


Figure 4.18 Refinement of the mesh at the trailing edge.

The reason of this refinement of the mesh was that trailing edge mesh definition is a critical factor, especially when a boundary layer has to be resolved [22]. Once the mesh parameters were set, the volumetric mesh was computed, giving 1,466,554 cells (figure 4.19).

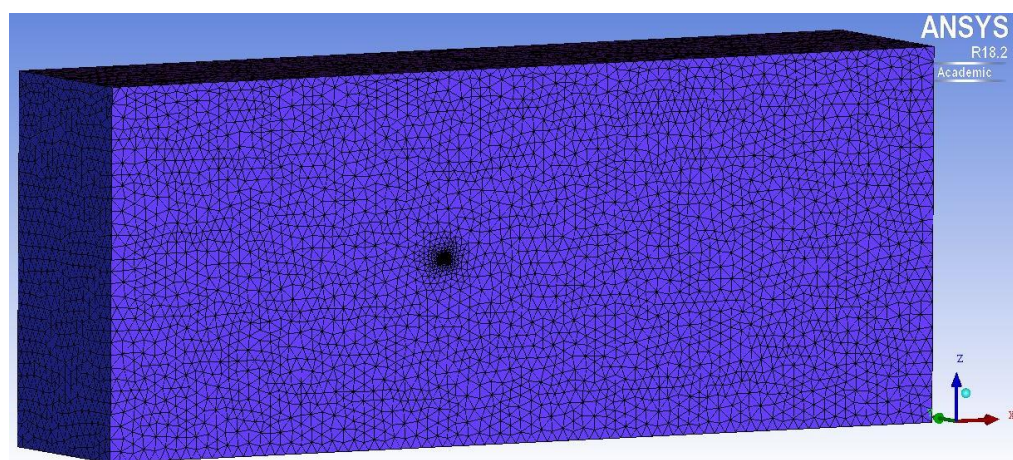


Figure 4.19 Unstructured Volumetric Mesh.

In figure 4.20 the tetra elements can be distinguished and the detail of the mesh growth ratio moving far from the aircraft is shown.

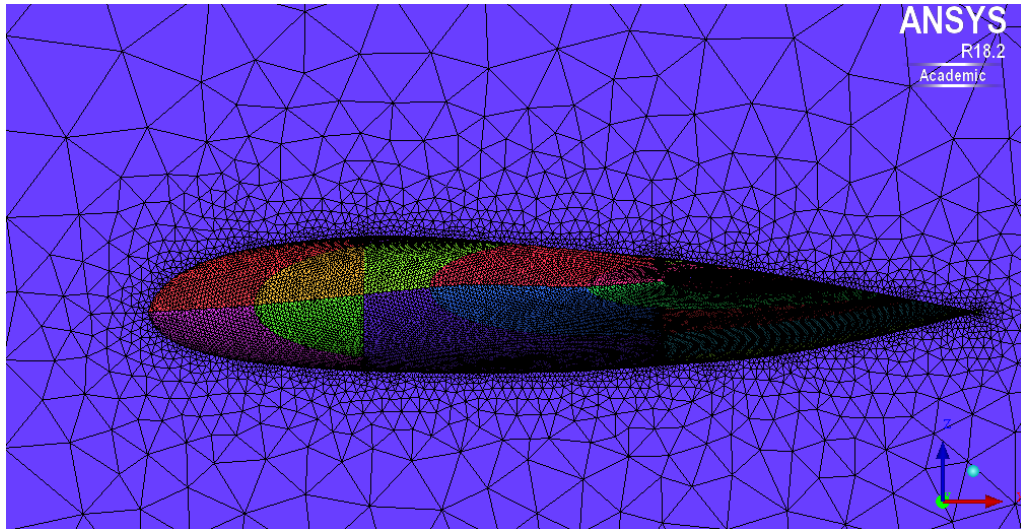


Figure 4.20 Detail of unstructured volumetric mesh (side view).

Furthermore, the preliminary fine mesh needed to be finer near the boundary layer of the body for a reasonable prediction of drag and of viscous effects. For this reason, a prism mesh over the surface of the blended wing body was computed (figure 4.21). The choice of boundary layer parameters depends on the method desired to model turbulence near the wall. Due to a low required y^+ , the choice of the height of the first prism layer was $5 \cdot 10^{-5}$, this value was about $5 \cdot 10^{-6}$ times the half span of the blended wing body. The number of the prism layers was 30 and the growth ratio was 1.2. After adding this prism layers the number of cells became 3,866,903.

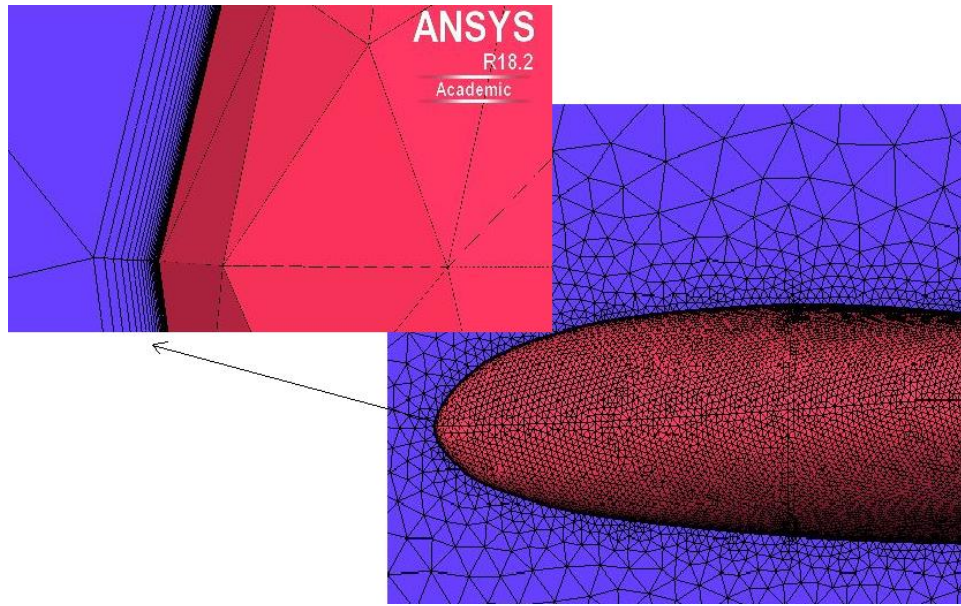


Figure 4.21 Detail of prism layer mesh.

Once the mesh had been imported in fluent, the boundary layer mesh was adapted - this means that the prismatic cells for the boundary layer were split to increase their number. Therefore, simulations have been computed on a mesh with 18,797,156 cells. Regarding the mesh quality, maximum aspect ratio was $5.63 \cdot 10^4$ and this high value has been accepted because the required y^+ was very low. Minimum orthogonal quality was below 0.01, where its range is from 0 to 1, but values close to 0 correspond to low quality. Maximum ortho-skewness was $9.99 \cdot 10^{-1}$, where its range is from 0 to 1, but values close to 0 correspond to low quality. Therefore, mesh quality needed to be repaired, this improvement was executed in fluent using the following command: */mesh/repair-improve/improve-quality*.

4.2.2 Setup

All simulations have been run under the following conditions. The solver was the 3D double precision, density-based and steady state solver. The linearization started with an explicit method with Courant number of 0.7 which was kept for 1000 iterations and then the calculations proceeded using

implicit linearization with Courant number equal to 2 to have faster convergence. When simulations were stopped, the residuals were about 10^{-4} . The second order upwind scheme was chosen for the spatial discretisation. The $k\omega$ -SST turbulence model was selected because the mesh had been built with a very low height of the first cell according the requirement of low y^+ , but it was not less than 5, so Spalart Allmaras model was not the better one to use. The ideal gas law was implemented and viscosity was computed using the three coefficient Sutherland law. Furthermore, boundary conditions were applied to the model and, the domain being consistent with the high-speed compressible flow, these were:

- The symmetry boundary condition was used on the body symmetry plane to reduce the computational. On this plane the normal gradients of all variables and normal velocity are zero.
- The wall boundary condition was used to define a solid region where, due to the viscous flow no-slip condition, all components of the velocity are zero.
- The Pressure-far field boundary condition was applied at all faces of the domain except for the symmetry plane. This condition models the free-stream condition at infinity, so Mach number, static pressure and angle of attack have been defined. In the simulations the Reynolds number has been maintained constant and equal to $Re=7.75 \cdot 10^8$ and the value of Mach has been changed. The CFD analysis has been performed for $M_\infty = 0.7$, $M_\infty = 0.75$ and $M_\infty = 0.8$. Temperatures, needed for the different Mach Numbers and reported in the table 5.1, have been computed by manipulating the following equations:

$$Re = \frac{\rho v c}{\mu} \quad (4.1)$$

$$a = \sqrt{\gamma RT} \quad (4.2)$$

$$M = \frac{v}{a} \quad (4.3)$$

$$P = \rho RT \quad (4.4)$$

$$\mu = \mu_o \left(\frac{T}{T_{ref}} \right)^{3/2} \left(\frac{T + S}{T_{ref} + S} \right) \quad (4.5)$$

where $P=101325$ Pa, $c=50$ m which is the half span of the blended wing body, and S is a constant whose value for air is 110.4K.

Table 4.4 Physical quantities corresponding at different Mach numbers.

M_∞	T (K)	a (m/s)	u (m/s)	μ (Kg/m s)	ρ (Kg/m ³)
0.7	300	347	243	$1.85 \cdot 10^{-5}$	1.18
0.75	316.7	357	268	$1.92 \cdot 10^{-5}$	1.12
0.8	333.5	366	293	$2 \cdot 10^{-5}$	1.06

4.2.3 Aerodynamic characteristics

In this section the aerodynamic results obtained with Ansys Fluent for the BW11 are shown for the different Mach Numbers and for several angles of

attack. Results for $M=0.75$ are compared with a coarse mesh, which has about 14,000,000 of cells to demonstrate how aerodynamic performance analysed with CFD are sensitive to the mesh characteristics. At the end of all the simulations, the values of lift, drag, pitching moment and C_L/C_D coefficients have been computed, and these are shown in the table 4.5, table 4.6, table 4.7 and table 4.8.

Table 4.5 C_L , C_D , C_M and C_L/C_D , corresponding at different angles of attack at $M_\infty=0.7$, fine mesh.

$M_\infty=0.7$, fine mesh				
α [°]	C_L	C_D	C_M	C_L/C_D
0	0.044	0.0060	-0.069	7.4
0.5	0.084	0.0064	-0.132	13.1
1	0.111	0.0069	-0.104	16.1
1.5	0.150	0.0078	-0.182	19.3
2	0.180	0.0088	-0.215	20.4
3	0.238	0.0118	-0.283	20.1

Table 4.6 C_L , C_D , C_M and C_L/C_D , corresponding at different angles of attack at $M_\infty=0.75$, fine mesh.

$M_\infty=0.75$, fine mesh				
α [°]	C_L	C_D	C_M	C_L/C_D
0	0.063	0.0062	-0.083	10.1
1	0.121	0.0070	-0.147	17.2
2	0.185	0.0090	-0.221	20.5
3	0.254	0.0134	-0.302	19.0

Table 4.7 C_L , C_D , and C_L/C_D , corresponding at different angles of attack at $M_\infty=0.75$, coarse mesh .

$M_\infty=0.75$, coarse mesh			
α [°]	C_L	C_D	C_L/C_D
0	0.054	0.0061	8.9
2	0.194	0.0093	20.8
4	0.328	0.0191	17.2
6	0.411	0.0369	11.2

Table 4.8 C_L , C_D , C_M and C_L/C_D , corresponding at different angles of attack at $M_\infty=0.8$, fine mesh.

$M_\infty=0.8$, fine mesh				
α [°]	C_L	C_D	C_M	C_L/C_D
0	0.0644	0.0063	-0.085	10.2
0.5	0.0981	0.0068	-0.124	14.4
0.75	0.1151	0.0072	-0.143	16.0
1	0.132	0.0076	-0.163	17.4
1.5	0.1664	0.0086	-0.203	19.3
2	0.1993	0.0101	-0.240	19.7
3	0.2674	0.0147	-0.317	18.2

From the values given in table 4.5, table 4.6 and table 4.7, the curves which describe the aerodynamic behaviour of BW11 have been obtained. Figure 4.22 shows the lift coefficient curve versus angle of attack

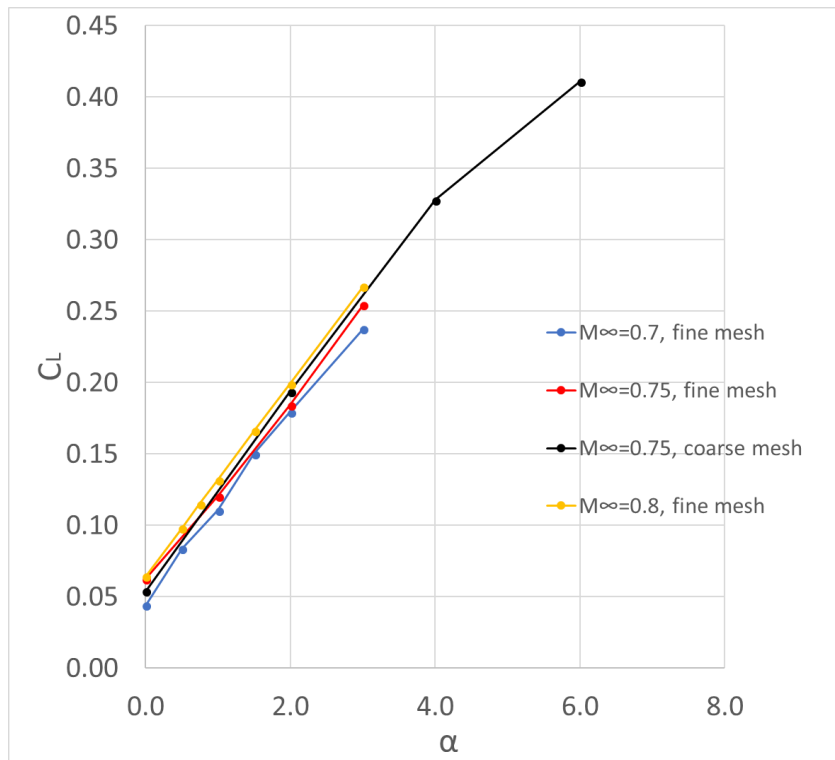


Figure 4.22 C_L versus α at different Mach numbers.

Interpolating the values of the linear part of the lift curves, their equations have been computed (table 4.9).

$$C_L = C_{L0} + C_{L\alpha} \cdot \alpha \quad (4.6)$$

Table 4.9 Equations of linear part of lift curves corresponding at the different Mach numbers.

$M_\infty=0.7$, fine mesh	$C_L = 0.048 + 0.064 \cdot \alpha$
$M_\infty=0.75$, fine mesh	$C_L = 0.060 + 0.064 \cdot \alpha$
$M_\infty=0.75$, coarse mesh	$C_L = 0.055 + 0.069 \cdot \alpha$
$M_\infty=0.8$, fine mesh	$C_L = 0.064 + 0.068 \cdot \alpha$

From these equations, values of lift coefficients at 0° angle of attack (C_{L0}) and lift curve slope ($C_{L\alpha}$) have been obtained. And finally, the zero-lift angle of attack (α_{0Lift}) have been computed.

$$\alpha_{0Lift} = -\frac{C_{L0}}{C_{L\alpha}} \quad (4.7)$$

All the values are reported in table 4.10.

Table 4.10 C_{L0} , $C_{L\alpha}$, and α_{0lift} at different Mach numbers.

	C_{L0}	$C_{L\alpha}$	α_{0lift} [°]
$M_\infty=0.7$, fine mesh	0.048	0.064	-0.75
$M_\infty=0.75$, fine mesh	0.060	0.064	-0.93
$M_\infty=0.75$, coarse mesh	0.055	0.069	-0.80
$M_\infty=0.8$, fine mesh	0.064	0.068	-1.05

From these values it is clear that the aerodynamic results are sensitive to the mesh characteristics. In figure 4.23 the effect of the angle of attack on the drag coefficient can be observed. For low angles of attack the curves are very close, but when $\alpha=1.5^\circ$ the curve corresponding at $M_\infty=0.8$ rises sharply. Given that the CFD analysis of BW11 has been carried out for three Mach numbers, these were not enough to allow interpolation to compute the M_{DD} . However, C_D grows gently until $\alpha=1.5^\circ$ for $M_\infty=0.8$ and until $\alpha=2^\circ$ for $M_\infty=0.75$, hence the sharp rise of drag was thought to appear at $M_\infty=0.77$ at $\alpha=2^\circ$. Therefore, CFD analysis in these flow conditions have also been carried out, C_D values corresponding to the different Mach numbers are represented in figure 4.24, for $\alpha=2^\circ$.

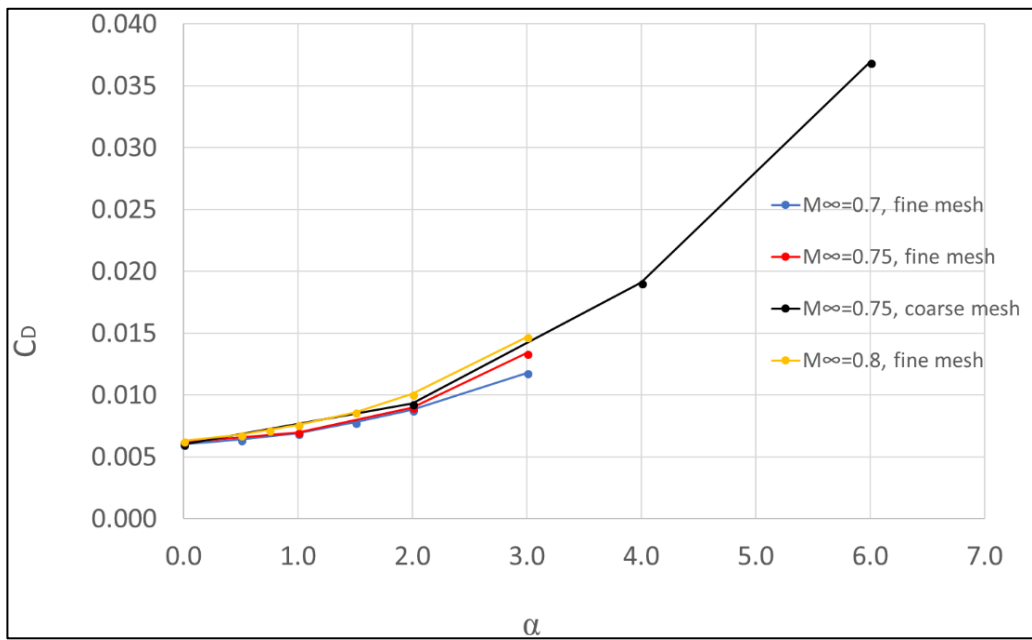


Figure 4.23 C_D versus α at different Mach numbers.

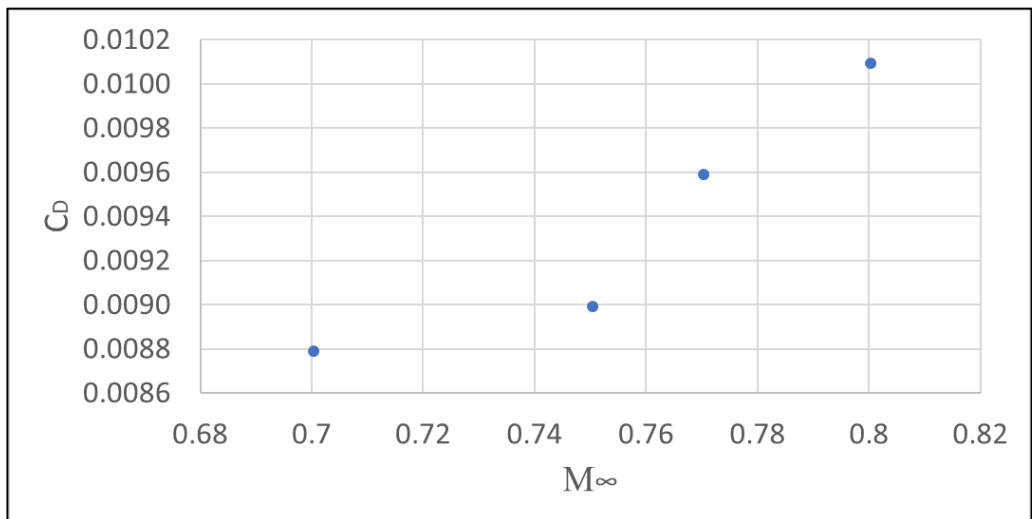


Figure 4.24 C_D versus M_∞ at $\alpha=2^\circ$.

From the plot of the lift coefficient versus drag coefficient the 'parabolic drag polar' can be obtained for each Mach number (figure 4.25 and figure 4.26).

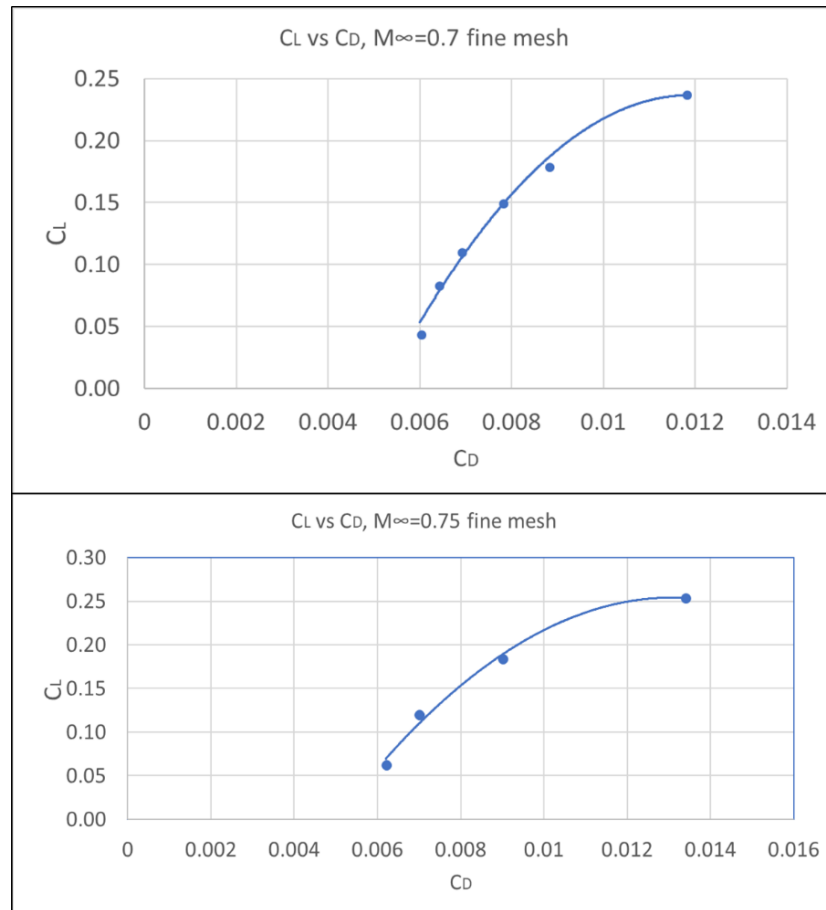


Figure 4.25 C_L versus C_D curve at $M_\infty=0.7$, fine mesh and $M_\infty=0.75$, fine mesh.

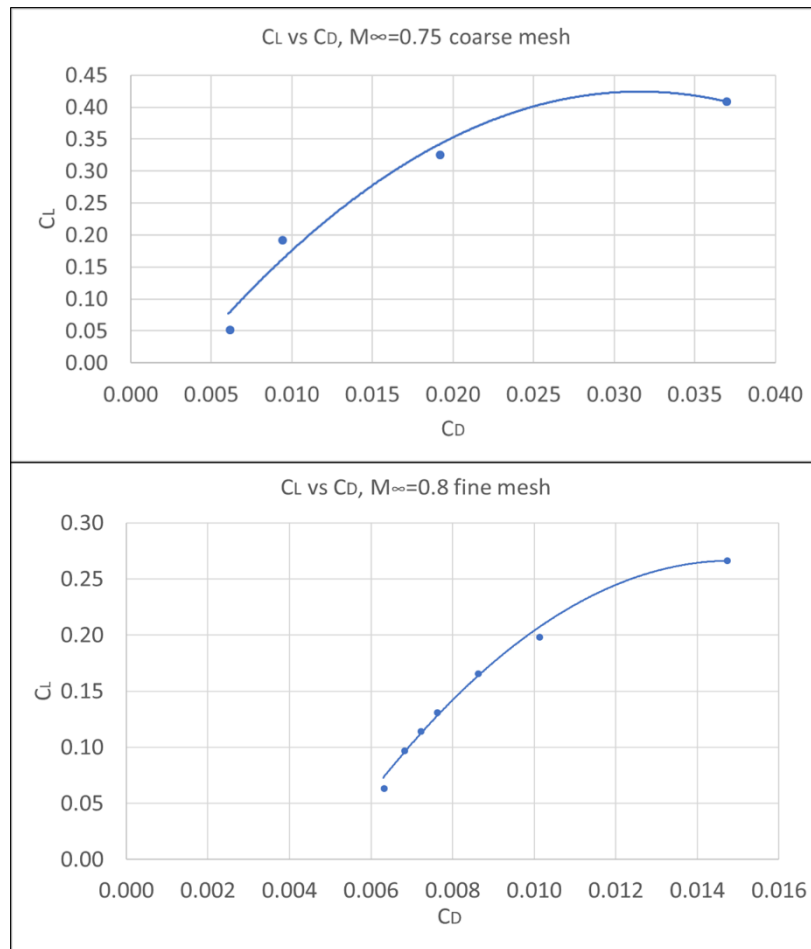


Figure 4.26 C_L versus C_D curve at $M_\infty=0.75$, coarse mesh and $M_\infty=0.8$, fine mesh.

In order to see the evolution of the aerodynamic efficiency with the increase of the angle of attack and to find the maximum ratio of C_L/C_D , which is a measure of maximum aerodynamic efficiency, the Lift-to-drag ratio versus angle of attack curve has been plotted for each Mach number. These are shown for the fine mesh in figure 4.27.

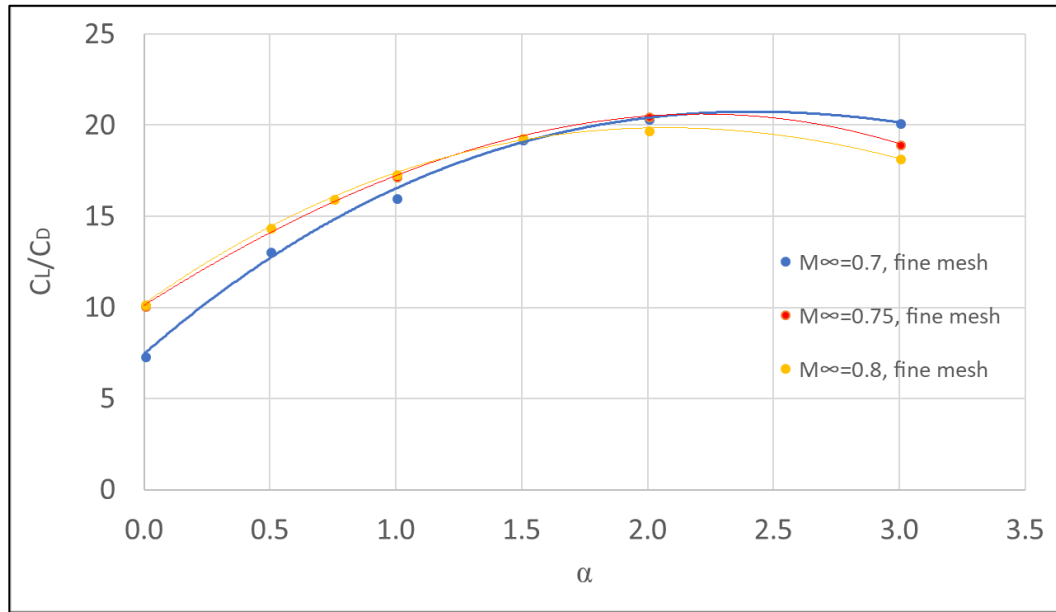


Figure 4.27 C_L/C_D versus α for each Mach number and fine mesh.

The aerodynamic efficiency goes up and reaches the maximum at the angle of attack included between 2° and 3° for all the Mach numbers, and for $M_\infty=0.7$ and $M_\infty=0.75$ it is up to 20. An approximate method for estimating the transonic performance of aerofoils is based on “the Korn equation,” which was an empirical relation developed by Dave Korn at the NYU Courant Institute of Mathematical Sciences in the early 1970s [16], and is given as:

$$M_{DD} + \frac{C_L}{10} + \left(\frac{t}{c}\right) = \kappa_A \quad (4.8)$$

where:

- M_{DD} drag divergence Mach number
- C_L is the lift coefficient
- t/c is the thickness to chord ratio

Thicker aerofoils create higher supervelocities over the upper and lower surfaces than a thin aerofoil. A thicker aerofoil will encounter critical conditions at lower free stream Mach number than a thin aerofoil. In general, this also results in an earlier onset of shock-induced boundary layer separation and therefore drag divergence. The increase in lift coefficient is a result of higher supervelocities on the suction side of aerofoils, which causes also an earlier formation of the shock wave and associated shock -induced separation. Therefore, with increasing lift coefficient the drag divergence Mach number decreases. Therefore, the Korn equation provides a simple means of estimating the possible combination of Mach, lift and thickness that can be obtained finding a compromise between high lift coefficient, large thickness to chord ratio and low and drag divergence Mach number. This relation can also be used to compare the transonic performance of aircraft – Airbus are known to use it as one of the measures of configuration performance. Considering $M_{DD}=0.77$, $C_L = 0.18$ corresponding at cruise condition of $\alpha=2^\circ$ and $M_\infty=0.75$, and t/c , which is an average on the BW11, the Korn technology factor (κ_A) could be estimated and its value was found to be 0.91. This value has been compared with the Korn factor computed for the RBC12 wing/body geometry designed by the Aircraft Research Association (ARA) which was representative of a 1990s aircraft, and was tested in the ARA Transonic Wind Tunnel [23]. Considering $M_{DD}=0.81$ and $C_L=0.4$ that is lift coefficient at cruise condition of $M_\infty=0.78$ and $\alpha=2^\circ$ is assumed, its value is 0.96. Therefore, the Korn factor is relatively good at lift coefficient $C_L = 0.18$ and $M_{DD}=0.77$ for the BW11. However, this value has an uncertainty, because the data indicates that for $\alpha=2^\circ$ the drag divergence Mach number is between 0.75 and 0.8, so the Korn factor is between 0.89 and 0.94. The stability characteristics of the BW11 design are also investigated, stability is particularly important because it is not immediately obvious how to achieve positive static margin for a BWB aircraft due to the absence of conventional empennage [24]. Moreover,

compressibility affects longitudinal static stability. The main goal is to maintain positive static margin at all flight conditions. Static margin (K_n) at each Mach number has been computed using Equation (4.9).

$$K_n = -\frac{C_{L\alpha}}{C_{M\alpha}} \quad (4.9)$$

$C_{M\alpha}$ is the pitching moment due to change in angle of attack, and it has been computed from the interpolations of the curves C_M versus α , showed in figure 4.28 for each Mach number, and the values are represented in table 4.11.

Table 4.11 Values of $C_{M\alpha}$ and K_n for each Mach number.

M_∞	$C_{M\alpha}$	K_n
0.7	-0.073	1.14
0.75	-0.073	1.14
0.8	-0.077	1.14

The decreasing of K_n , represented in figure 4.29, with the increase of Mach number is mostly because the flow changes from a flow with a weak shock to a flow with strong shock. The explanation for the reduction in stability is the movement of the aerodynamic centre forward caused by the separation which occurs behind the shock wave [25].

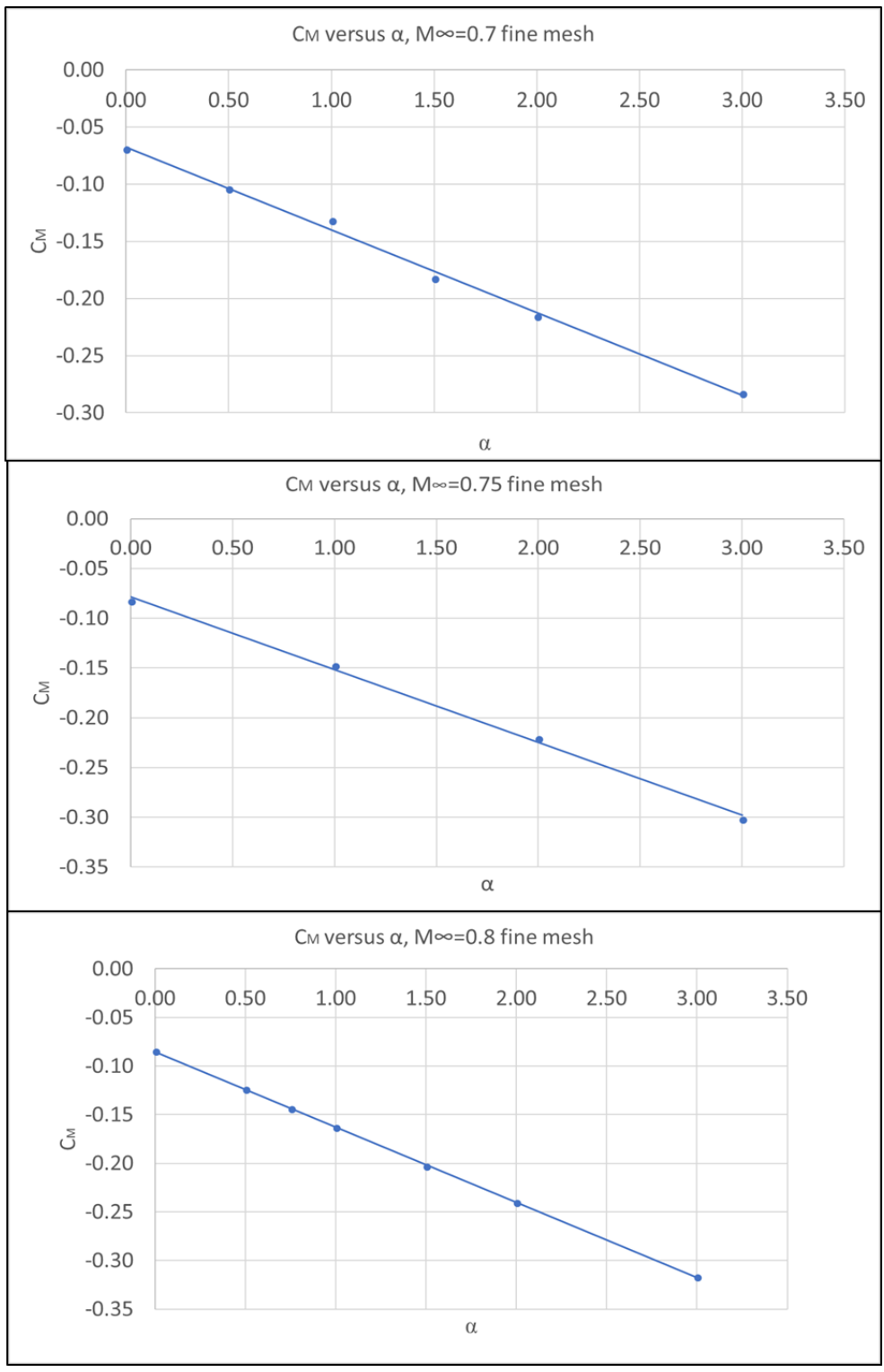


Figure 4.28 C_M versus α for each Mach number.

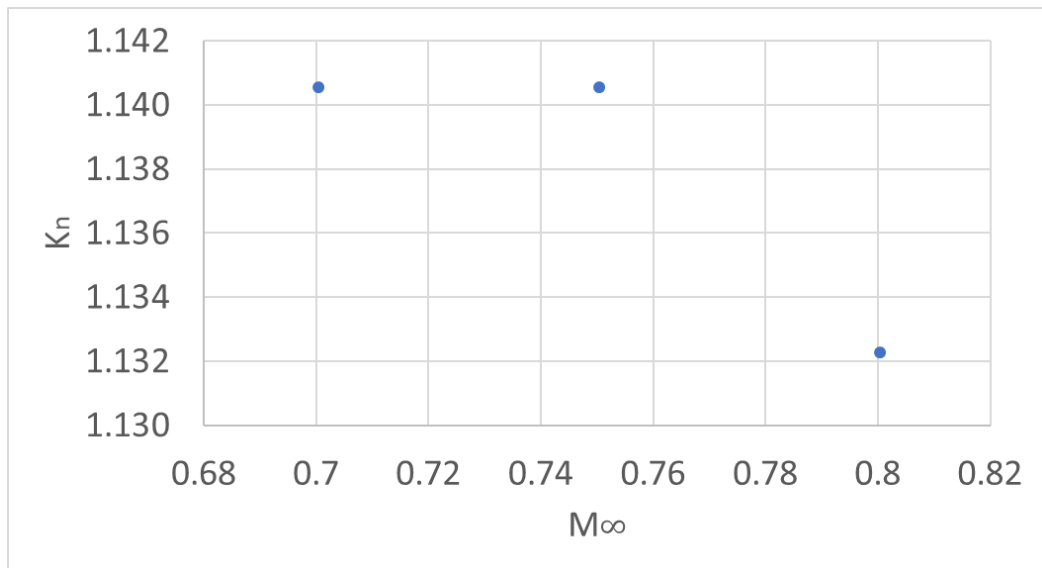


Figure 4.29 Static margin versus Mach number.

4.2.3.1 Pressure and Mach distribution

After that general aerodynamic behaviour of the aircraft has been analysed for different Mach numbers and different angles of attack, through the curves presented in the previous section, a deeper analysis of the aerodynamic effect in transonic conditions was carried out through analysis of the pressure and Mach distribution. Due to time limitation it was not possible to analyse pressure distributions for all flight conditions, so pressure distribution and Mach distribution have been studied in depth for only $\alpha=2^\circ$ and $\alpha=3^\circ$, for different Mach numbers, which are representative of cruise alphas. For $M_\infty = 0.75$ and $\alpha=2^\circ$, a weak shock wave is presented at the leading edge on the upper surface, indeed a sudden change in pressure coefficient at the leading edge of the outer wing is shown in the figure 4.30. This is the characteristic behaviour of a shock wave, which starts at the wingtip and extends up to the beginning of the body. In figure 4.31 the pressure coefficient distribution shows a stronger wave for $M_\infty=0.77$ and $\alpha=2^\circ$ and, as expected, its strength rises for $M_\infty=0.8$ (figure 4.32). However, in all cases the shock appears only on the top surface of the body and disappears at the crank between the body and the outer wing. Moreover, the shock is not curved, so the crank of the

wing works well. The pressure distributions on the top and bottom of the aft body are very similar, this means that this part does not contribute to lift generation.

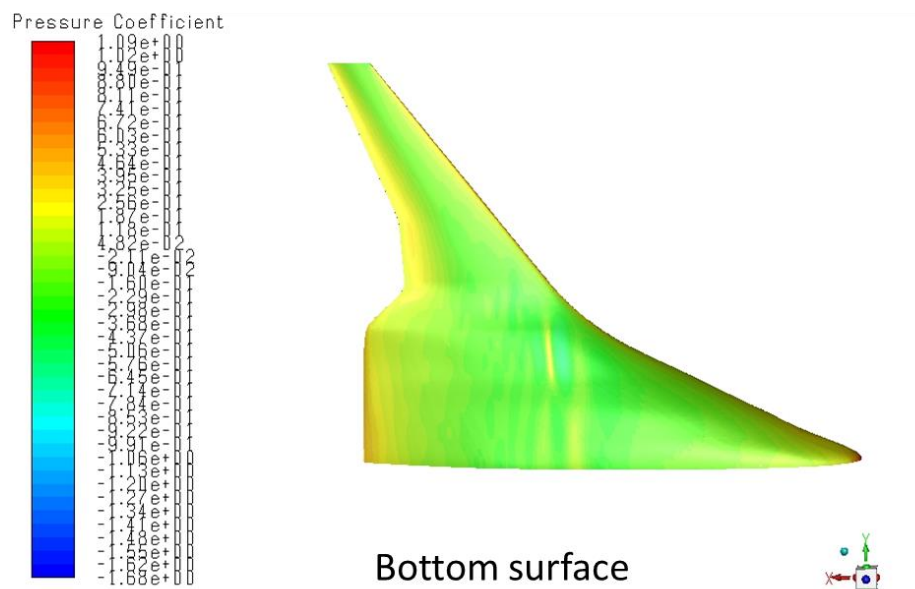
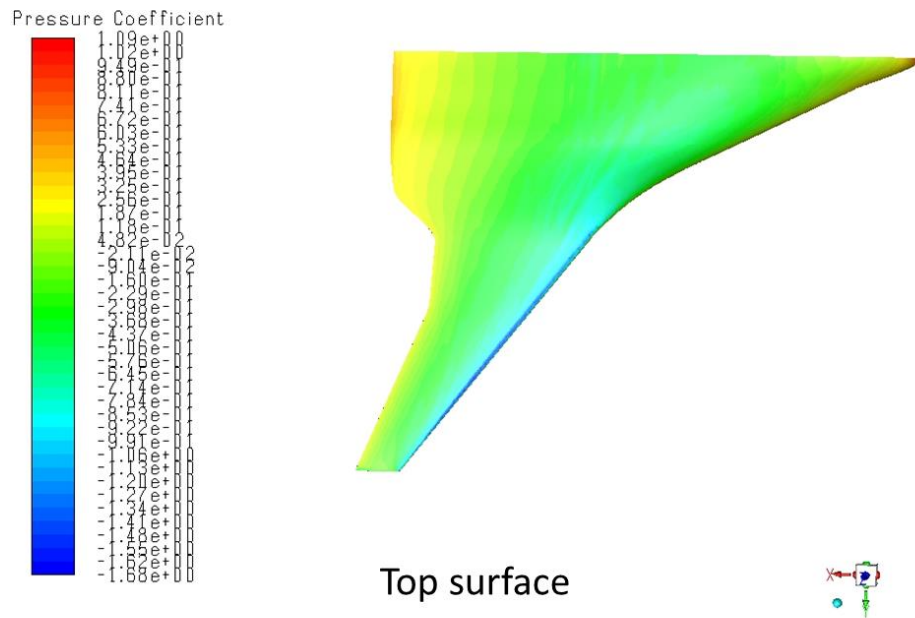
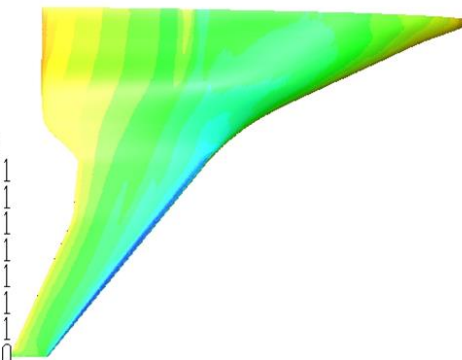
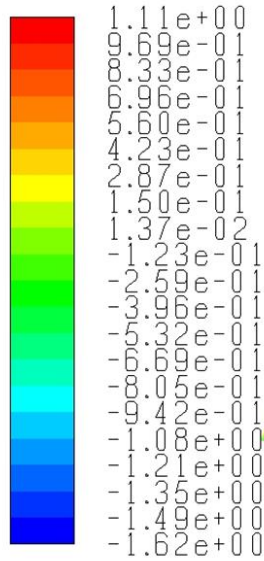


Figure 4.30 C_p distribution at $M_\infty=0.75$ and $\alpha=2^\circ$ on top and bottom surface of BW11.

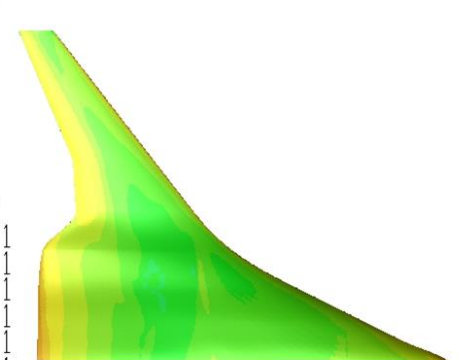
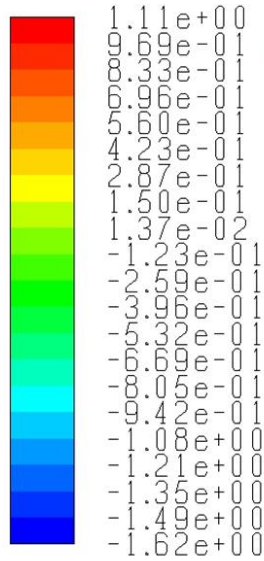
Pressure Coefficient



Top surface



Pressure Coefficient

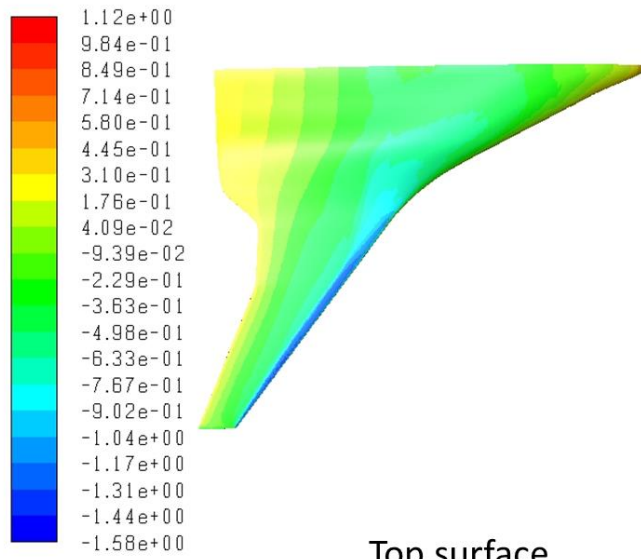


Bottom surface



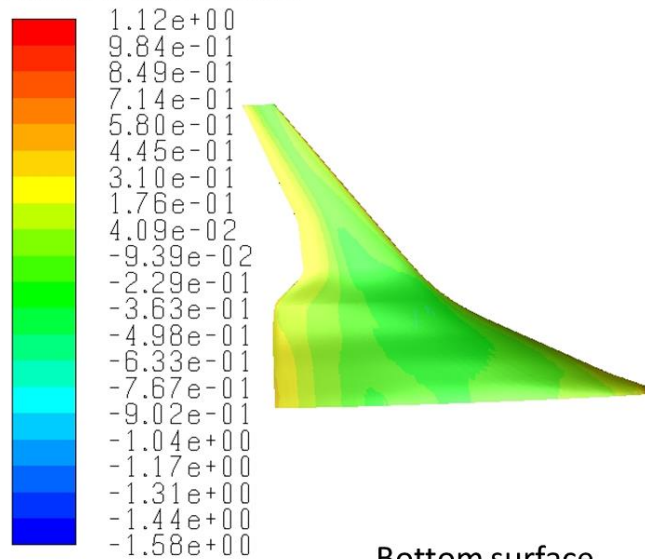
Figure 4.31 C_p distribution at $M_\infty=0.77$ and $\alpha=2^\circ$ on top and bottom surface of BW11.

Pressure Coefficient



Top surface

Pressure Coefficient



Bottom surface

Figure 4.32 C_p distribution at $M_\infty=0.8$ and $\alpha=2^\circ$ on top and bottom surface of BW11.

Several sections, located at different spanwise positions, have been identified in the pressure distribution contour of the upper surface to analyse the flow over the body and wing respectively, in conditions of $M_\infty=0.8$ and $\alpha=2^\circ$. The spanwise stations analysed are $\eta=0$ ($y=0$ m), $\eta=0.17$ ($y=6.5$ m), $\eta=0.34$ ($y=13$) m, $\eta=0.45$ ($y=17.5$ m), $\eta=0.80$ ($y=31$ m) and $\eta=1$ ($y=38.5$ m). First of all, it can be observed how the local lift in the section $\eta=0$, which is on the symmetry plane, is very low. Indeed, it derives from the area between the pressure coefficient of upper and lower surface, and the plot of pressure distribution, in figure 4.33, shows that values of C_p of upper surface and lower are very close.

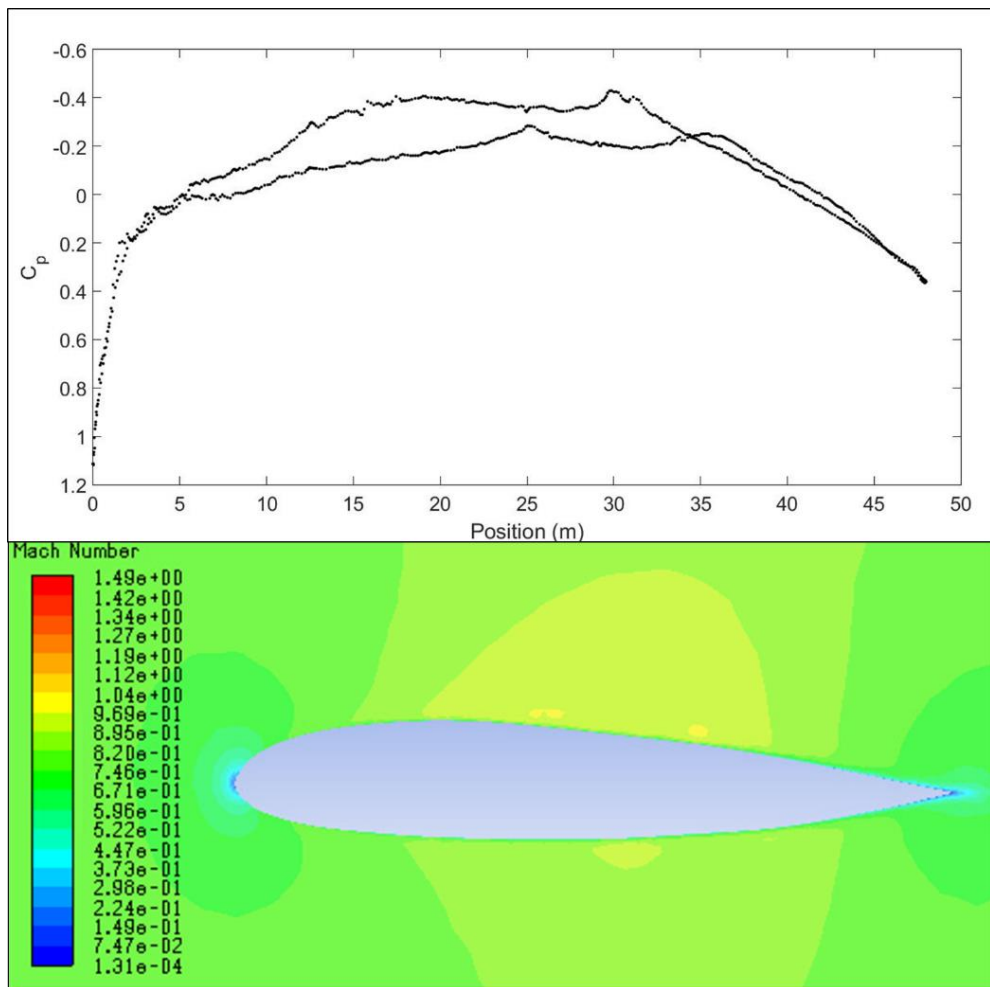


Figure 4.33 Section $\eta=0$, Mach and C_p distributions at $M_\infty=0.8$ and $\alpha=2^\circ$.

Furthermore, the stagnation point is clearly defined because this section coincides with the centreline of the body and there is no lateral flow. Moreover, from Mach contour it is possible to see that the shock wave, which starts at the wing tip, does not reach this section. In the section $\eta=0.17$ (shown in figure 4.34), there is no stagnation point because there is a spanwise flow component due to the sweep and the large change in thickness in the body, so C_p at the leading edge is reduced ($C_p = 0.13$). This means that 3D effects start to affect the lift and drag generated by this part of the body.

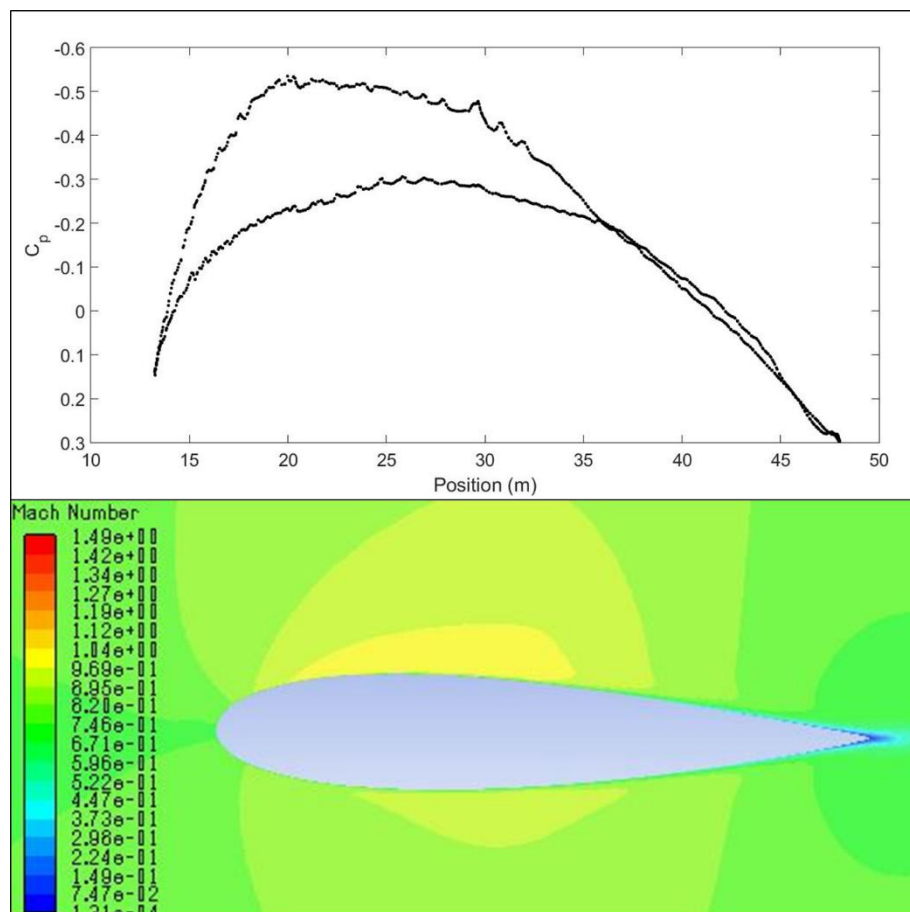


Figure 4.34 Section $\eta=0.17$, Mach and C_p distributions at $M_\infty=0.8$ and $\alpha=2^\circ$.

Section $\eta=0.34$ is the crank between body and wing. From the Mach number contours, in figure 4.35, it is possible to notice that the flow is supersonic over the most forward part of the section, but the shock is still weak.

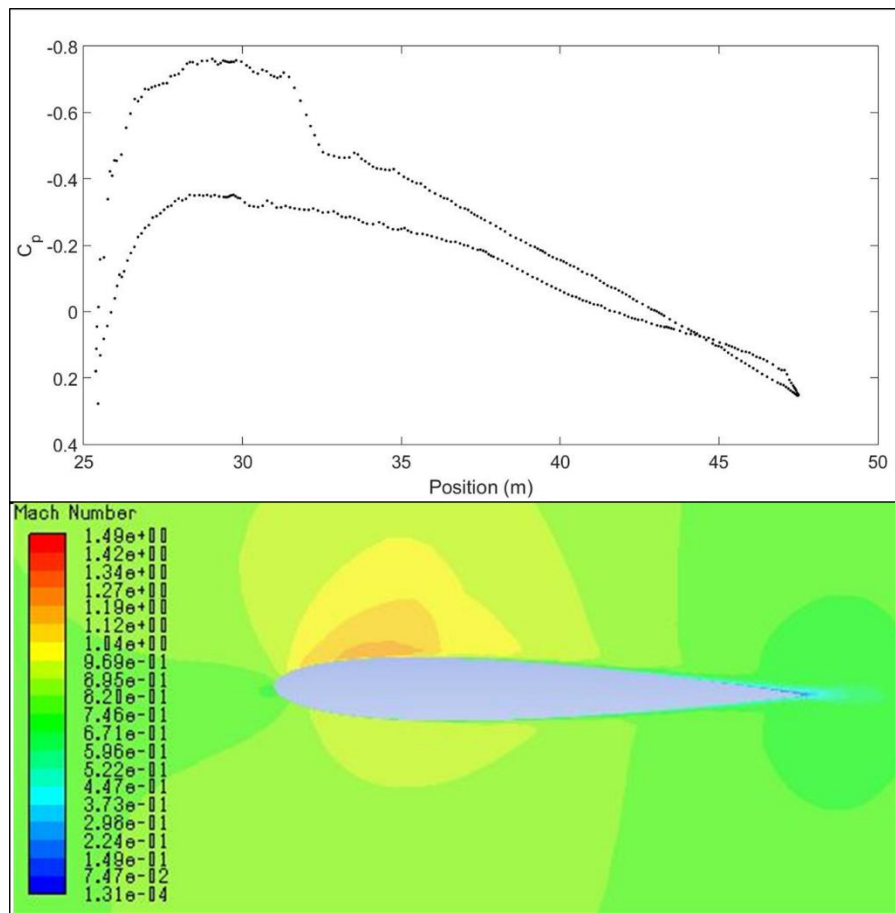


Figure 4.35 Section $\eta=0.34$, Mach and C_p distributions at $M_\infty=0.8$ and $\alpha=2^\circ$.

Moreover, in the C_p distributions there is a significant difference between top and bottom surface pressures near the leading edge that gives a large contribution to the lift. For the first wing section considered, at $\eta=0.45$, the pressure distribution shows that there is still the large difference in C_p values between top and bottom surfaces at the leading edge and the 3D effects have a smaller contribution on the wing because the value of C_p at leading edge is

higher. Local Mach number as shown, in figure 4.36, reaches a value close to 1.35 next to the leading edge, but thanks to the supercritical aerofoil design with reflex camber at the trailing edge, the lift generation is relatively high.

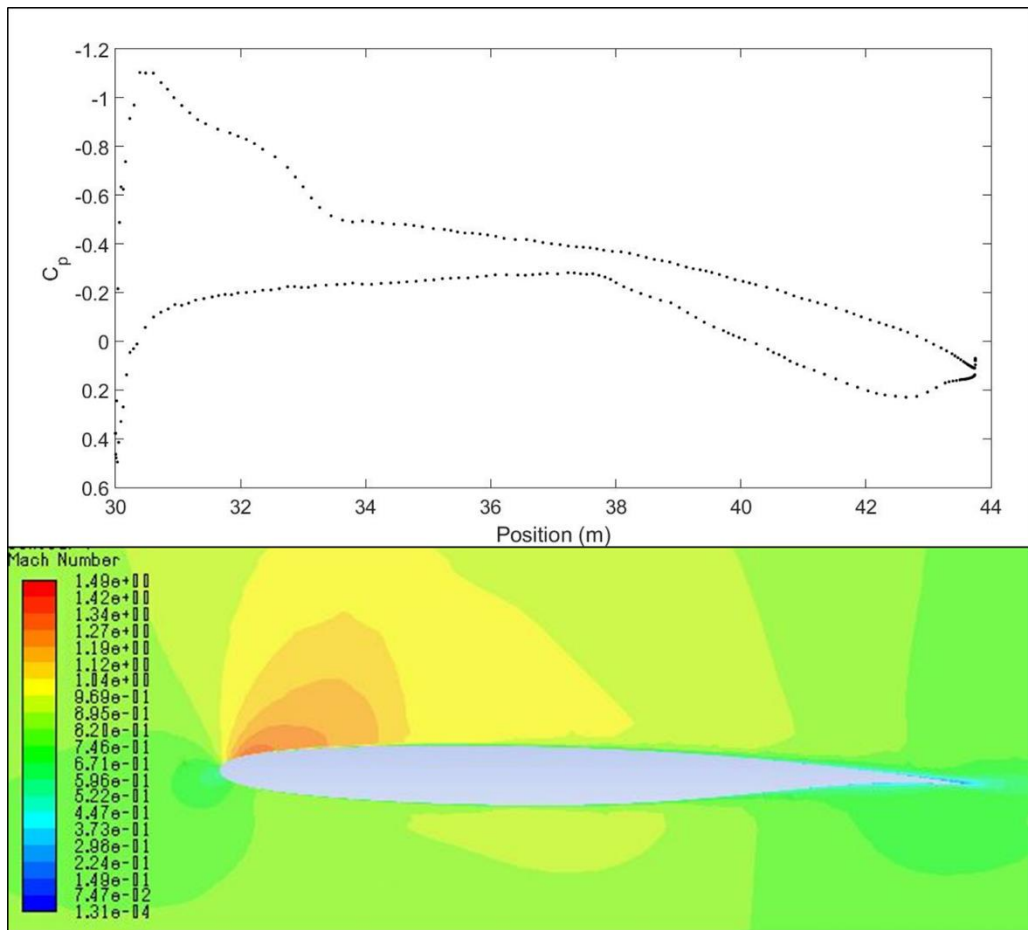


Figure 4.36 Section $\eta=0.45$, Mach and C_p distributions at $M_\infty=0.8$ and $\alpha=2^\circ$.

Moving to the section at $\eta=0.80$, local Mach number reaches a value close to 1.5 and the shockwave causes a great increase in C_p level on the profile (figure 4.37). The flow seems attached despite the strength of the shock wave.

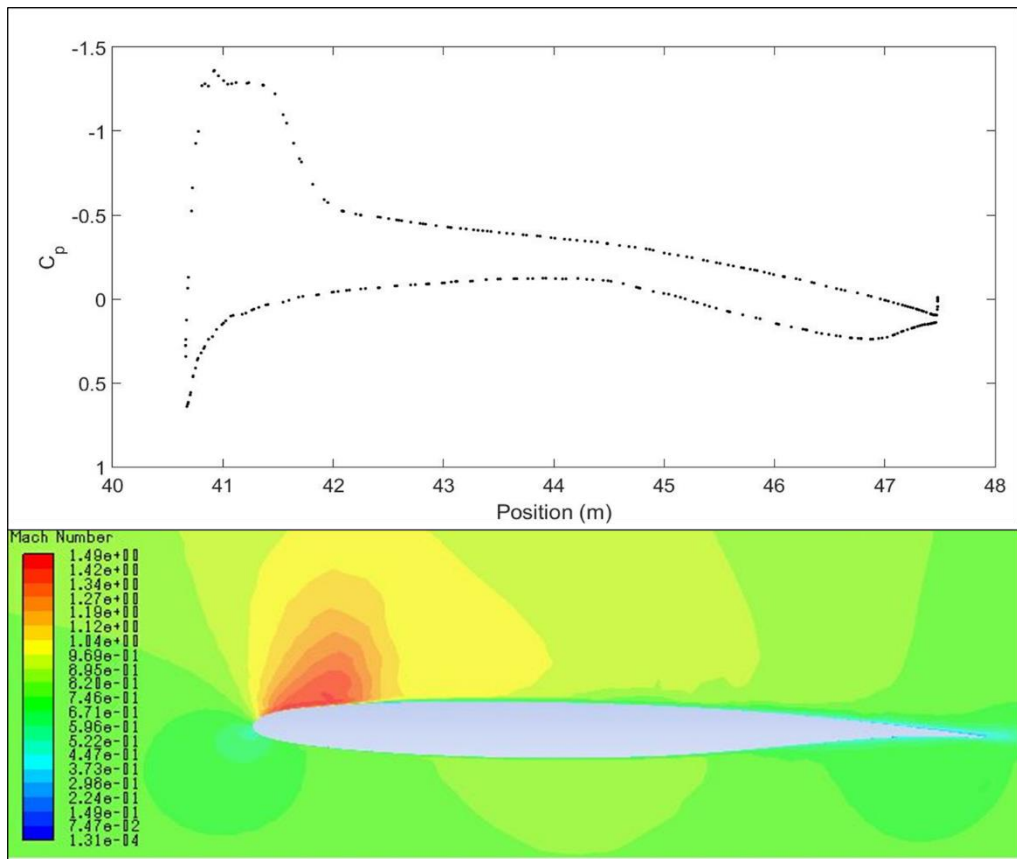


Figure 4.37 Section $\eta=0.80$, Mach and C_p distributions at $M_\infty=0.8$ and $\alpha=2^\circ$.

In the last section $\eta=1.00$, which is the tip of outer wing, the shock wave is very close to the leading edge (figure 4.38). This means that the flow is decelerated very early, making the values in pressure distribution between upper and lower surface very close. Therefore, the contribution to global lift of this section is very low.

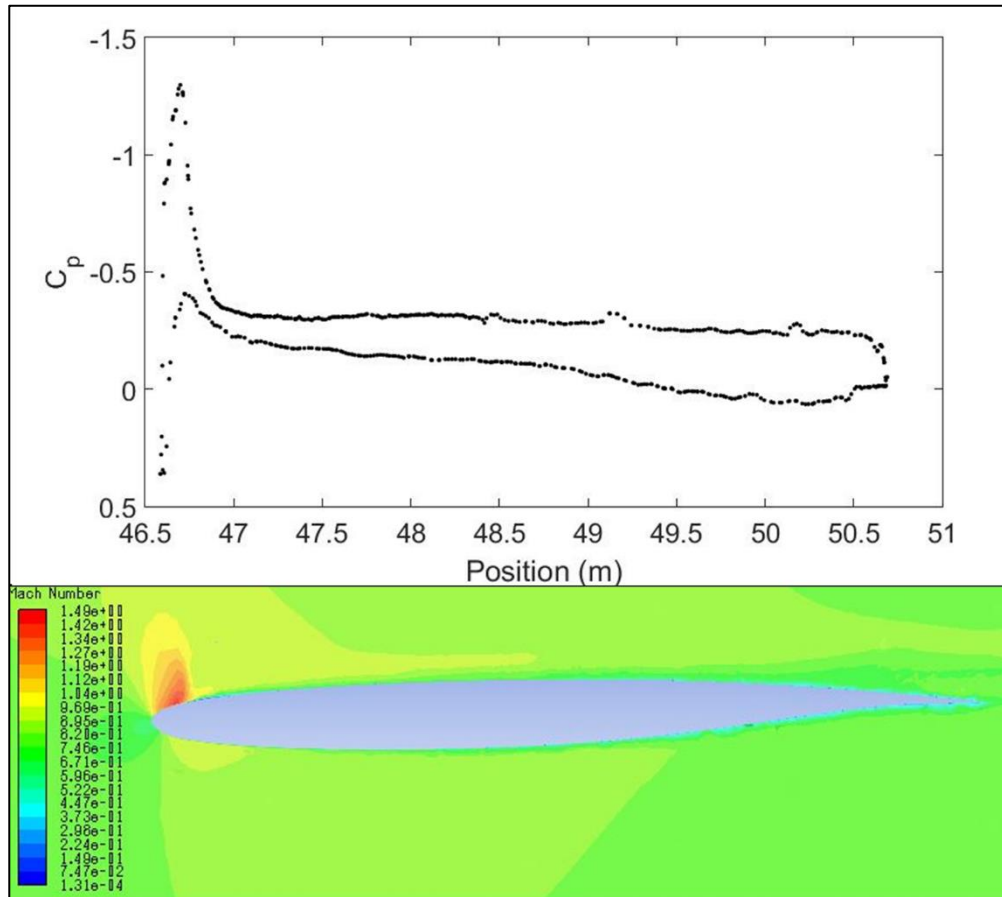


Figure 4.38 Section $\eta=1$, Mach and C_p distributions at $M_\infty=0.8$ and $\alpha=2^\circ$.

Comparison of these results with Mach and pressure distributions for $M_\infty = 0.7$ and $\alpha=2^\circ$ (figure 4.39) and for $M_\infty = 0.75$ and $\alpha=2^\circ$ (figure 4.40) in section $\eta=1$, where the shock wave is stronger than in the other positions, is shown. It possible to notice that the strength at $M_\infty = 0.7$ and $M_\infty = 0.75$ is lower, indeed local Mach reaches value not up 1.4 for $M_\infty = 0.7$ and not up 1.26 for $M_\infty = 0.75$.

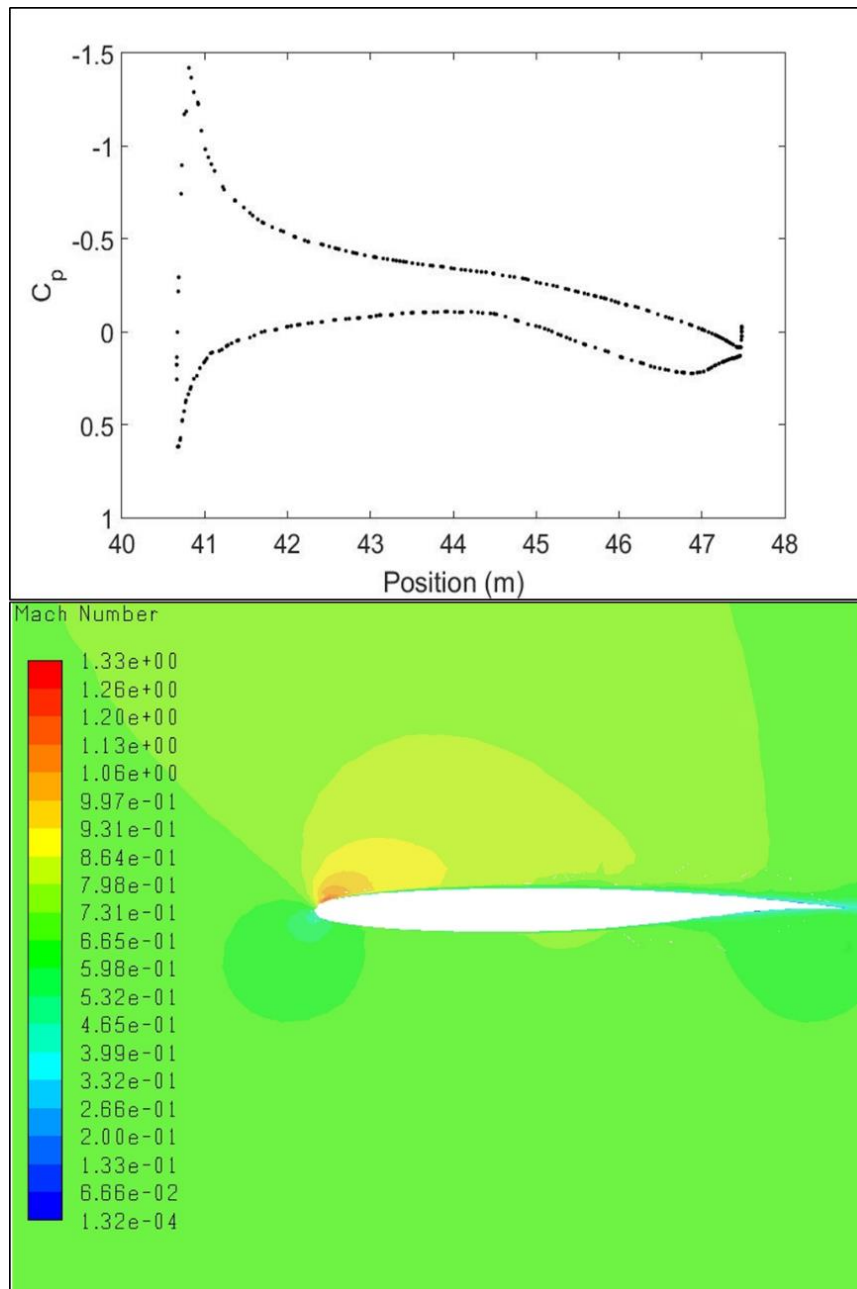


Figure 4.39 Section $\eta=0.80$, Mach and C_p distributions at $M_\infty=0.7$ and $\alpha=2^\circ$.

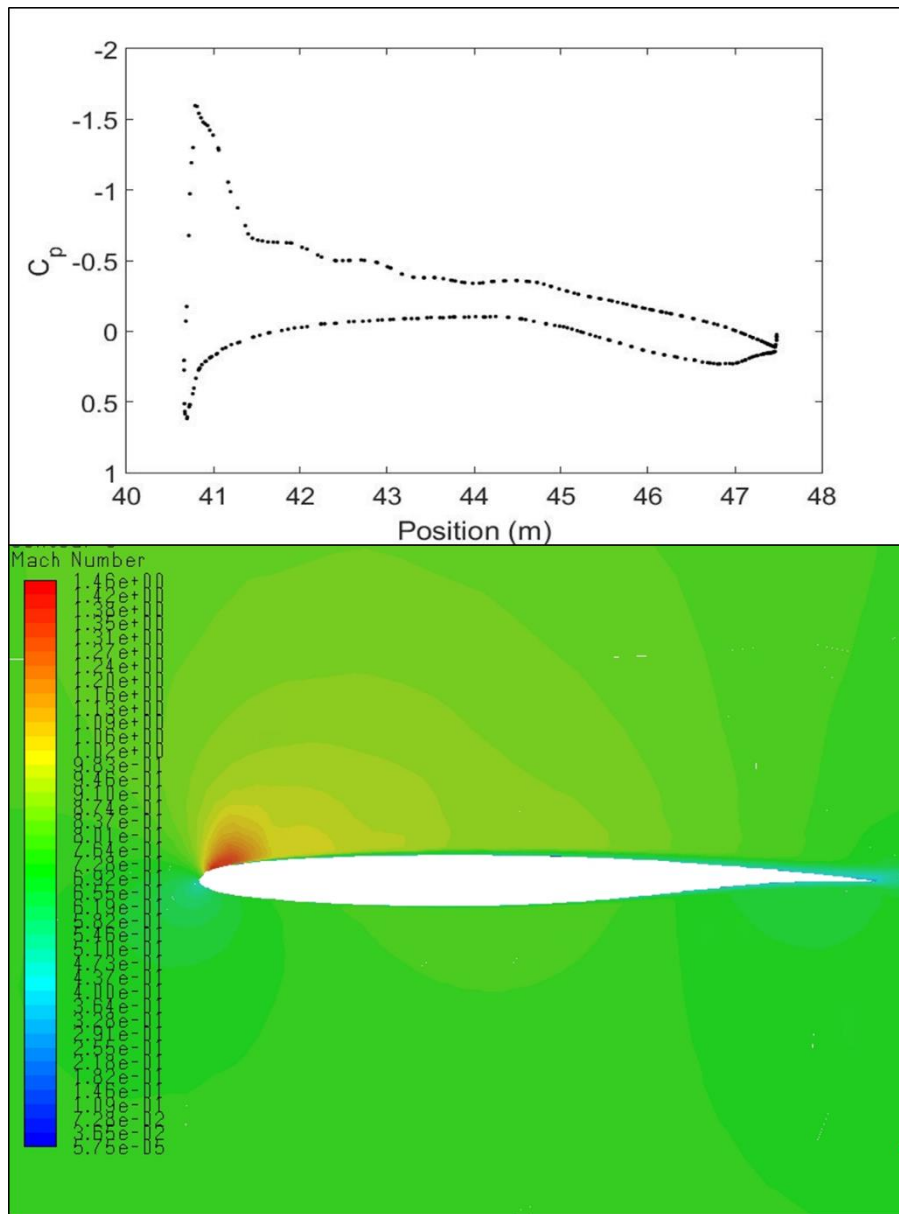


Figure 4.40 Section $\eta=0.80$, Mach and C_p distributions at $M_\infty=0.75$ and $\alpha=2^\circ$.

The presence of the shockwave has strong implications in the lift and drag created by the wing, it can induce separation of the flow behind it, generating a substantial increase in wave drag which implies reduction in the aerodynamic efficiency. Figure 4.41 shows a strong shockwave at $\alpha=3^\circ$ and for $M_\infty=0.8$, indeed after $\alpha=2^\circ$ the drag coefficient shows a sharp

rise for $\eta=0.80$ where a separation exists. This is visible in figure 4.38 where local Mach number reaches the value of 1.6 and a strong shock wave appears near the leading edge, flow after the shock does not remain attached but a bubble of separated flow forms. In the bubble separation the flow is deflected away from the surface due to the reverse flow as shown in figure 4.42.

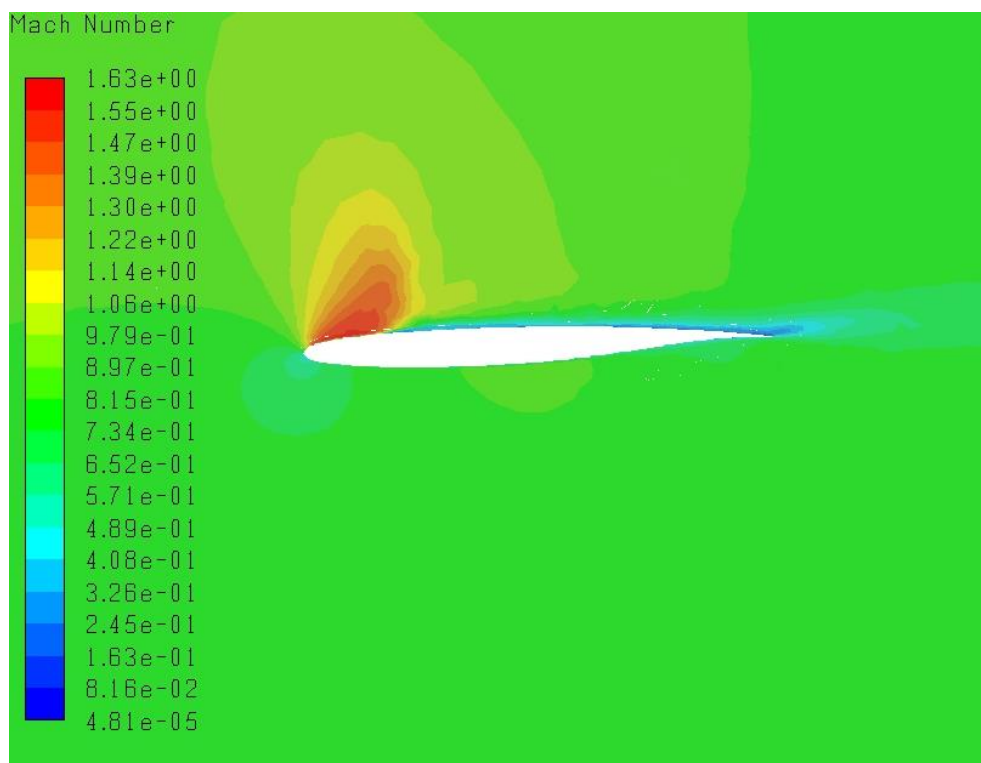


Figure 4.41 Section $\eta=0.80$, Mach distribution at $M_\infty=0.8$ and $\alpha=3^\circ$.

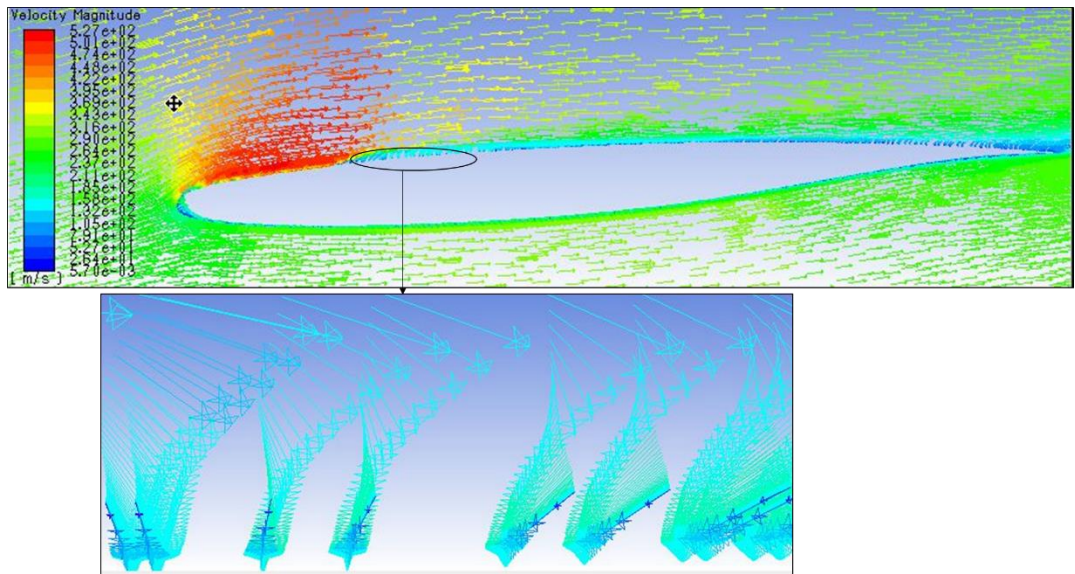


Figure 4.42 Section $\eta=0.80$, bubble separation at $M_\infty=0.8$ and $\alpha=3^\circ$.

The evidence for bubble separation is seen in the C_p distribution, because after the shock position there is a constant pressure region in the upper surface. The length of the separation bubble is quite small and after that the flow is reattached and the pressure continues to increase.

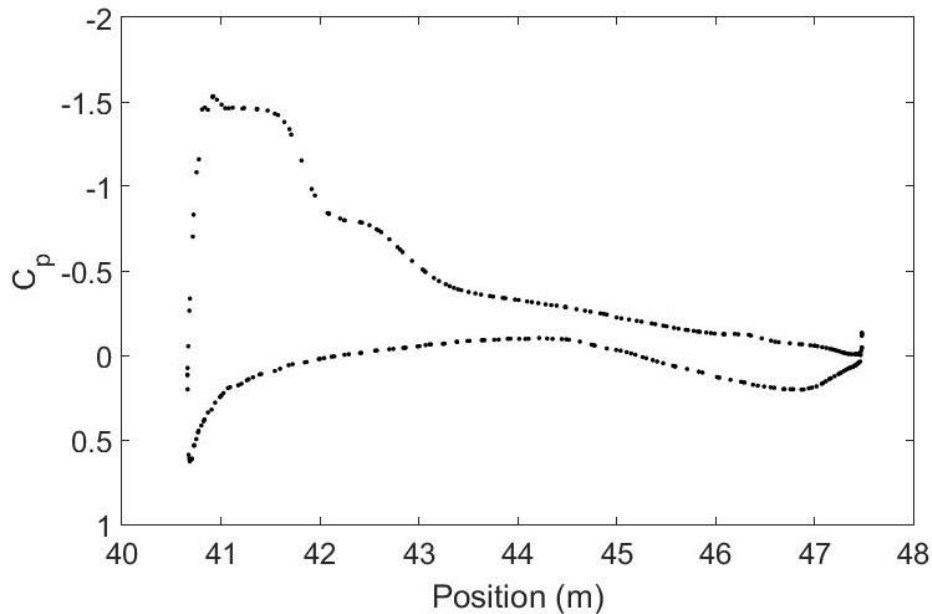


Figure 4.43 Section $\eta=0.80$, C_p distribution at $M_\infty=0.8$ and $\alpha=3^\circ$.

4.2.4 BW11 Aerodynamic Optimization on conceptual design

This chapter is focused on some proposals for aerodynamic optimization of the baseline configuration to offer performance advantages over conventional transonic transport configurations. To find the best configuration, while maintaining enough volume for passengers, some modifications in the geometry should be done slightly improving the aerodynamic efficiency at each step. The target of BW11 optimization is to achieve better aerodynamic efficiency at transonic speed and bring Mach drag divergence number closer to 1.

- Sweep: An optimization could be done by increasing the sweep angle to reduce the strength of the shock wave on the wing while decreasing the sweep angle of the body, so it could generate more lift.
- Transition of the body and outer wing: Making the transition of the body and outer wing smoother, while not compromising the inner space for passengers, could limit the 3D effects. An idea to achieve that, maintaining enough inner space, could be to enlarge the centre-body area to have smoother change in sections. In this way lift increases but friction drag increase will as well. Since friction drag is the major contributor to total drag, this would need to be carefully managed.
- Aerofoils: A good way to ensure a delay in Mach drag divergence and to have weak shock wave is modifying the aerofoils. First, shape variation of the wing section should be small, otherwise a large shape variation may lead to a bad change in aerodynamic characteristics at transonic speed. Moreover, making the thickness to chord ratio smaller, while also satisfying the structural requirements, Mach drag divergence number increases and it could be possible to estimate the relation between t/c and M_{DD} with some empirical or statistical equations [26]. Thickness chord ratio becomes smaller by increasing chord length, and consequently decreasing the pressure drag could offset the increase of friction drag.

- Twist: An improvement of aerodynamic characteristics could be reached by twisting the wing along the Y axis. Aerofoil sections in the tip region have an angle of attack lower than that at the root, and chord lines of aerofoils at different spanwise stations are not parallel to each other. The twist can decrease loading and weaken shock strength at the outer wing. Typical twist angles are 1° and 2° and they rarely exceed 3° . Another benefit of the twist is the delay in stall because it adjusts lift distribution along the wing. This means that the linear part of the lift curve, which for $M=0.7$ and coarse mesh shown in figure 4.22, could be extended for $\alpha > 4^\circ$.

4.2.5 Critical comments about advantages and disadvantages mentioned

This section presents some considerations, consequently the study of BW11, about the advantages and disadvantages mentioned in chapter 2. First of all, lift is also generated by centre-body, but for the BW11 its contribute is not so high as expected, the most contribution at the lift is generated by the section of the kink and the leading edge of the outer wing. The comparison of the blended wing body with Sears Hack's body, mentioned by Kunawala, is not appropriate because of the large shape of the centre-body that is necessary to provide enough inner space for passengers. Reduction of the large shape of the centre body is a challenge because it would make the transition between thicker centre-body aerofoil to thinner outer wing aerofoil abrupt, causing bad aerodynamic characteristics at transonic speed. The analysis of BW11 is carried out without engines, but the aft location of them maybe could bring some benefits in wake drag. A drawback is that the gravity centre is moved aft, so the configuration needs to load the forepart to reduce the pitching moment. Moreover, supersonic flow does not occur on the lower surface and so in all sections there are not shock waves on the bottom curve.

5 CONCLUSIONS

The project was mainly focused on analysing the aerodynamic performance in transonic flow of the BW11 blended wing configuration, which was originally designed for subsonic flight. CFD analysis through ANSYS ICEM and Fluent has resulted in aerodynamic data for the study the preliminary validation of the aerodynamic design. Its transonic aerodynamic performance has been investigated based on RANS simulation with Kw-SST turbulence model. The aerodynamic performance investigation included variation of lift and drag coefficients. In addition, coefficient of pressure and Mach distributions are studied to provide deeper physical insight. The first stage of the study was the validation of the results obtained by Fluent on the aerofoil RAE2822 in transonic conditions. It is known that CFD results, obtained with CFD software, are affected by mesh characteristics and mesh size. It is obvious that higher the number of cells is, the better the calculations converge to the physically accurate solution. However, the 2D aerofoil case has been analysed with two meshes characterized by different number of cells and it has been shown that values of lift and drag coefficient and the surface pressure distributions oscillated within acceptable limits. Moreover, unstructured and structured meshes provided comparable results. The studies on RAE2822 also helped in selecting which turbulence model had to be used. Finally, the mesh size for the Blended wing body mesh generation was a trade-off of low computational time cost and acceptable accuracy in results. The turbulence model was chosen according to the value of y^+ which could be reached with the mesh size of prism layers imposed. From the decision of the mesh and solver characteristics, the baseline results were obtained for different Mach numbers and angles of attack. The Korn factor has been computed to estimate aerodynamic efficiency of the BW11 in transonic flight. Given that it was not possible to calculate exactly Mach drag divergence due to the limited analysis at three Mach numbers, its value had an uncertainty, which, taking this into account, was estimated at between 0.89 and 0.94. Comparison with the Korn

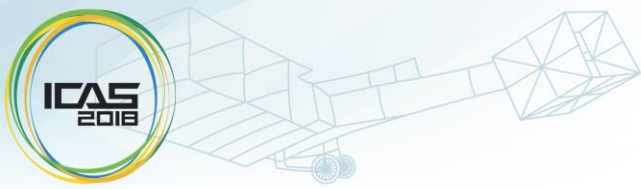
factor of a conventional aircraft design, which is about 0.96, highlights that BW11 may be a reasonably good design, considering $M_{DD}=0.77$ and cruise condition of $M_\infty=0.75$ and $\alpha=2^\circ$. One of the main aspects to notice is the maximum L/D reached values close to 20 for α between 2° and 3° , which are higher than conventional aircraft despite the presence of shock waves over the wing. However, the shock wave and separation limit high efficiency at higher angles of attack. Indeed, the rise of drag starts already for $\alpha=1.5^\circ$ and separation for $M_\infty=0.8$ happens at $\alpha=3^\circ$. Therefore, surface pressure and Mach number distributions are investigated for $\alpha=2^\circ$. Shock waves starts at the wing tip and reach the crank of the wing. In terms of lift, the body gives a lower contribution than the outer wing because the C_p levels on the upper and lower surfaces are very close. Most of the lift is generated at the leading part of the upper surface of the wing, and interactions between boundary layer and shock wave is evident in the compression in the C_p distribution indicating the position of the shock wave. Another interesting parameter investigated has been the static margin and its variation with Mach number. This remains a positive value with increasing Mach number, but decreases due to the increase in strength of shock wave. In conclusion, BW11 performance are reasonably good but an optimization procedure, proposed in previous chapter by the author, should be done to reach aerodynamic performance in transonic field comparable with conventional aircraft.

6 REFERENCES

- [1] Nimeesha B. Kuntawala, “Aerodynamic Shape Optimization of a Blended Wing Body Aircraft Configuration”. Aerospace Engineering University of Toronto, 2011.
- [2] https://www.militaryfactory.com/imageviewer/ac/pic-detail.asp?aircraft_id=239&sCurrentPic=pic2.
- [3] Rupesh A., Anchith A.K., “Trends in Wing Design and Role of Blended Wing Body (BWB) in the Performance Characteristics of Aircraft”. Journal of Advanced Engineering Research ISSN: 2393-8447 Volume 3, Issue 1, pp.8-14, 2016.
- [4] Kroo, I., “Innovations in Aeronautics,” 42nd AIAA Aerospace Sciences Meeting, January 2004.
- [5] Qin, N., Vavalle, A., Le Moigne, A., Laban, M., Hackett, K., and Weinerfelt, P., “Aerodynamic Considerations of Blended Wing Body Aircraft”. Progress in Aerospace Sciences, Vol. 40, No. 6, 8 2004, pp. 321–343.
- [6] Liebeck R. H., “Design of the Blended Wing Body Subsonic Transport”, Journal of Aircraft, 41(1), January-February 2004.
- [7] Ikeda T., Cees B., “Aerodynamic performance of a blended Wing-Body configuration aircraft”. 25th international congress of aeronautical sciences.
- [8] Dehpana P., Nejat A., “The aerodynamic design evaluation of a blended-wing-body-configuration”. Aerospace Science and Technology, Volume 43, Pages 96-110, June 2015.

- [9] Patel D., Carter M. B., Vicroy D. D., “Blended-Wing-Body Transonic Aerodynamics: Summary of Ground Tests and Sample Results (Invited)”. 47th AIAA Aerospace Sciences Meeting, January 2009.
- [10] Ikeda T., “Aerodynamic Analysis of a Blended-Wing-Body Aircraft Configuration”. RMIT University, March 2006.
- [11] Liebeck R. H., “Blended wing body design challenges”, International Air and Space Symposium and Exposition: The Next 100 Y, Dayton, Ohio, 14-17 July 2003.
- [12] Vos R., Farokhi S., “Introduction to Transonic Aerodynamics”.
- [13] Hurt H. H. Jr., “Aerodynamics for Naval Aviators”. Book, published by Direction of the Commander, Naval Air Systems Command, United States Navy, reprinted by Aviation Supplies and Academics, Inc., 7005 132nd Place SE, Renton, Washington 98059-3153, 1965.
- [14] Prof. Coiro D. P. (Personal Communication).
- [15] Weiland P., “Transonic Aerodynamics in conceptual aircraft design”. Deutscher Luft-und Raumfahrtkongress, 2013.
- [16] Mason W.H., “Transonic Aerodynamics of Airfoils and Wings”.
- [17] AGARD. “Special Course on Engineering Methods in Aerodynamic Analysis and Design of Aircraft”. AGARD Report 783, JAN1992.
- [18] Ansys Fluent 12.0 Theory Guide. ANSYS, April 2009.

- [19] Anderson J. D., JR, "Computational Fluid Dynamics: The basics with Applications". University of Maryland, McGraw-Hill, inc.
- [20] Barnola R. L., "Interaction Between Aerodynamics. Structure and Packaging in a Blended Wing Body Configuration Conceptual Design". MSc. Aerospace Vehicle Design, School of Engineering, Cranfield University, 2012.
- [21] Kim Y. H, Ko S. L., "Improvement of cutting simulation using the octree method". Int J Adv Manuf Technol, 2006.
- [22] Bottasso C. L. and Detomi D., "A Procedure for Tetrahedral Boundary Layer Mesh Generation". Dipartimento di Ingegneria Aerospaziale, Politecnico di Milano, Milano, Italy, 2002.
- [23] Lawson S. G, Greenwell D., Quinn M. K., "Characterisation of Buffet on a Civil Aircraft Wing", AIAA Paper 2016-1309, AIAA 54th Aerospace Sciences Meeting, San Diego, California, USA, 4-8 January 2016.
- [24] Lyu Z., Martins J. R. R. A., "RANS-based Aerodynamic Shape Optimization of a Blended-Wing-Body Aircraft". Fluid Dynamics and Co-located Conferences, 21st AIAA Computational Fluid Dynamics Conference, San Diego, CA, June 24-27, 2013.
- [25] "Flying Qualities Phase", Volume II, Chapter 5: Longitudinal Static Stability, October 1990.
- [26] Scholz D., Ciornei S., "Mach number, relative thickness. Swept and lift coefficient of the wing-an empirical investigation of parameters and equations". Hamburg University of Applied Sciences, Germany.



A RAPID AERODYNAMIC PREDICTION METHOD FOR UNCONVENTIONAL TRANSONIC AIRCRAFT CONFIGURATIONS

Simon Prince*, Davide Di Pasquale*, Kevin Garry* & Cristina Nuzzo**
*Cranfield University, UK, **Politecnico di Torino, Italy

Keywords: *Transonic Aerodynamics, Aircraft Design, CFD*

Abstract

This paper presents some results comparing the use of the Full Potential equations, coupled with the turbulent integral boundary layer equations for aircraft transonic cruise analysis. Use of such a method in the conceptual design stage is shown to be capable of yielding accurate enough data in a few minutes on a single processor, where Navier-Stokes simulations on 100+ processors take several days.

1 Introduction

Modern conceptual aircraft design requires the rapid generation of appropriate aerodynamics data for performance calculation and structural analysis within the context of trade-off studies. Such data must be of sufficient accuracy, in terms of overall and local lift and drag forces, that the performance trends are correctly captured and such attributes as range and fuel burn characteristics are predicted accurately.

The need for this data to be available rapidly to allow for many concepts and configurations to be assessed in these trade-off studies allows the costs of the conceptual design stage to be minimized. The accuracy of the analysis methods allows uncertainties associated with the decision making and the resulting conceptual configurations to be minimized, thereby reducing the downstream costs associated with design mistakes.

The focus of this paper is the demonstration of a rapid but lower fidelity method for the conceptual design and analysis of transonic cruise transport aircraft. Since the application of interest is the design analysis of transonic cruise

wing flows, the Viscous Full Potential method, which couples the solution of the Full Potential equations for compressible rotational inviscid flow with the integral boundary layer equations, is wholly adequate for a design method. No aircraft wing would be designed to operate in cruise flight under significant separated flow condition, which would result in buffet phenomena, and so a rapid and relatively accurate “attached flow” method for such applications is valid.

2 The Viscous Full Potential Method

2.1 The Governing Equations

Potential flow methods involve the solution of the governing equations which are reduced by assuming the flow is inviscid, irrotational and isentropic. These simplifications allow the continuity equation to be derived in terms of the velocity potential function Φ . The last two assumptions, however, limit the validity of the method to cases where no shock waves exist in the flow field, or where the shock waves are so weak that the isentropic assumption leads to only minor errors in the calculation of pressure and velocity. Supersonic flows can be computed only in the regions inside a shock layer. An example would be the supersonic flow around a slender body, where a potential flow solution could be computed between the attached bow shock wave and the body surface, assuming the conditions on the downstream side of the shock surface can be determined as a boundary condition for the calculation. The full velocity potential equation, for an irrotational, inviscid, isentropic flow, in terms of Cartesian coordinates (x,y,z) is written:

$$\begin{aligned}
 & \left(1 - \frac{\bar{\Phi}_x^2}{a^2}\right) \bar{\Phi}_{xx} + \left(1 - \frac{\bar{\Phi}_y^2}{a^2}\right) \bar{\Phi}_{yy} + \left(1 - \frac{\bar{\Phi}_z^2}{a^2}\right) \bar{\Phi}_{zz} \\
 & - 2 \frac{\bar{\Phi}_x \bar{\Phi}_y}{a^2} \bar{\Phi}_{xy} - 2 \frac{\bar{\Phi}_x \bar{\Phi}_z}{a^2} \bar{\Phi}_{xz} - 2 \frac{\bar{\Phi}_y \bar{\Phi}_z}{a^2} \bar{\Phi}_{yz} \\
 & - 2 \bar{\Phi}_x \bar{\Phi}_{xt} - 2 \bar{\Phi}_y \bar{\Phi}_{yt} - 2 \bar{\Phi}_z \bar{\Phi}_{zt} - \bar{\Phi}_{tt} = 0 \quad (1)
 \end{aligned}$$

where the velocity potential Φ is defined by:

$$V = \sqrt{u^2 + v^2 + w^2} = \nabla \bar{\Phi} \quad (2)$$

such that:

$$u = \bar{\Phi}_x = \frac{\partial \bar{\Phi}}{\partial x}, \quad v = \bar{\Phi}_y = \frac{\partial \bar{\Phi}}{\partial y}, \quad w = \bar{\Phi}_z = \frac{\partial \bar{\Phi}}{\partial z} \quad (3)$$

and the time, t , is in the unsteady terms. If the flow is steady, the last four terms of the equation are neglected.

2.2 The VFP solver implementation

For this application, a steady flow VFP solver has been used, which is a development of the VFP code available commercially from IHS ESDU [1]. This code allows the wing geometry to be input as a series of section profiles to be defined from the root to the tip, along with the corresponding location, relative to the fuselage reference point, of the local leading edge, chord length and the local twist angle setting. The process of changing such geometric features as leading edge sweep, taper, local dihedral, crank location and twist setting therefore involves the change of a few parameters, which can be done manually or as part of a computational optimization algorithm.

The VFP program also incorporates the modelling of the zero alpha flow around the isolated fuselage whereby the potential flow field is obtained by the classical solution of the Stokes-streamline problem for the input body geometry defined in a separate input file [2]. This provides both the zero incidence surface pressure distribution on the isolated fuselage, and the increment in Mach number at the wing quarter

chord location across the wing span which is used to vary the local Mach number along the wing span in the VFP calculation. Validations of this method are reported in reference [3]. In order to calculate the aerodynamic characteristics of a complete wing-body configuration, the contribution to the forces and moments from the fuselage is calculated by computing the surface pressure distribution at the required angle of attack by the method of De Jarnette [4]. The surface integration of this distribution provides the local distribution of the lift and drag pressure force along its longitudinal axis (x in this case) which is further integrated to provide the total lift, drag and pitching moment contribution from the fuselage. The interference from the wing flow onto the body is not yet accounted for in the method, but this is deemed to be relatively minor for the long fuselage configurations typical of modern transport aircraft.

The VFP code automatically generates the separate computational grids around both the fuselage and the wing, details for which are provided in ref [1]. For this study, the wing-bodies investigated, are modelled with meshes of 135,432 cells, wrapping an O-topology grid around the wing (in this case 162 cells wrapped around the wing, 38 cells along the span of the wing and 22 cells outward from the wing surface). The fuselage was modelled with 33 points along its axis, and 32 points around its circular half perimeter, where the flow is assumed to be symmetric about the $y = 0$ (wing centreline) plane.

The code then solves the full (non-linear) potential flow equations, coupled with the integral boundary layer equations. In particular the code uses a relaxation algorithm to solve the finite difference form of the full velocity-potential equation which is coupled with the semi-inverse, swept / tapered integral boundary layer method of Ashill and Smith [5, 6]. The convergence criteria was set as a maximum absolute change in value of velocity perturbation potential reduced to an order of 10^{-6} .

2.3 The Navier-Stokes solver

For comparison with the VFP results, a modern commercial, compressible flow, Navier-Stokes

solver was employed to obtain high resolution simulations of the flows analyzed with the VFP method. The solver employed the Roe approximate Riemann solver for shock capturing with a second order scheme in both space and time to obtain converged steady flow solutions. A number of turbulence models were used for the Reynolds Averaged Navier-Stokes (RANS) calculations for comparative purposes, as detailed in the paper, and for test case 2 the Delayed Detached Eddy Simulation (DDES) method was used to obtain unsteady time accurate data. Grid insensitivity was demonstrated in all cases, the convergence criteria being overall force coefficient convergence together with residual convergence to at least 10^{-4} .

3 The Test Cases

3.1 Test Case 1: The W4 Wing-Body Configuration

The first validation test case was the RAE Wing 4, transonic wing-body configuration as shown in fig 1, which was tested in the RAE Bedford 8ft Supersonic wind tunnel in the late 1970's.

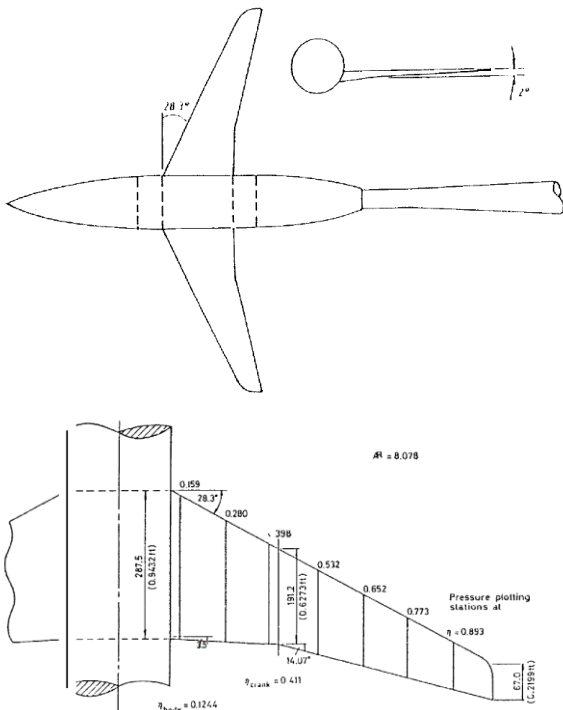


Fig 1: Dimensions of the V4 wing-body configuration [7].

The data was made available via the NATO AGARD AR-303 report in 1994 [7]. In this paper, comparisons are presented for the Mach 0.78, $Re_c = 5.12 \times 10^6$ condition

3.2 Test Case 2: The RBC12 Wing-Body Configuration

The configuration chosen for the second validation test case was the RBC12 wing/body geometry designed by the Aircraft Research Association (ARA). Fig 2 presents a photograph of the half model being tested in the ARA Transonic Wind Tunnel along with some basic dimensions [8]. The RBC12 model has a quarter chord sweep of 25° , with a swept / tapered and cranked planform which has a semi-span of 1.085m, a mean aerodynamic chord of 0.279m, and an aspect ratio of 7.78.

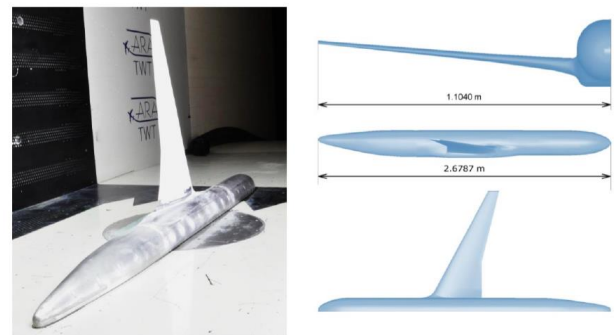


Fig 2: The RBC12 wing-body configuration half model in the ARA Transonic Wind Tunnel, and its principle dimensions [8].

The half span model was mounted on the floor of the tunnel, from a 5-component strain gauge balance which measured the forces and moments on the combined wing and fuselage. Surface pressures were obtained using the Dynamic Pressure Sensitive Paint (DPSP) method. Tests were conducted in the Mach number range 0.7 – 0.84, corresponding to Reynolds numbers, based on mean aerodynamic chord, of 2.8 to 3.9 million. In this paper on the comparisons for the Mach 0.8, $Re_c = 3.75 \times 10^6$ condition are presented.

3.3 Test Case 3: The BW-11 Blended Wing-Body Configuration

The VFP method having been validated against experimental data with test cases 1 and 2, the third demonstration was to assess the ability of the VFP approach to accurately and rapidly predict the aerodynamic characteristics of a transonic blended wing body configuration. For this the Cranfield University BW-11 configuration was adopted, the basic dimensions for which are presented in Fig 3.

Because experimental data for such configurations at transonic flight conditions, at the time of writing, were not available to the authors, it was decided to make a direct comparison between VFP and high resolution Reynolds Averaged Navier-Stokes results, given that this approach has been shown to be accurate enough for conceptual design analysis for this application, as will be demonstrated for the first two test cases.

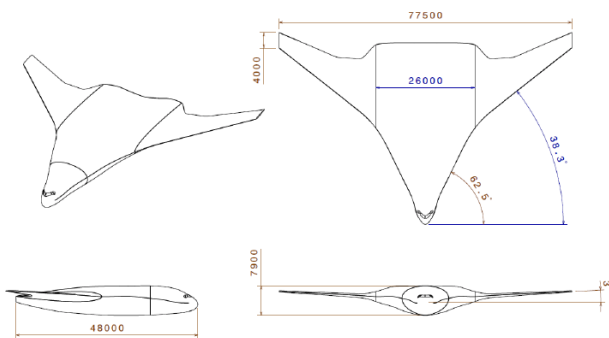


Fig 3: Dimensions of the basic Cranfield BW-11 Blended Wing Body configuration with no winglets (units in mm).

4 Results and Discussion

4.1 Test Case 1: The W4 Wing-Body Configuration

For this test case the VFP results are compared only with the experimental data for the Mach 0.78 case of interest. No RANS calculations were performed for this case. Fig 4 compares the VFP predicted lift (C_L) and drag (C_D) coefficient characteristics with those obtained from the experiment. Here the dashed line in the lift curve

indicates the linear trend in VFP predicted lift and shows that this lower order method has successfully captured the non-linearity at the higher α associated with onset trailing edge separations which the coupled boundary layer method can capture. While the VFP method is seen to resolve the drag levels at low α remarkably well, it over-predicts C_D by up to 10 drag counts at the higher incidences. For a lower fidelity method, however, this is still acceptable as it is often the trends which need to be resolved and not necessarily accurate magnitudes.

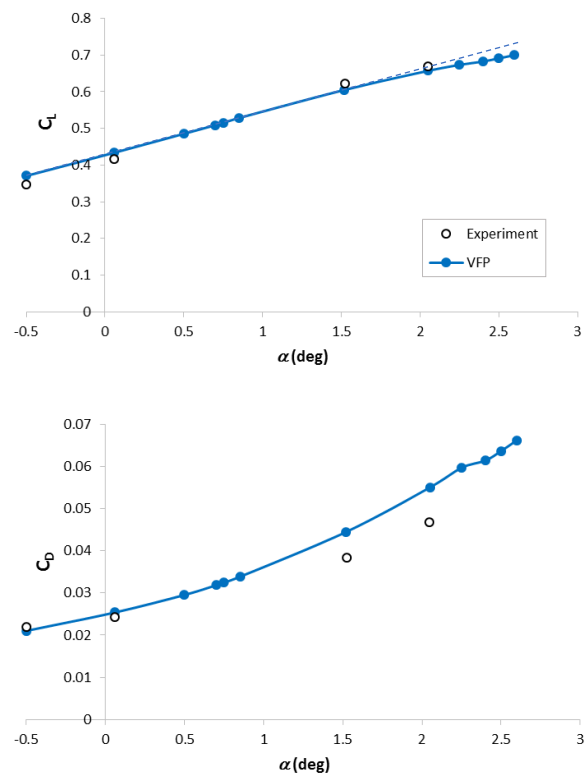


Fig 4: Comparison of measured and computed lift and drag characteristics with α , for W4. $M_\infty=0.78$, $Re_c=5.12 \times 10^6$.

The VFP method outputs automatically, a breakdown of the local lift and drag contributions along the wing span for the assessment of wing loading. Fig 5 presents the comparison between the VFP predicted wing loadings and those obtained from integration of the experimentally measure surface pressures. Here, again, the VFP method is seen to capture these remarkably well for all four α cases investigated, certainly to an accuracy useful at the conceptual design stage.

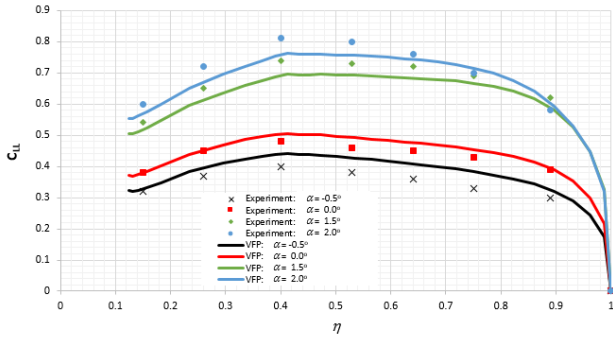


Fig 5: Comparison of the variation with angle of attack of measured (via integrated surface pressure) and VFP predicted spanwise loading (local lift coefficient). $M_\infty=0.78$, $Re_c=5.12 \times 10^6$.

A selection of the comparisons of the predicted and experimentally measured chordwise surface pressure distributions are presented at different spanwise stations in figure 6 and 7, for $\alpha = 0$ and 2.0° respectively. Here, η is the span location as a percentage of the total wing span, and C_p is the local surface pressure coefficient. For the zero incidence case, shown in fig 6, the surface pressure distributions are captured with an accuracy typically expected with a Navier-Stokes calculation, including the resolution of the weak upper surface shock wave, towards the wing tip around 30% chord. The discrepancy with the two experimental points for the most inboard spanwise location is due to a known experimental measurement error.

For the more challenging case of $\alpha = 2.0^\circ$, where a relatively strong upper surface shock wave appears, the comparisons are plotted in fig 7. Here, again, the VFP method provides predicted surface pressure distributions, with indicative shock wave locations and strengths that are typical of the accuracy expected of modern Navier-Stokes solvers using much finer computational meshes and at much higher computational and run-time cost. The plot for the most outboard spanwise station is of interest, as this shows that the VFP method has successfully captured the trend towards boundary layer separation at the tip, indicated when local C_p at the trailing edge goes negative.

The VFP method has been developed to output both the local boundary layer properties on the wing surface, including the displacement thickness, δ^* , the momentum thickness, θ , the

shape factor, $\bar{H} (= \delta^*/\theta)$, together with local skin friction coefficient, C_f , and the skew angle, β , between the limiting flow vector above the surface, and that at the boundary layer edge, which is useful for the design of flow control devices.

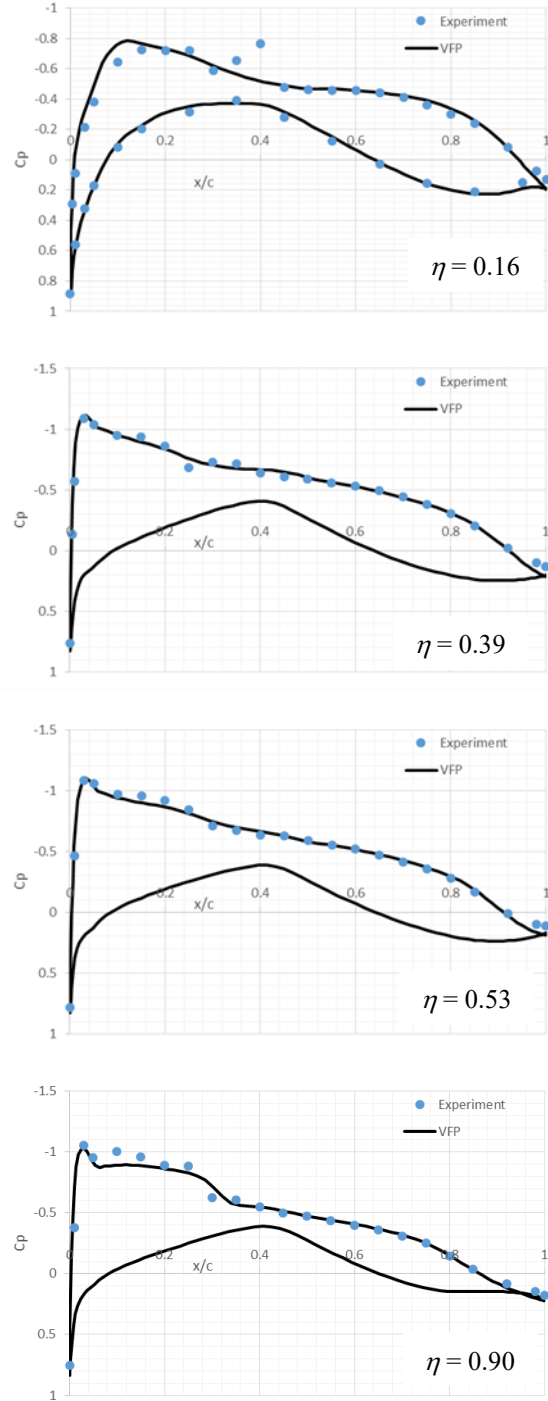


Fig 6: Comparison of measured and computed surface pressure distributions for W4. $M_\infty=0.78$, $\alpha = 0.0^\circ$, $Re_c=5.12 \times 10^6$.

These parameters are output directly from the boundary layer solver, whereas separate post-processing is required from a CFD solver. Fig 8 presents the VFP derived upper surface C_p contours showing the resolution for two α cases.

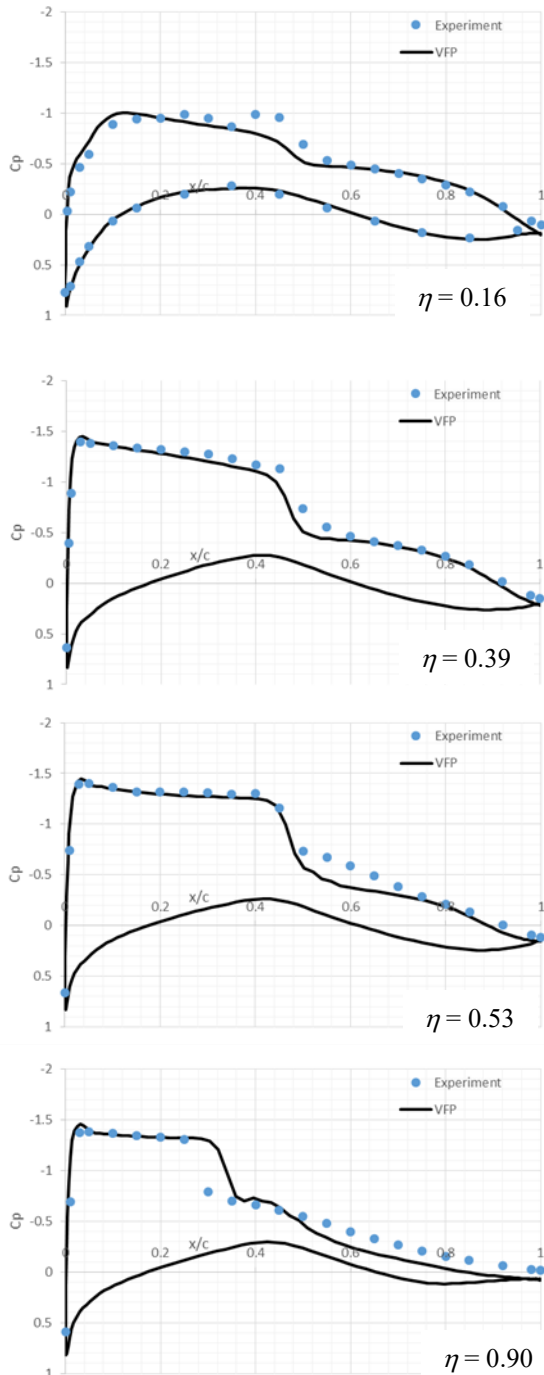


Fig 7: Comparison of measured and computed surface pressure distributions for W4. $M_\infty=0.78$, $\alpha = 2.0^\circ$, $Re_c=5.12 \times 10^6$.

The lower α case correctly resolves a shock free upper surface flow, while a strong swept shock wave is well resolved for the 2.5° incidence case. The shock wave is correctly seen to be the weakest inboard, strengthening outboard with a noticeable unsweep towards the tip where incipient boundary layer separation is known to occur.

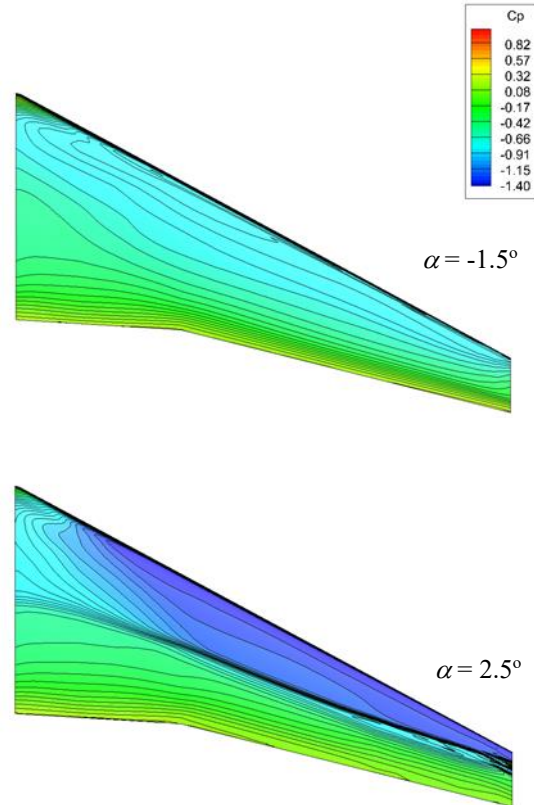


Fig 8: Selected VFP computed upper surface C_p contours for W4. $M_\infty=0.78$, $Re_c=5.12 \times 10^6$.

4.2 Test Case 2: The RBC12 Wing-Body Configuration

For test case 2 the VFP predictions were compared against both experimental data as well as high fidelity CFD, which in this case involved Delayed Detached Eddy Simulation (DDES) as part of another study of this test case. Fig 9 presents the surface mesh for the coarsest structured grid superimposed with the resulting surface C_p contours for the Mach 0.8, zero incidence, case of interest. Grid convergence was found (force coefficients to 3 significant figures) for cell counts of the order of ~ 20 million. Individual calculations involving the acquisition of 0.5 seconds of simulated flow took typically 15 days of run-time on 128 core processors of a

modern parallel cluster machine. The steady RANS ($k-\omega$ SST turbulence model) calculation from which the DDES simulation was started from took about 1 day for convergence to be achieved on the same computing resource. Compare this with a ~ 120 second run time for a corresponding VFP calculation on a single processor of a modest desktop PC.

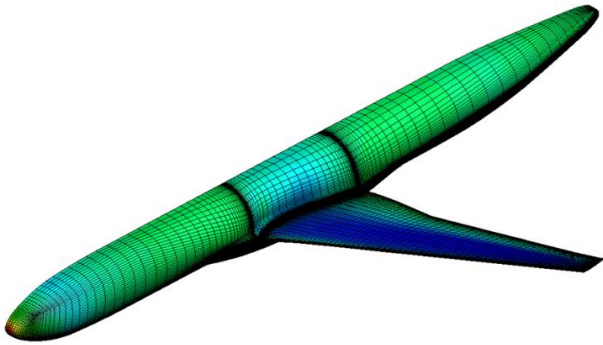


Fig 9: The coarse RBC12 structured surface grid, with surface C_p contours for the Mach 0.8, $\alpha=0^\circ$ case.

Fig 10 compares the lift and drag characteristics for both the VFP prediction and the initial RANS calculation (3 points only), with the corresponding experimental measurements [8]. Data for both the wing-alone and for the combined wing and fuselage are plotted for the predicted results.

Both the VFP and the RANS calculation resolve the lift and drag coefficients remarkably well at $\alpha=2.5^\circ$. The VFP result correctly resolves the non-linearity in the lift trend due the onset of shock induced viscous effects, together with the associated rise in drag. If anything the VFP slightly over-predicted the lift force which thereby resulted in excessive induced drag and a corresponding over-prediction in drag force compared with experiment. The RANS predicted lift is seen to follow the continued linear trend (dashed line), while the drag coefficient at the highest α was woefully under-predicted. Fig 11, which compares the experimentally measured (dynamic pressure sensitive paint) upper surface static pressure contours with the corresponding predicted results for the higher α case, provides a possible answer to this failure of the RANS/DDES method.

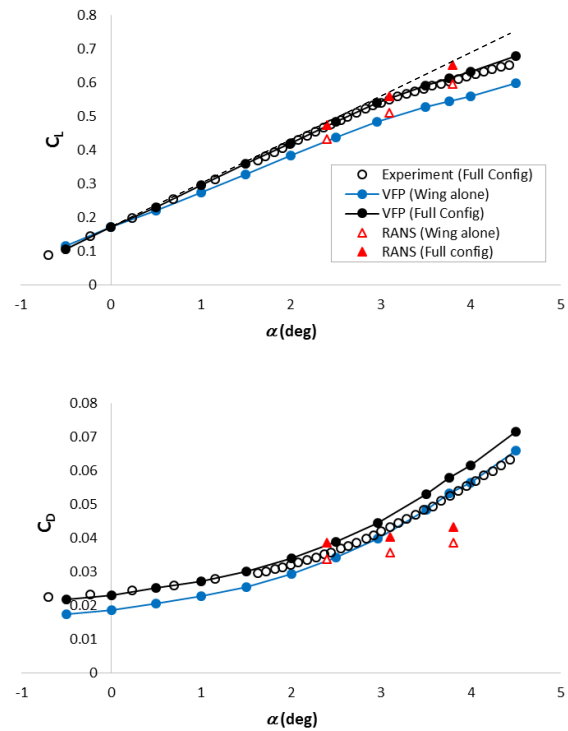


Fig 10: Comparison of measured and computed lift and drag characteristics with α , for RBC12.

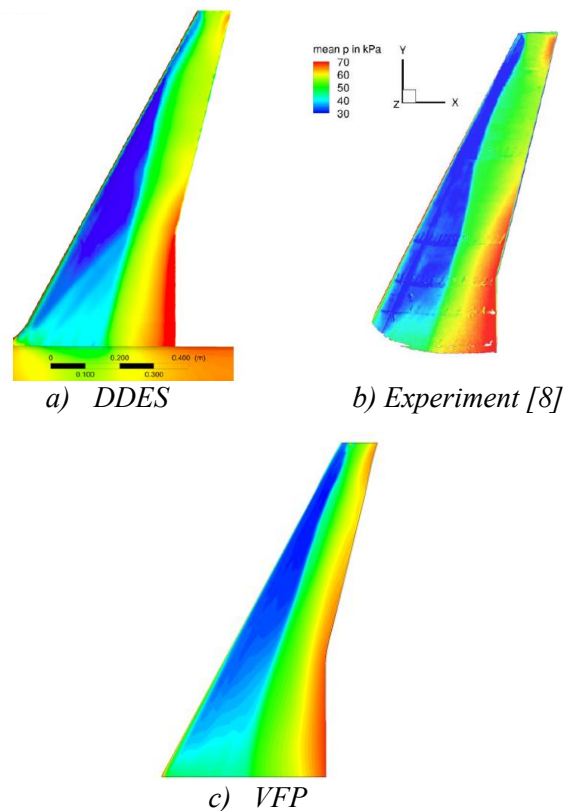


Fig 11: Comparison of measured and computed surface pressure contours for RBC12. $M_\infty=0.8$, $\alpha = 3.76^\circ$, $Re_c=3.75 \times 10^6$.

Close scrutiny of the pressure contours at the tip indicates that the time averaged DDES result (almost identical to the RANS result) predicts a much weaker upper surface shock wave, which sits closer to the leading edge, whilst the VFP result predicts a stronger shock sitting further rearward, with a considerable unsweep at the tip, as seen in the experiment. The VFP method solves the coupled turbulent boundary layer equations directly, while the CFD method solves approximate equations for the flow and the turbulence production and dissipation which almost certainly has resulted, in this case, in poor boundary layer resolution and corresponding shock evolution towards the tip leading edge.

A selection of the output from the VFP solver for the characterization of the local chordwise pressure and boundary layer state for the inboard spanwise station, $\eta=0.1$, is presented in fig 12. This is typical of the data that is produced and which can be quickly used to aid in deciding how a given wing may be redesigned for improved performance or for safer off-design characteristics. Such a method, for which an entire pitch sweep can be obtained in less than an hour on a modest desktop machine, clearly lends itself well to the conceptual design activity, where it would be unwise to deploy high resolution Navier-Stokes methods.

4.3 Test Case 3: The BW-11 Blended Wing-Body Configuration

For test case 3 the comparisons are only between VFP and Navier-Stokes predictions at an arbitrary Reynolds number, based on centre-span chord, of 9 million.

Fig. 13 presents the surface mesh density for the RANS calculations, where the hybrid grid encompassed ~ 14 million cells, and that used in the VFP calculation which comprised 135,432 cells. The RANS grid used a layer of 30 prismatic cells to model the boundary layer, where y^+ was found to be in the range 1 – 10.

A comparison of the VFP and RANS predicted (with three different turbulence models) lift and drag characteristics is provided in figure 14 for $M=0.75$.

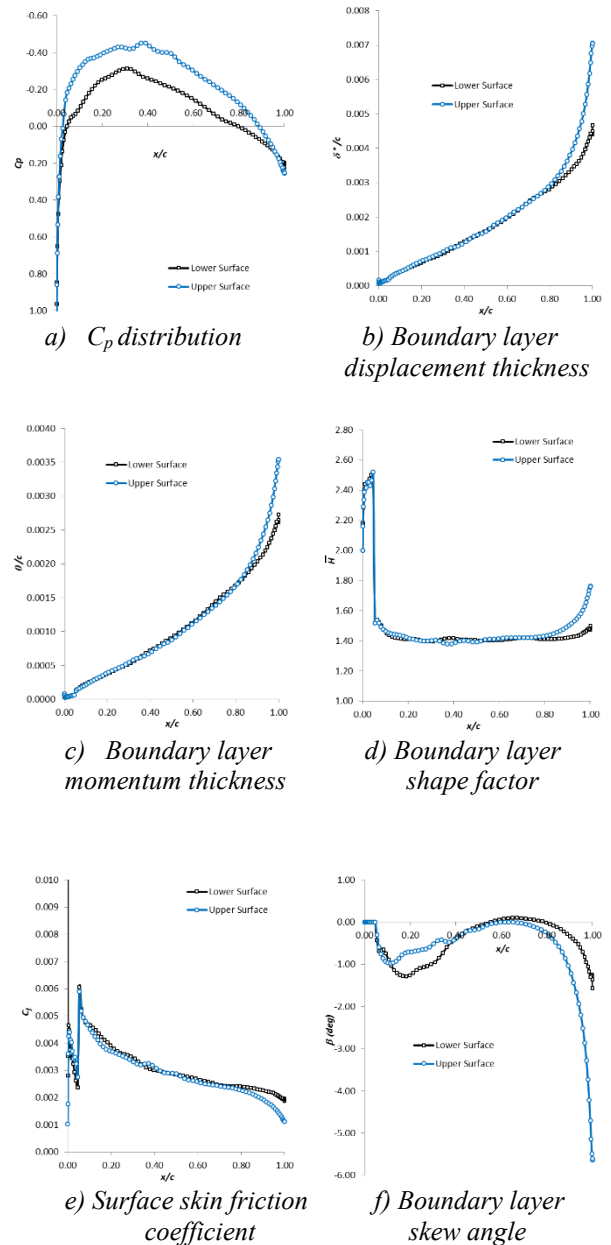


Fig 12: VFP computed chordwise distribution of viscous flow characteristics for RBC12 at spanwise location $\eta=0.1$. $M_\infty=0.8$, $\alpha = 3.76^\circ$, $Re_c=3.75 \times 10^6$.

The VFP predicted lift has been found to be lower at the higher α , where leading edge vortex suction, resolved in the RANS solution, cannot be predicted by VFP which assumes attached boundary layer flow. The agreement between the VFP and RANS resolved drag coefficient is, however, remarkably good. For rapid prediction of leading edge vortex related loading, semi-empirical predictions of the contribution can be added to the predicted lift figure.

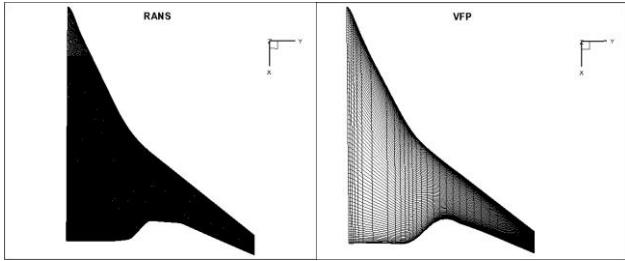


Fig 13: Comparison of the surface mesh densities used for the computational methods for the BW-11 predictions.

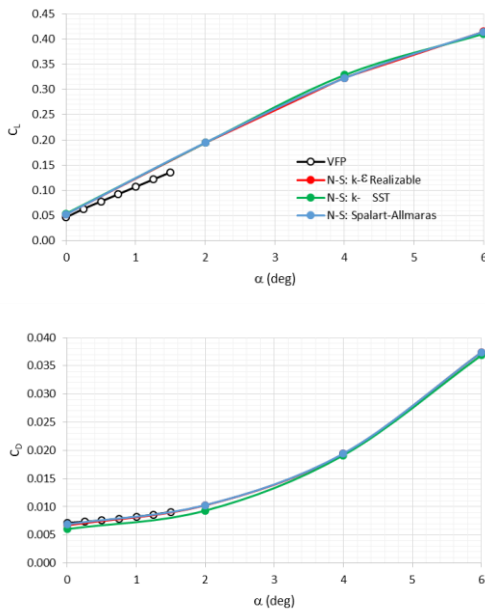


Fig 14: Comparison of the predicted lift and drag curves for BW-11. $M_\infty=0.75$, $Re_c=9 \times 10^6$.

Representative comparisons of the predicted upper surface pressure distributions at two Mach numbers are provided in fig. 15, which seems to demonstrate that the VFP method is successfully resolving the main flow characteristics including the large region of suction behind the wing leading edge crank, but fails to resolve the leading edge vortex suction on the forward fuselage. This is a focus for future improvement.

An important consideration in the design of blended wing-body aircraft is that of propulsion integration, for which an accurate set of data for the boundary layer characteristics on the upper rear fuselage is necessary if boundary layer ingesting intakes are employed. Here, the intake system must be carefully designed to minimize the degraded intake airflows arising from the ingestion of boundary layer air. Accurate

boundary layer data is therefore essential for the conceptual design analysis of such an aircraft.

Fig. 16 presents the kind of boundary layer data that can be rapidly produced using the VFP method to aid in the understanding of the local flow condition in the region where a boundary layer ingesting propulsion system is to be installed. In this instance, turbulent boundary layer data is plotted on the upper surface at spanwise locations $\eta = 0$ (the body centerline) and $\eta = 0.33$ (just outboard of the leading edge crank) for the $M = 0.8$, $\alpha = 0^\circ$ condition.

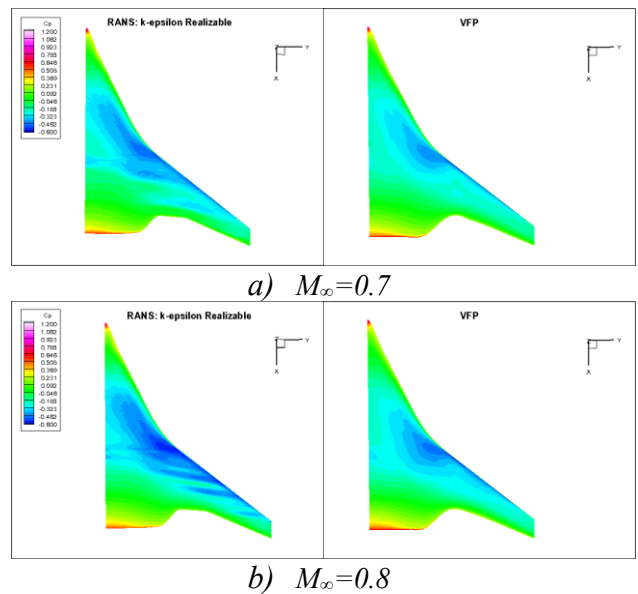


Fig 15: Comparison of the computed upper surface pressure contours for BW-11, $\alpha = 0^\circ$, $Re_c=9 \times 10^6$.

5 Conclusions

This paper, presenting some results of the feasibility assessment of using the Full Potential equations, coupled with the turbulent integral boundary layer equations, has demonstrated both the accuracy and the efficiency of the method for attach flow cases, prior to buffet onset, which are relevant to the transonic cruise condition. Use of such a method in the conceptual design stage is shown to be capable of yielding accurate enough data in a few minutes on a single processor, where Navier-Stokes simulations on 100+ processors can take several days.

Acknowledgements

This work was funded by Innovate UK and an Airbus UK led industrial consortia, as part of the ATI sponsored APROCONE project.

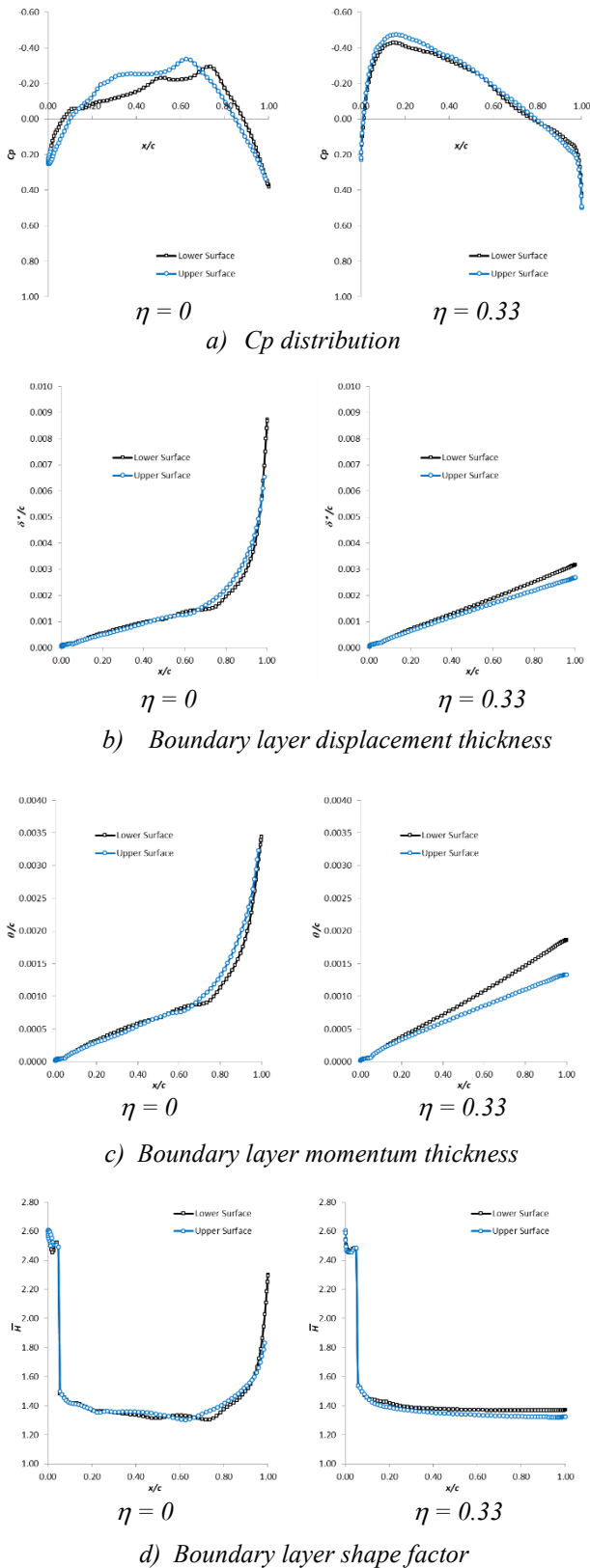


Fig 16: VFP computed chordwise distribution of viscous flow characteristics for BW-11 at two spanwise locations. $M_\infty=0.8$, $\alpha = 0^\circ$, $Re_c=9 \times 10^6$.

References

- [1] Full-potential (FP) method for three-dimensional wings and wing-body combinations – inviscid flow. Part I: Principles and results. ESDU 02013, June 2002 (with Amendment A, May 2006).
- [2] Von Karman, T. “Calculation of pressure distribution on airship hulls” NACA TM 574, 1930.
- [3] Viscous full-potential (VFP) method for three-dimensional wings and wing-body combinations. Part 1: Validation of VFP results with experiment and comparisons with other methods. ESDU 13013.
- [4] De Jarnette, F. R., Ford, C. P. & Young, D. E. “A New Method for Calculating Surface Pressures on Bodies at an Angle of Attack in Supersonic Flow” AIAA Paper 79-1552. AIAA 12th Fluid & Plasma Dynamics Conference, Williamsburg, VA, July 1979.
- [5] Ashill, P. R. & Smith, P. D. “An integral method for calculating the effects on turbulent boundary layer development on sweep and taper”, RAE Technical Report, TR83053. June 1983.
- [6] Smith, P.D. “A calculation method for the turbulent boundary layer on an infinite yawed wing in compressible, adiabatic flow. A.R.C. CP1268, 1974.
- [7] J. L. Fulker, “Pressure distributions on research wing W4 mounted on an axisymmetric body”, *AGARD AR 303*, Volume 2, 1994.
- [8] Lawson, S. G, Greenwell, D. & Quinn, M. K. “Characterisation of Buffet on a Civil Aircraft Wing” AIAA Paper 2016-1309, *AIAA 54th Aerospace Sciences Meeting*, 4-8 Jan. 2016, San Diego, California, USA.
- [9] Ashill, P. R & Smith, P. D. “An integral method for calculating the effects on turbulent boundary-layer development of sweep and taper”, *RAE Technical Report*, TR83053, June 1983.
- [10] Barnola, R. L. “Interaction between Aerodynamics, Structure and Packaging in a Blended Wing Body Configuration Conceptual Design”, Cranfield University MSc Thesis, 2012.

Contact Author Email Address

mailto: simon.prince@cranfield.ac.uk

Copyright Statement

The authors confirm that they, and/or their company or organization, hold copyright on all of the original material included in this paper. The authors also confirm that they have obtained permission, from the copyright holder of any third party material included in this paper, to publish it as part of their paper. The authors confirm that they give permission, or have obtained permission from the copyright holder of this paper, for the publication and distribution of this paper as part of the ICAS proceedings or as individual off-prints from the proceedings.